For the attention of SFOE Section Energy Research

Contract- and project number: SI/500910-01 / 8100075 (Program: Combustion)
SI/500902-01 / 8100082 (Program: Grids)

Final Report

Renewable Energies in Future Energy Supply

(RENERG^2)

WP1 Electrolysis
WP2 Methanation
WP3 HCNG Combustion Fundamentals
WP4 HCNG Field Testing
WP5 Market & Grid

25th of October 2017

1. Summary

The RENERG^2 project was started officially in July 2013 and finished in September 2017. This final scientific report summarizes the results over the whole project duration. The project was divided into the 5 work packages Electrolysis (WP1), Methanation (WP2), Combustion fundamentals (WP3), HCNG field test (WP4) and Markets and Grids (WP5).

WP1 Electrolysis

The main goal of WP1 within the RENERG^2 project is (i) the development of a new anode catalyst for both polymer electrolyte water electrolyzers (PEWEs) and co-electrolyzers with none or reduced noble metal content and its transfer into a single cell electrolyzer. In addition, we are focusing on the development and understanding of efficient catalysts for the electrochemical reduction of CO_2. Both pathways are supported by theoretical modeling by density functional theory (DFT) of the stability and activity of the respective systems.

One of the major cost inhibitors of PEWEs is the use of IrO_2 as anode material. Iridium is not only an expensive noble metal, but it is also a non-abundant element which prevents its implementation as anode material into PEECs on a large scale. Replacing Ir in the anodic electrode of PEECs is, however, challenging due to the harsh requirements for the anodic catalyst which are (i) stability in acidic environment at high electrode potentials and (ii) a reasonable oxygen evolution activity.

In this work package dealing with electrolysis, we follow a multi-level approach in order to research, develop and understand the limiting electrocatalytic reactions in acidic water electrolysis systems, viz. the oxygen evolution reaction (OER), and in co-electrolysis systems, viz., the CO_2 reduction.

In the context of improving the performance of OER catalysts, IrO_2 catalysts with high surface area (up to 150 $m^2\ g^{-1}$) were prepared and fully characterized in order to understand the influence of particle size, morphology, surface structure, and the nature of surface species on the electrochemical OER activity of nanocrystalline IrO_2. IrO_2 nanoparticles with the highest surface area also displays the highest mass activity ($E = 1.499 \pm 0.003$ V at 10 Ag_{ox}^{-1}). The high OER activity was correlated not only to the catalyst surface area but also to the presence of an initial iridium hydroxide layer. For the highest surface area sample *operando* X-ray absorption spectroscopy shows that the initial fraction of Ir^{3+}, which is associated with the hydroxide layer, is reversibly converted to Ir-oxide species as the OER proceeds.

Unfortunately, IrO_2 as nanoparticles suffers of poor stability under OER conditions. Therefore we have oriented our research towards other structures containing reduced Ir-content.

Pyrochlores are a family of complex oxides with a general formula $A_2B_2O_{6.5+x}$, where noble metals can be partially replaced by earth-abundant elements providing a compromise between activity, stability, and cost of the OER catalysts. Pyrochlores of the general formula $(A, A')_2(Ir/Ru)_2O_{6.5+x}$ (A, A' = Bi, Pb, Y) were synthesized via the modified Adams fusion method and possess the surface areas in the range 10 – 40 $m^2\ g^{-1}$. Electrochemical measurements in acidic media showed that yttrium and bismuth pyrochlore catalysts possess high OER activity approaching the activity of state-of-the-art IrO_2 nanoparticles. High intrinsic activities and stability behavior of yttrium iridium catalysts were correlated with the formation of the highly active IrOx surface layer due to leaching of the Y^{3+} cations into the electrolyte solution, revealed both experimentally and computationally using density functional theory calculations**.** The Ir-based pyrochlores present good stability over the 500 cycles, with an activity loss within the 20%. This is not the case for the Ru-based pyrochlore showing a complete failure of the activity over the potential cycling. Based on the activity and stability results, it can be concluded that $Y_2Ir_2O_7$ and $Bi_2Ir_2O_7$ pyrochlores represent the best candidates as OER catalysts for application in polymer water electrolyzers.

WP2 Methanation

a) *Hydrogen addition to hydrothermal gasification/methanation*

In WP2, peak electricity storage as (bio-)methane was studied and demonstrated using the hydrothermal gasification and methanation process developed at PSI. One approach involved the production of H_2 by electrolysis and co-feeding the H_2 with the biomass into the hydrothermal gasification process. The feasibility of this approach was demonstrated both theoretically by modeling as well as by small-scale experiments in a continuous hydrothermal gasification test rig at PSI. Addition of hydrogen in a stoichiometric amount produced a methane rich gas from glycerol with (86 $\pm$ 6) vol% CH_4, which corresponded to the calculated maximum value of 88 vol% at the chemical equilibrium. No detrimental effect on the catalyst when co-feeding H_2 was observed. A second approach would involve an electric process heater for the hydrothermal gasification process, operated on the peak electric power. When no such peak power is available, the heater would be operated on a methane-rich gas. To this aim, a dual gas/electric heater was designed using commercial components. In summary, both approaches to store electric peak power as biomethane using hydrothermal gasification technology were shown to be feasible.

b) Hydrogen-rich methanation of CO_2-containing gases

Within this project, the know-how on CO_2 methanation (converting biogas and pure CO_2, e.g. from industrial sources) and hydrogen-rich methanation of gasification derived producer gas was increased by modelling and experiments. As the pilot scale set-up "GanyMeth" that originally should be used unfortunately was not available within the project time, experiments were conducted using the TRL 5 plant Cosyma. Within another project, Cosyma was connected to a biogas plant in Zürich. After achieving the goals of that other project, the operation of the installation was continued to conduct optimisation experiments. In these experiments, it was found that the addition of water can be significantly reduced without coke formation, which improves the yield in the main reactor and will allow decreasing the effort (CAPEX and OPEX) in the upgrading step of the process.

In parallel, the complete process chain of biogas based power-to-gas was modelled and optimised. For this, the main units (reactors, membranes) were represented by rate-based models, while other process units were calculated with thermodynamic and short-cut models. The detail description of four different process concepts allowed also detailed cost calculations. It was found that the grid injection specifications make an upgrading step, e.g. by a hydrogen separation membrane or a second fixed bed reactor, necessary. The optimum with respect to process robustness and flexibility turned out to be introducing a hydrogen separation membrane which in turn changed the conditions in the main reactor due to recycled hydrogen and methane.

WP3 (Combustion fundamentals)

WP3 focused on experimental and numerical investigations of the early flame phase of premixed methane/air and hydrogen enriched methane/air combustion. A high pressure experimental test rig was designed and built, with optical access for spectroscopic diagnostics. This allowed for application of the Spark-Induced Breakdown Spectroscopy (SIBS) technique at engine relevant conditions. We could successfully demonstrate the capability to determine hydrogen content of the admixture, based on C_2 swan band and atomic hydrogen emissions. Ratios of atomic emission lines of hydrogen, oxygen and nitrogen exhibited an unambiguous dependency on the air-methane ratio. The oxygen-hydrogen ratio showed a much higher sensitivity compared to formerly reported ratios of molecular emissions such as hydroxyl (OH), nitrogen monohydride (NH) and cyanogen (CN) and is applicable for the complete range of interest for methane-air mixtures. The time resolved measurement data revealed the coupling effects of the secondary

circuit in the ignition system with the measured intensity in the spectra. Based on findings in the ignition cell, an optical spark plug was designed to enable SIBS and early flame front arrival measurements in optically non-accessible test rigs, such as full metal Internal Combustion Engines (ICE).

In the Rapid Compression Expansion Machine (RCEM) at ETHZ efforts focused on the generation of well-defined turbulence levels by means of high pressure gas injection during the early compression stroke. A high-speed Particle Image Velocimetry (PIV) system was commissioned allowing for two-dimensional characterization of the evolving flow field, which were complemented by three-dimensional (3D) Computational Fluid Dynamic (CFD) calculations. In combination thereof, optimal injection strategies (injector location and orientation as well as injection timing and pressure) were derived to reach engine relevant turbulence levels at spark timing. Good agreement was found between experiments and 3D-CFD simulations with respect to the general flow pattern and the turbulent fluctuation speed close to the spark plug. Careful alignment between the RCEM experiments and work conducted in WP4.3 (measurements in the single-cylinder full metal engine) ensured A) thermo-dynamic conditions, viz. pressure and temperature levels, B) equivalence ratio and C) hydrogen addition levels as close as possible in the optical rig to the full metal engine conditions.

PIV measurements paired with OH* chemiluminescence or Schlieren imaging have been conducted in the RCEM for laminar and turbulent reactive conditions at three hydrogen enrichment ratios. The benefit of hydrogen admixture on the faster flame kernel formation was successfully demonstrated via both optical techniques as well as heat release rate calculations.

A database characterizing laminar flame properties for a wide range in unburned temperature, pressure and mixture composition relevant to engine conditions has been generated by computing flame structures for freely propagating laminar premixed flames using a detailed chemical mechanism. For the single-cylinder research engine 3D-CRFD calculations have been performed, and a literature survey concerning suitable combustion models – in particular with respect to their appropriateness for hydrogen admixtures – has further been conducted. Closures for the turbulent flame speed have been assessed based on previously existing engine measurement data. A Large Eddy Simulation (LES) framework has been established and proven to be capable to reproduce the cycle-to-cycle variations (CCV) measured in the engine.

WP4 HCNG field testing

In WP4 investigations on the utilization of the fuel mixture HCNG for mobile and stationary applications were carried out. HCNG contains H_2 (hydrogen) and CNG (natural gas/biogas) whereby the focus lied on H_2 admixture of 0 to 25 vol-% for the mobile and 0 to 50 vol-% for the stationary application.

To enable refueling of three CNG test vehicles, a temporary refueling solution allowing low H_2 admixture of 2 vol-% was realized. 2 vol-% is the highest H_2 fraction permitted for conventional CNG vehicles by the respective Swiss regulations. The test vehicles were operated several months with both pure CNG and 2 vol-% H_2 admixture as part of the parcel delivery fleet of Swiss Post while data was gathered onboard with data loggers. The analysis of the data indicated small tendencies towards improved efficiency and a decrease in CO_2 emissions which presumably results from an improved combustion process. The amount of H_2 added was very little, the effect lies within the statistical uncertainty. However, it was observed that engine starting behavior could be improved considerably. In general the results confirmed that adding low amounts of H_2 in the fuel of conventional CNG vehicles have no negative but rather positive effects even though no modifications to the vehicle were carried out. A paper on this topic is currently in preparation and is expected to be submitted in the beginning of 2018.

For the field tests with higher H_2 content (up to 25 vol-%) a different CNG vehicle was retrofitted with new tanks and fuel lines to ensure compatibility with H_2. The new fuel system and the vehicle have been re-certified and the vehicle has started its field test in the parcel delivery service of Swiss Post. Also a new permanent HCNG dispenser was realized allowing the refueling of mixtures with 0 to 30 vol-% of H_2. The setup and the control algorithm of the dispenser were developed at Empa based on measurements and simulations carried out in the scope of this project. During the field test, the vehicle showed no negative behavior, neither in CNG nor in HCNG operation and also the HCNG filling station worked as reliable as the normal CNG filling station.

Regarding stationary applications the impact of the fuel HCNG on a micro combined heat and power plant (mCHP) was investigated. Thereby the emphasis was put on analyzing the effects of H_2 admixing during lean burn operation and exhaust gas recirculation (EGR) on the combustion process and raw emissions. Measurements were taken on a single cylinder 4-stroke spark ignited and naturally aspirated engine of 250 cm^3 swept volume including an upstream gas mixing device to supply predefined rates of EGR and H_2.

It was found that by adding H_2 to CNG it is possible to extend the operating limits of a naturally aspirated mCHP engine for lean burn operation from $\lambda = 1.4$ (CNG only) to $\lambda = 1.8$ ($50\%_{vol.}$ H_2) and for EGR operation from EGR = 10% (CNG only) to EGR ≥ 25% ($50\%_{vol.}$ H_2). The extension of the operating lambda allows for a significant raw NO_x emission reduction down to below 250 mg/Nm^3 which is the legal limit for stationary gas engines in the smallest power class in Switzerland. However, even with hydrogen extended EGR operation this NO_x limit cannot be reached. The efficiency bonus of adding hydrogen increases rapidly with increasing lambda and can be observed starting from $\lambda = 1.2$. This phenomenon is almost not observable for EGR operation.

WP5 Grids and Markets

In this WP we carried out a qualitative and quantitative feasibility analysis of the Power-to-Gas (PtG) technology in the future Swiss low voltage (LV) grid, which will be characterized by a significant share of intermittent renewable energy sources (RES). For this purpose, a financial simulation platform has been built and a model of producing hydrogen or methane with Photovoltaics (PV) excess energy and additional energy from the grid has been established. Data and results from load flow analyses of a Swiss grid model served as the basis for the analysis.

After the Fukushima accident in 2011, Swiss Federal government has set forth a new energy policy, so-called Energy Strategy 2050, to implement cessation of the existing nuclear power plants with implementation of a strong expansion of renewable energy sources. PV, for example, shall make up one fifth of Switzerland's total energy production in 2050. Such a drastic expansion rate of PV can lead to so-called reverse power flow in the LV grid. According to a prior study, in which the load flow of a Zürich area was calculated, it was found necessary to install a suitable battery energy storage system (BESS) to resolve the reverse power flow, which may be caused by the excess PV energy production. Alternatively, a PtG plant represents another suitable storage solution for absorbing the excess PV energy production in the LV grid in the future.

The results obtained in this WP demonstrate the impact of the PtG technology through nine different operating scenarios established. The input energy source to the PtG plant comprises the excess PV energy and the energy from the grid. Economic values, such as levelized cost of energy (LCOE) and levelized value of electricity (LVOE) has been determined to assess the economic feasibility. Moreover, sensitivity analysis has been carried out to identify the parameters having the strongest impact on the electricity cost.

Acknowledgements

The RENERG^2 project team would like to express special thanks of gratitude to the funding agencies: Competence Center of Energy and Mobility in the ETH-Domain (CCEM), the Swiss Federal Office for Energy (SFOE), the Swisselectric Research (SER) and the Swiss Gas Association (VSG/SVGW) as well as to the industrial partner within the work packages.

2. Electrolysis (WP1)

PSI, Electrochemistry Laboratory: ***Thomas J. Schmidt, E. Fabbri, Y. Paratcha, K. Waltar, J. Herranz***
EPFL, Theory and Simulation of Materials: ***Nicola Marzari, Ivano Castelli***
ETHZ, research group name: ***Christophe Copéret, A. Fedorov, D. Lebedev***

2.1 General targets and state of WP1 compared to the proposal aims/milestones

The goal of WP1 (Electrolysis**,** funded by BFE, Swiss Electric Power and CCEM) within the RENERG^2 project is to generate new anode catalysts for both polymer electrolyte water electrolyzers (PEWEs) and co-electrolyszers with none or reduced noble metal content and its transfer into a single cell electrolyzer, eliminating one of the major cost inhibitor of PEWEs. In one path, we are focusing on the development of new electrocatalytic systems for the oxygen evolution reaction (OER), a reaction taking place in both water electrolyzers and co-electrolyzers. In addition, we are focusing on the development and understanding of efficient catalysts for the electrochemical reduction of CO_2. Both pathways are supported by theoretical modeling by density functional theory (DFT) of the stability and activity of the respective systems.

In this work package dealing with electrolysis, we follow a multi-level approach in order to research, develop and understand the limiting electrocatalytic reactions in acidic and alkaline water electrolysis systems, viz. the oxygen evolution reaction, and in co-electrolysis systems, viz., the CO2 reduction. Within the WP, there are three PhD students working at SIC@ETH and ECL@PSI, respectively and one Post-Doctoral Researcher at THEOS@EPFL.

2.2 Main Achievements of WP1

a) *Catalysts for the Oxygen Evolution Reaction*

IrO2-RuO2 catalysts

In order to have a more defined and rational strategy on the design of novel materials, a first step of the study was a more detailed understanding of the benchmark IrO_2 – RuO_2 electrocatalytic system. To the best of our knowledge even for this well-studied system the detailed mechanism of the OER as well as the underlying factors responsible for the limited stability of the materials are still not fully understood today.

The present research work was focused on making IrO_2 – RuO_2 catalysts via one of the most widely used methods for the synthesis of noble metal oxide nanoparticles – so-called Adams fusion method wherein nanoparticles are synthesized by oxidative decomposition of Ir or Ru containing precursors (e.g. chlorides) in a molten sodium nitrate.

Five benchmark materials $Ru_xIr_{(1-x)}O_2$ with x = 0, 0.25, 0.5, 0.75 and 1 were prepared via Adams fusion method. Experimental procedure can be briefly described as follows: appropriate amounts of $RuCl_3$ hydrous, $IrCl_3$ hydrous (in total 0.5-0.6 g) and 15 g of $NaNO_3$ were dissolved in 100 ml of deionized water. After homogenization the solution was dried under vacuum and thus obtained powder was calcined in a muffle furnace using the following temperature program: RT – 30 min – 150°C – 30 min – 150°C – 60 min – 350°C – 30 min – 350°C. Obtained sample was washed with deionized water and dried at 150°C under vacuum.

Catalysts were studied using different techniques: powder X-ray diffraction (XRD), transmission electron microscopy (TEM), and nitrogen adsorption / desorption. Powder XRD diffraction patterns of the samples are presented in Figure 2.1. Broad peaks indicate the formation of small nanoparticles in all samples. All obtained reflections match rutile type structure, which is in the good agreement with the literature data.

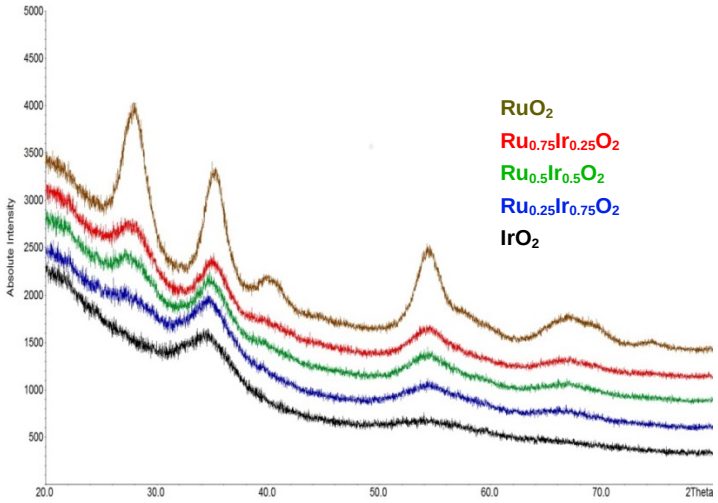

Fig. 2.1 Powder XRD patterns of IrO_2 – RuO_2 samples

TEM studies (Figure 2.2) confirm formation of small and narrowly distributed nanoparticles. Calculated particle size distributions (Figure 2.3) give the following average particle sizes: 4.4 ± 1 nm for RuO_2, 2.8 ± 0.8 nm for $Ru_{0.75}Ir_{0.25}O_2$, 1.4 ± 0.3 nm for $Ru_{0.5}Ir_{0.5}O_2$, 1.4 ± 0.2 nm for $Ru_{0.25}Ir_{0.75}O_2$ and 1.3 ± 0.3 nm for IrO_2. BET analysis of nitrogen adsorption / desorption isotherms indicates that all the samples have high surface area (> 200 m^2/g), which was achieved by lowering of the reaction temperature and time during the synthesis process (30 min at 350°C).

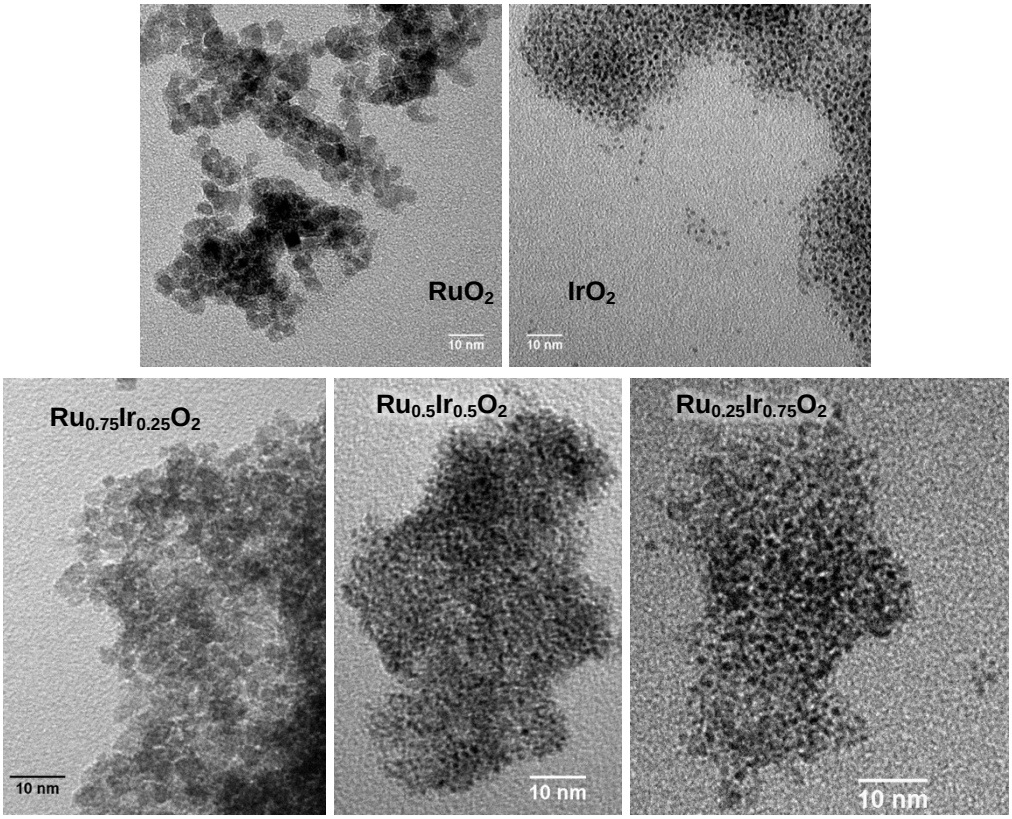

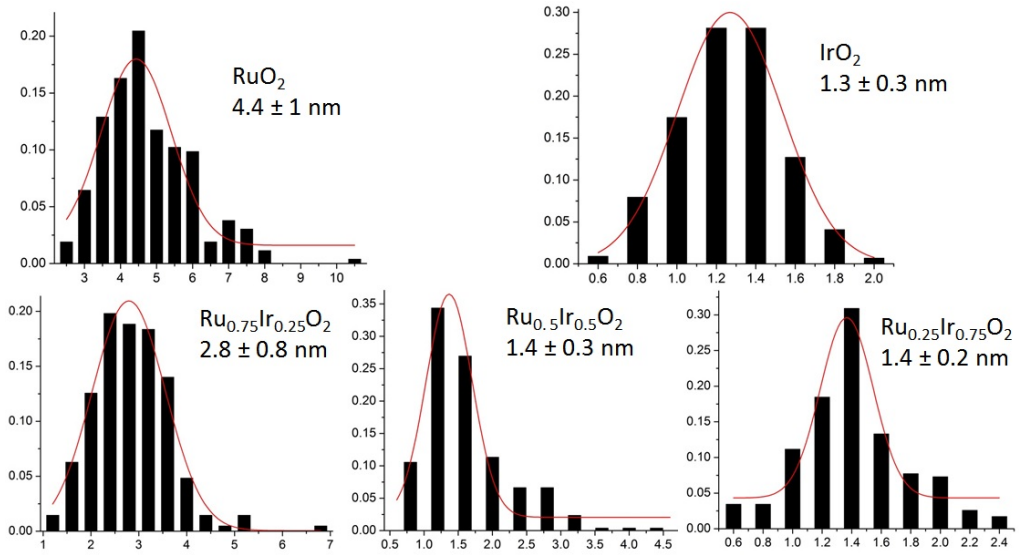

Fig. 2.2 TEM images and calculated particle size distributions of IrO2-RuO2 samples

The investigated benchmark catalysts $Ru_xIr_{(1-x)}O_2$ with x = 0, 0.25, 0.5, 0.75 were analyzed with respect to their electrochemical activity which is herein defined as the electrode potential needed to drive a total current density of 10 A/g under potentiostatic conditions. Polarization curves of the different catalysts performed in 0.1 M $HClO_4$ at ambient temperature and an atmosphere containing 20 mol% O_2 are presented in Figure 3.

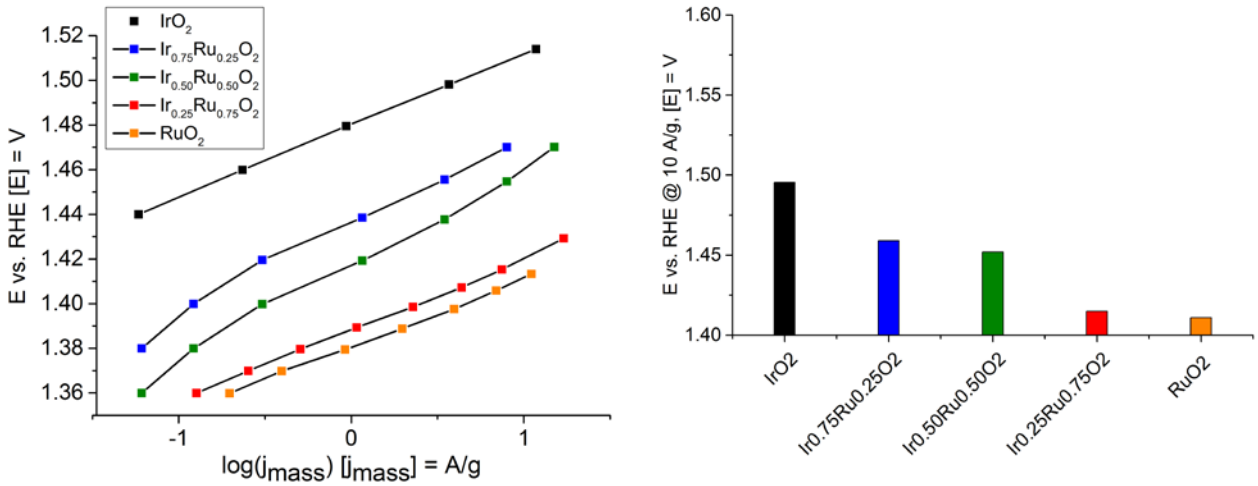

Fig. 2.3 Left: Polarization curves of all investigated benchmark catalysts. All curves are recorded under potentiostatic conditions in a 0.1 M HClO4 electrolyte and under an atmosphere containing 20 mol% O_2. The working electrode is rotated at 900 rpm. Right: Bar plot of the electrode potential at 10 A/g indicating the decrease in overpotential or respectively the increase in activity with higher Ru content.

All the catalysts presented in this work are highly active towards the OER[1]. Nevertheless, Ru and Ir are noble transition metals, and their large-scale implementation into real electrolyzer applications is expected to increase costs. Additionally to this issue of costs, Ru and its oxides have shown poor electrochemical stability (rapid drop of the current while holding a potential in the OER regime). For this reason it has been decided to work only on stable system (IrO_2 catalysts), trying to keep a good OER activity while decreasing the amount of noble metal content in the catalyst.

IrO_2 catalysts

In the context of improving the performance of OER catalysts, IrO_2 catalysts with high surface area were prepared and fully characterized in order to understand the influence of particle size, morphology, surface structure, and the nature of surface species on the electrochemical OER activity of nanocrystalline IrO_2.[2] A chloride-free modified Adams method was developed to prepare a wide range of particle sizes. Furthermore, a broad range of physical characterization techniques including N_2 adsorption/desorption measurements, high-resolution transmission electron microscopy (HRTEM), powder X-ray diffraction (XRD), X-ray photoelectron spectroscopy (XPS), and operando X-ray absorption spectroscopy (XAS) were used to relate the structural and morphological changes to the observed electrochemical OER activity and catalyst stability.

Iridium oxide nanoparticles synthesized via a modified Adams fusion method from the iridium(III) acetylacetonate ($Ir(acac)_3$) precursor and annealed at 350 °C present a specific surface areas of ca. 150 m^2g^{-1}. The experimental procedure can be briefly described as follows: 300 mg of Ir(III) acetylacetonate ($Ir(acac)_3$, 98% Ir, Strem Chemicals) and 10 g of $NaNO_3$ (>99.5%, Sigma Aldrich) were homogenized by grinding in an agate mortar. The obtained yellow powder was transferred into a porcelain crucible and heated in a muffle furnace at 350 °C for 30 min. The obtained samples were then washed with deionized water and subsequently dried at 150 °C overnight under ca. 2 mbar of residual air pressure to give the black powder of IrO_2 nanoparticles. Increasing the synthesis temperature up to 500 and 600 °C yielded IrO_2 with surface area of 110 and 90 m^2g^{-1}, respectively. Post-synthesis calcination of at 600 °C provides IrO_2 with a much lower surface area of about 30 m^2g^{-1}. The samples are named according to their approximate BET surface area, for example, IrO_2-150 ≈ 150 m^2g^{-1}.

As shown by transmission electron microscopy (TEM, Figure 2.4), the particle size of all synthesized iridium oxide nanoparticle materials increases with increasing synthesis temperature, which is in line with the N_2 adsorption/ desorption data.

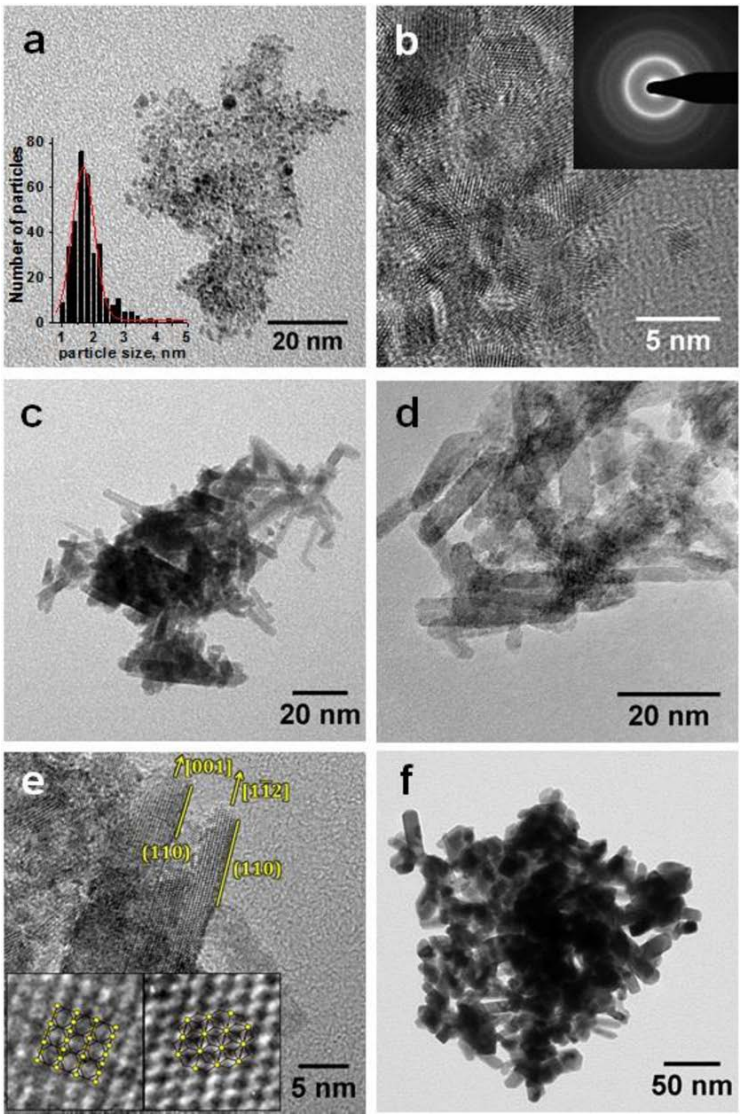

Fig. 2.4 TEM and particle size distribution (inset) of IrO2-150 (a); HRTEM and electron diffraction (inset) of IrO2-150 (b); TEM of IrO2-110 (c); TEM of IrO2-90 (d); HRTEM of IrO2-90; insets show part of IrO2 rutile structure overlaid with HRTEM images of corresponding particles (e); and TEM of IrO2-30 (f).

According to the high-resolution TEM (HRTEM) studies (see Figure 4b and e), all synthesized materials are crystalline. The sample with 150 m^2g^{-1} (IrO_2-150) consists of small spherical particles (1.7 ± 0.4 nm in diameter, Figure 4a, inset), while the samples prepared at higher temperature (IrO_2-110, IrO_2-90 and IrO_2-30) mainly consist of rod-shaped particles.

Detailed electrochemical studies of the OER activity (taken as the Ohmic-drop corrected potential measured at 10 A per grams of oxide) showed that the catalyst with the largest surface area (150 $m^2\ g^{-1}$) consisting of small (<2 nm) nanoparticles is significantly more active towards oxygen evolution reaction compared to other IrO_2 materials with lower BET surface area (see Figure 2.5). Such increase in the activity cannot only be explained by increase of the surface area.

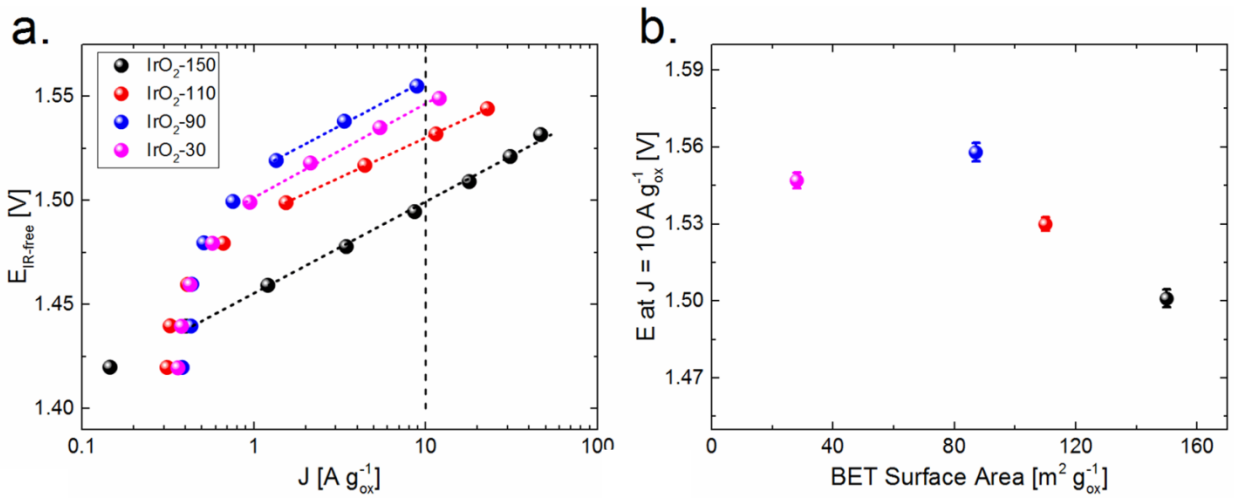

Fig. 2.5 OER Tafel plots showing the steady-state current density recorded after 1 min in 0.1 M HClO4 (a); OER activity (defined as potential at the current density J = 10 Ag−1) as a function of surface area (b)

The increased activity of this catalyst was explained by presence of the surface hydroxo layer, detected by both XPS and XAS studies. The Ir 4f spectra for IrO_2-150 and IrO_2-30 are shown in Figure 2.6a and b, respectively. The asymmetric 4f region characteristic of rutile-type IrO2 consists of two main components: the Ir 4f7/2 and Ir 4f5/2 binding peaks, which in the case of IrO_2-30 are located at ca. 61.7 and 64.7 eV. These values are in very close agreement with those previously reported in the literature for rutile IrO_2. In contrast, the 4f peaks for IrO_2-150 are clearly shifted to higher binding energies, suggesting the presence of Ir3+ sites with. Moreover, the broader shape of the peaks in the Ir 4f spectrum of IrO_2-150 as compared to IrO_2-30 highlights a broader distribution of sites.

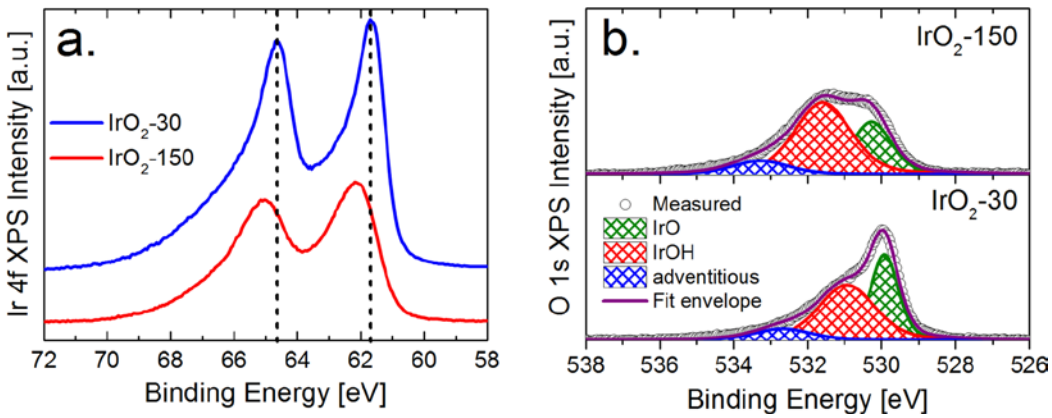

Fig. 2.6 Ir 4f (a) and O 1s (b) XPS spectra of the prepared IrO_2-150 and IrO_2-30 materials

Operando XAS studies were performed at the SuperXAS beamline of the Swiss Light Source of Paul Scherrer Institut. X-ray absorption near edge structure (XANES) spectra recorded at different potentials show a reversible shift of the Ir−edge position as a function of the applied potential (Figure 2.7a). Such shift corresponds to an increase of the Ir oxidation state at high electrode potentials. Furthermore, the Ir−O bond length obtained from the Extended X-ray absorption fine structure (EXAFS) fitting gradually changes from ca. 2.02 Å at 1.00 V to 2.01 Å at 1.50 V. The average bond length for Ir−O in IrO_x containing Ir^{3+} was reported to be ca. 2.02 Å, whereas the bond length of Ir^{4+} in the IrO_2 rutile oxide is closer to 1.98 Å.[3] Therefore, the shortening of the Ir−O bonds within the octahedron represent the transition of IrO_2−150 from a mixed $Ir^{3+/4+}$ state, to a structure more populated by Ir^{4+}, which is in line with XANES studies. Overall the observed behavior is consistent with the reversible transformation of the hydroxo surface layer of the IrO_x nanoparticles to oxo surface species with increase of the applied potential.

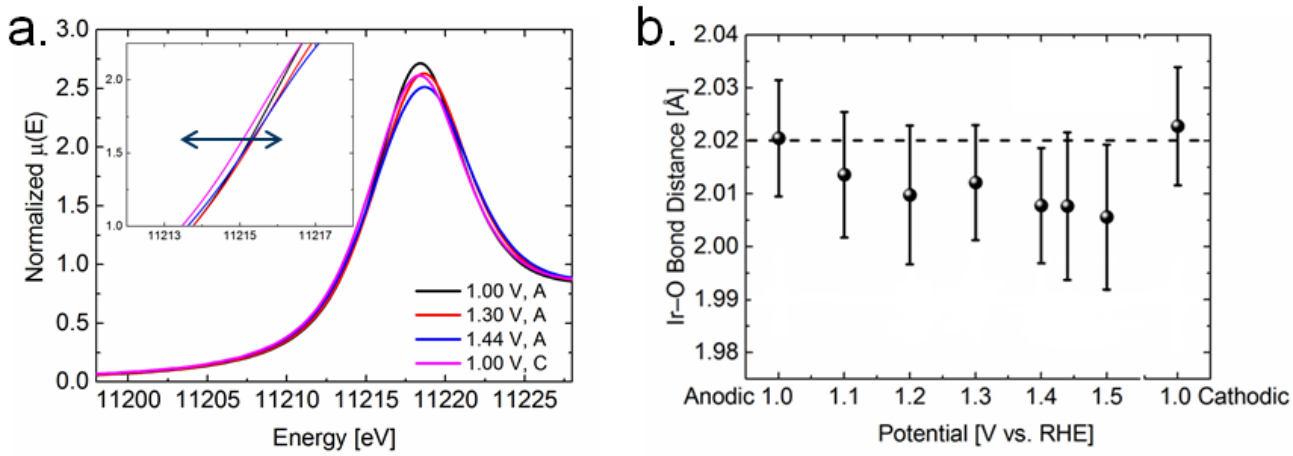

Fig. 2.7 Normalized XANES spectra for IrO_2−150 recorded at different electrode potentials, inset shows an expansion of the absorption peak to highlight the change in position (a); the EXAFS-determined Ir−O bond distance shown over the range of applied potentials (b).

To summarize, *operando* XAS and XPS investigations indicate the presence of iridium hydroxo (Ir−OH) surface species for the IrO_2-150 samples, which seems to be strongly linked to the high OER activity observed for this catalyst.

<u>IrO_2–TiO_2 catalysts</u>

In the context of decrease the amount of IrO_2 in OER catalysts without losing catalysts performances, IrO_2–TiO_2 catalyst was synthesized in one step via modified chlorine-free Adams fusion method.[4] The obtained catalyst with 40 mol_M% of Ir has the surface area of 245 $m^2\ g^{-1}$ (denoted here as IrO_2−TiO_2−245) and possesses sufficient electrical conductivity of 0.26 S cm^{-1}. Powder X-ray diffraction studies of the catalyst show the formation of rutile IrO_2 and TiO_2 as well as anatase TiO_2 nanoparticles.

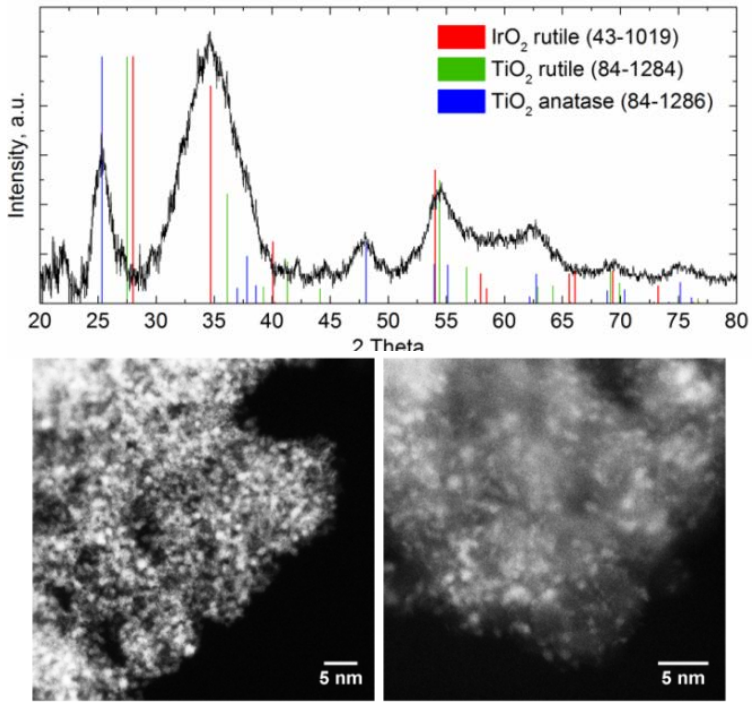

Fig. 2.8 Powder X-ray diffraction pattern of IrO_2−TiO_2−245 with reference patterns and HAADF-STEM images of IrO_2−TiO_2−245

The activity and stability of IrO_2−TiO_2−245 towards OER electrocatalysis was investigated using rotating disk electrode experiments and compared to the high surface area IrO_2-150 and benchmark industrial catalyst provided by Umicore with an iridium loading of ~66 mol_M%[5-6], denoted here as IrO_2−TiO_2−Umicore (34 $m^2\ g^{-1}$ by BET analysis). The stability tests are intended to simulate the start/stop behavior of an electrolyzer by stepping between a potential close to the open circuit value, i.e. where no OER current is observed (1.00 V), and a potential where an appreciable OER current is observed, i.e. J > 10 A g^{-1} (1.60 V). Thus the stability protocol consists of stepping the applied potential between 1.0 and 1.6 V while holding for 10 seconds at each potential for 500 cycles. Further details of the measurement procedure are given in the experimental section. The normalized current values are based on the current reading at 1.6 V after every 100 cycles (Fig. 2.9b).

Evaluation of the electrochemical activity of the IrO_2-TiO_2 catalyst showed that the catalyst has similar Tafel slope compared to the high surface area IrO_2-150, which indicates that the OER is likely proceeding by the same mechanism and the presence of TiO_2 does not affect the reaction pathway. The catalyst shows improved activity and stability not only compared to the commercial IrO_2-TiO_2 catalyst but also compared to the high surface area IrO_2. The latter may result from the better distribution and accessibility of the IrO_2 particles the presence of particle – support interactions, such as the epitaxial particle growth and / or partial iridium – titanium intermixing.

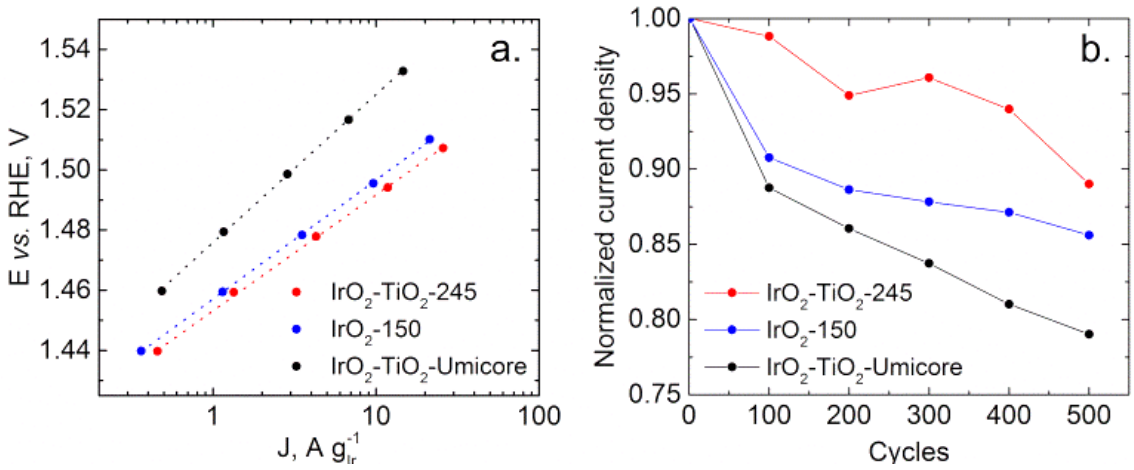

Fig. 2.9 Tafel plots (a) and stabilities (b) of the Ir OER catalysts

The catalysts were further characterized XANES spectra recorded at the Ir L_{III} edge (Figure 2.10a). XANES spectra show that IrO_2–TiO_2–245 has a white line energy of 11215.7 eV, which is almost identical to IrO_2–150 and lower than IrO_2–TiO_2–Umicore. This suggests that IrO_2–TiO_2–245 is more reduced, which is rationalized via the presence of a larger fraction of Ir^{3+} in the sample. The EXAFS data (Figure 2.10b) of IrO_2–TiO_2–245 and IrO_2–TiO_2–Umicore catalysts significantly differ from each other. The refined Ir–O bond length within the first shell for IrO_2–TiO_2–245 is comparable to IrO_2–150 and 0.024 ± 0.011 Å longer compared to IrO_2–TiO_2–Umicore. Since the Ir–O bond distance within the first shell is highly sensitive to the iridium oxidation state,[7-8] the longer Ir–O distance indicates a lower oxidation state of Ir, consistent with the presence of Ir^{3+} as determined by XANES spectroscopy. The average bond length for Ir–O in IrO_x containing Ir^{3+} has been reported to be roughly 2.02 Å, whereas the bond length of Ir^{4+} in the IrO_2 rutile oxide is closer to 1.98 Å.[3, 9]

In order to investigate the structural changes of the iridium oxide surface as a function of the applied electrode potential, the sample IrO_2–TiO_2–245 was further studied using *operando* XAS spectroscopy at the Ir LIII edge. Fig. 10c–e presents the normalized XANES spectra and EXAFS data recorded during a typical OER polarization measurement. Results of the operando XAS studies of IrO_2–TiO_2–245 material are similar to what we have previously reported for the IrO_2-150. As the electrode potential is stepped into the OER regime the Ir–edge position gradually shifts towards higher energies. The effect is attributed to the fact that IrO_2–TiO_2–245 initially exists as a mixture of Ir3+ and Ir4+ sites and transitions to higher oxidation state upon anodic polarization. The shift to higher edge energies presumably represents a transition from a hydroxide to an oxide terminated surface. The Ir–O bond length obtained from the EXAFS fitting gradually changes from ca. 2.01(1) Å at 1.00 V to 1.99(1) Å at 1.50 V. The shortening of the Ir–O bonds represents the transition of IrO_2–TiO_2–245 from a mixed Ir3+/4+ oxidation state to a structure more heavily populated by Ir4+, which is in line with the XANES data. The observed similarities of the OER properties and *operando* behavior of the IrO_2–TiO_2–245 and high surface area IrO_2-150 indicate that the same catalytic mechanism likely operates for these materials. Surface Ir hydroxyls are the key OER intermediates, and their high initial fraction is probably responsible for enhanced activity of IrO_2–TiO_2–245.

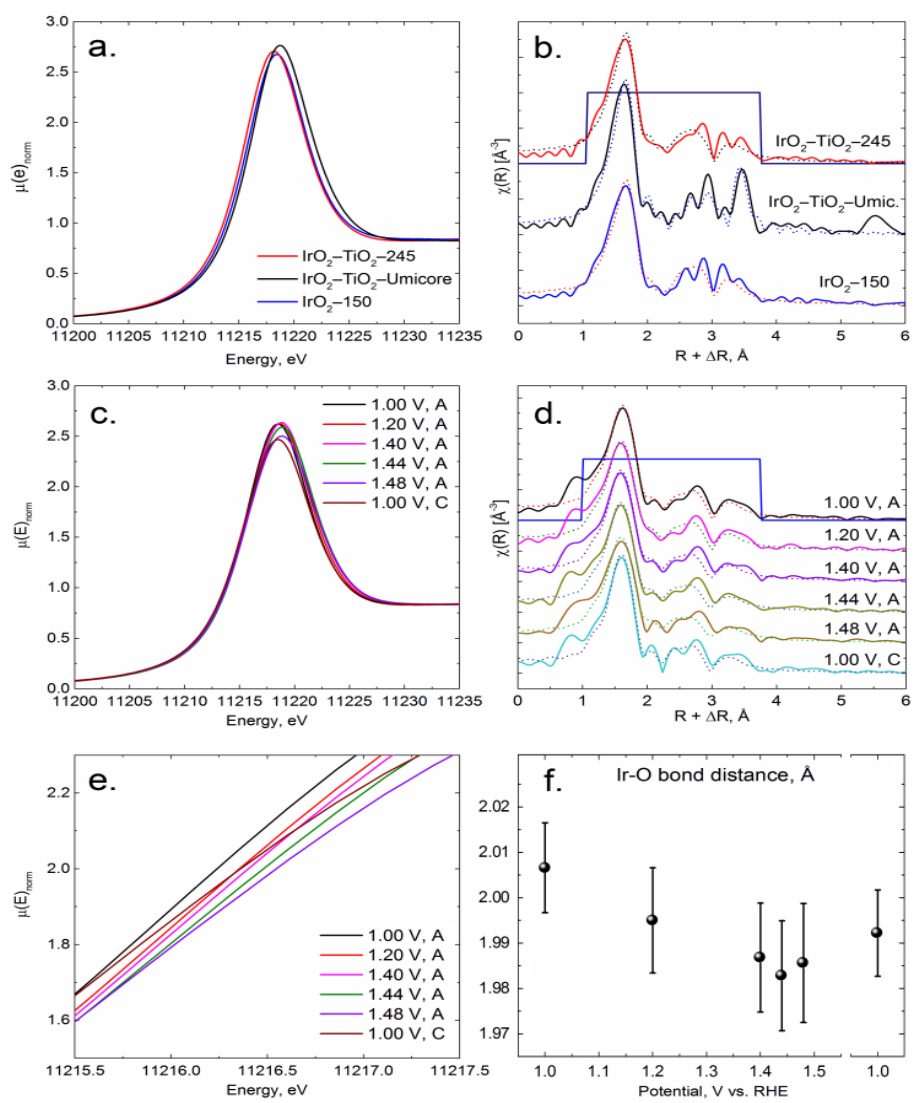

Fig. 2.10 XAS data of OER catalysts: XANES spectra (a); EXAFS data (solid line for experimental data and dotted line for the fits) with k-weight 2 (b). In-situ XAS data of IrO_2−TiO_2−245 recorded at different electrode potentials: XANES spectra (c); EXAFS data (solid line for experimental data and dotted line for the fits) with k-weight 2 (d); an expansion of the XANES absorption peak (e) and the EXAFS-determined Ir−O bond distance as a function of the applied potential (f).

Ir-based pyrochlore catalysts

Further progress was made on synthesis and understanding of the iridium pyrochlore materials for the OER. Use of these materials will allow to further decrease the amount of iridium in the catalysts keeping high activity and stability of IrO_2. Pyrochlores of the general formula $(A, A')_2Ir_2O_{6.5+x}$ (A, A' = Bi, Pb, Y) were synthesized via the modified Adams fusion method and possess the surface areas in the range 10 – 40 $m^2 g^{-1}$ (Table 2.1). Powder X-ray diffraction studies confirm formation of the cubic pyrochlore structure (Figure 2.11a), microscopy studies indicate formation of the nanoparticles with the particle size 50-100 nm.

Table 2.1 Synthesized pyrochlore materials

Pyrochlore	**Surface area,** $m^2 g^{-1}$	**Unit cell parameter** *a*, Å	**XPS composition, mol$_M$%** *A* position	Ir	**Tafel slope,** mV dec^{-1}	J at 1.525 V, A g_{Ir}^{-1}
Bi–Ir	30	10.489(1)	Bi 61.3(9)	38.7(8)	45(1)	21(5)
Y–Ir	21	10.190(5)	Y 58(3)	42(3)	50(2)	38(14)
Pb–Ir	24	10.381(4)	Pb 51.5(6)	48.5(6)	65(1)	10(6)
BiY–Ir	28	10.330(3)	Bi 28.1(8); Y 28.7(6)	43(1)	40(1)	23(5)
BiPb–Ir	38	10.457(2)	Bi 26.0(5); Pb 29(1)	45(2)	42(1)	17(7)
YPb–Ir	11	10.251(3)	Y 33.8(2); Pb 26.6(4)	39.6(1)	41(1)	16(5)

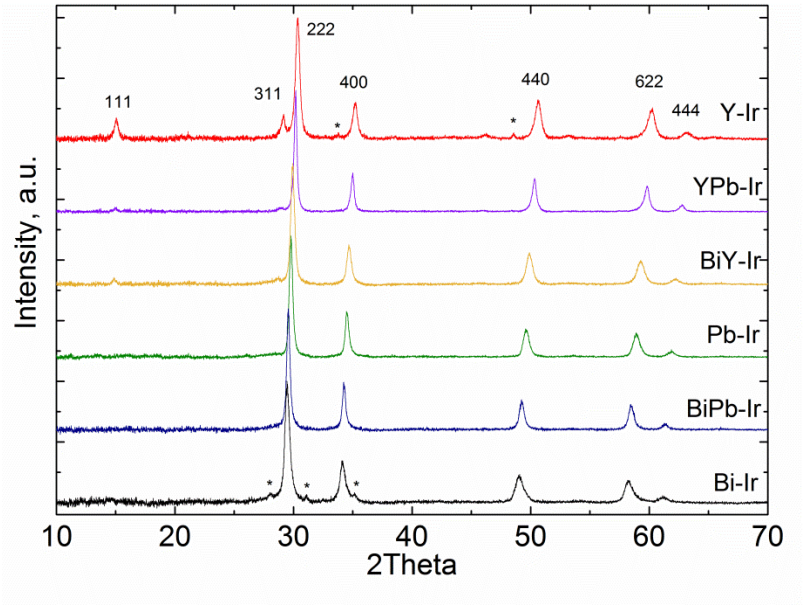

Fig. 2.11 Powder X-ray diffraction data of pyrochlore catalysts

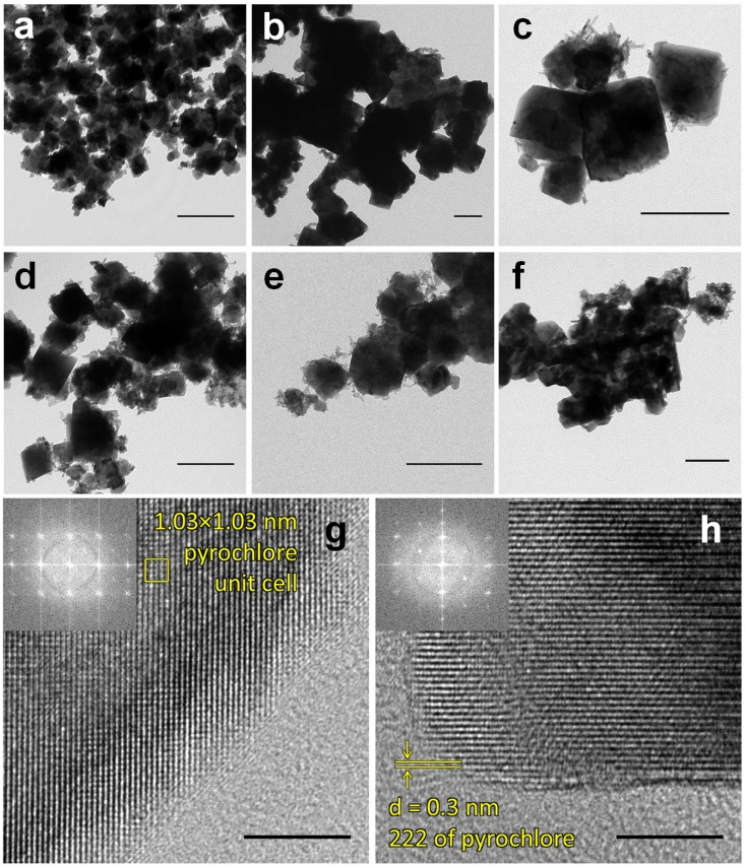

Fig. 2.12 TEM images of Bi−Ir (a), Y−Ir (b), Pb−Ir (c), BiY−Ir (d), BiPb−Ir (e), YPb−Ir (f), scale bars are 100 nm; HRTEM images of Pb−Ir (g) and Y−Ir (h), scale bars are 5 nm, Fourier transformed images are shown as insets.

Obtained pyrochlore materials were tested for the OER in acidic media (Table 2.1 and Figure 2.13). All pyrochlores except Pb−Ir show similar Tafel slopes of 40 - 50 mV dec^{-1}, which is slightly lower than commonly reported values for IrO_2 in acidic environment (ca. 60 mV dec^{-1}). At the same time Pb−Ir shows much higher Tafel slope of 65(1) mV dec^{-1}, which suggests that most likely OER proceeds through a similar mechanism on Bi, Y and mixed pyrochlores, while lead pyrochlore has a different catalytic pathway. In terms of the OER activity, yttrium and bismuth iridium pyrochlores show the best catalytic performance, being more active than IrO_2 of similar surface area (28 m^2 g^{-1}). This suggests that the pyrochlore structure allows improving the specific activity of Ir-based catalysts, i.e. achieving a higher mass activity for comparable active surface area/particle size.

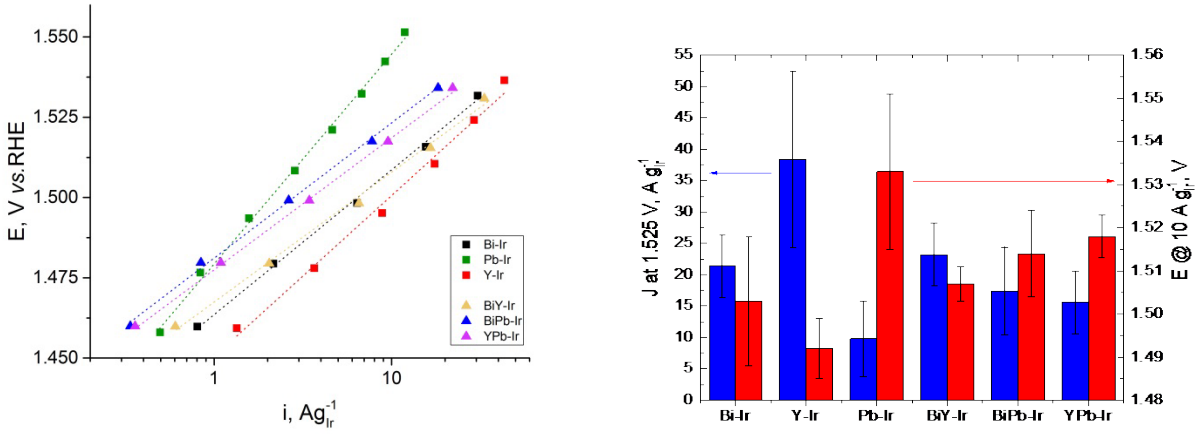

Fig. 2.13 OER Tafel plots showing the steady−state current density recorded after 1 minute in 0.1 M $HClO_4$ (top) and OER activity of the pyrochlore samples as potential, required to achieve a current density of 10 A gIr−1 (bottom)

The stability of pyrochlore samples was evaluated by stepping the sample between a potential close to the open circuit value, i.e. where no OER current is observed (1.00 V), and a potential where an appreciable OER current is observed, i.e. J > 10 A g^{-1} (1.60 V). Such stability tests are intended to simulate the start/stop behavior of a PEM electrolyzer. Shown in Figure 14 are the normalized current densities over the course of 500 potential step cycles for the pyrochlore samples. All the pyrochlore catalysts show fairly good stability over the 500 cycles. The less stable samples, in terms of current drop are the catalysts having a single element in the A site of the phyroclore structure. The samples with two cations occupying the A site show an increase of current density over cycling, which indicates that certain catalyst modification take place under operative conditions but that such changes are beneficial in terms of output current.

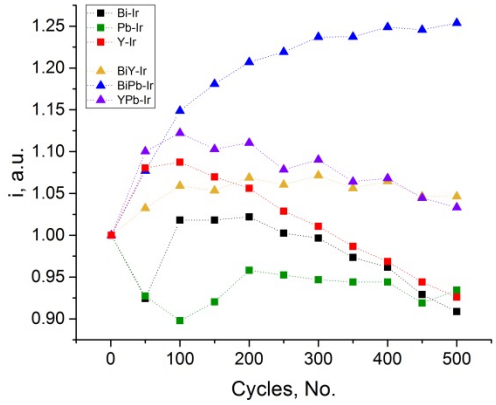

Fig. 2.14 Stability measurements for the pyrochlore samples

DFT calculation for OER catalysts

We aim to identify novel electrodes for the oxygen evolution reaction using Density Functional theory (DFT) and a computational screening approach. An important preliminary step is the evaluation of possible errors present in our simulations. In particular, we would like to define a tested and optimized pseudopotential library which should be accurate and at the same time not too computational costly. Recently, Lejaeghere et al.[10] have proposed a protocol in which they compare the equations of state of several DFT codes with all-electron WIEN2k results for elemental structures for almost all the elements in the periodic table. In their protocol, 7 points around the equilibrium volume of each structure are used to calculate the so-called delta-factor that is defined as the squared deviation of the equation of state calculated using a pseudopotential, that approximate the complicate physics of the core electrons with a smooth curve, with respect to the one using an all-electron code. A small delta indicates that the pseudopotential well approximate the all-electron configuration. In addition, together with the results, they provide all the information necessary to reproduce their data and contribute to the testing of other codes, methods, and pseudopotentials.

Starting from this idea, we have defined a more comprehensive protocol which goes beyond the structural properties provided by the equation of state and includes the verification of the vibrational properties of elemental crystals. Next to the delta-factor, the protocol includes the convergence of phonons, formation energies with respect to the isolated atom and stresses and the computational cost as a function of the wave function cutoff. A combination of these ingredients allows us to define two Standard Solid State Pseudopotential (SSSP) libraries with focus on efficiency and accuracy (SSSP efficiency and SSSP accuracy) for reliable high-throughput calculations at a reduced computational cost. At today we have investigated twelve pseudopotential libraries for the Quantum ESPRESSO code (three projector augmented wave method pseudopotential libraries (PAW: pslibrary.0.3.1, pslibrary.1.0.0 high and low accuracy, and from Topsakal and Wentzcovitch for the rare-earth elements), six ultrasoft (US: GBRV (versions 1.2, 1.4 and 1.5), pslibrary.0.3.1, and pslibrary.1.0.0 high and low accuracy) and two norm conserving (NC: SG15, versions 1.0 and 1.1). Less systematic investigations have been performed for other norm conserving libraries, for example the Pseudo Dojo library. In particular, two of these libraries (GBRV 1.4 and SG15 1.1) are updates of previous versions following up some of our comments. We highly encourage the community to contribute to the verification.

For this purpose, we provide examples of the input structures and files for the calculations as well as the pseudopotential libraries, the relevant output results, the dynamical matrices, and the script to reproduce and update the convergence patterns at the web address http://materialscloud.org/sssp which has been visited more than 4000 times in 6 months. Several groups in Switzerland and around the World are already using the SSSP libraries as standard for their calculations. This project is powered by AiiDA, an infrastructure to automate, store, and share quantum mechanical calculations [http://aiida.net] which is developed and maintained at THEOS, EPFL.

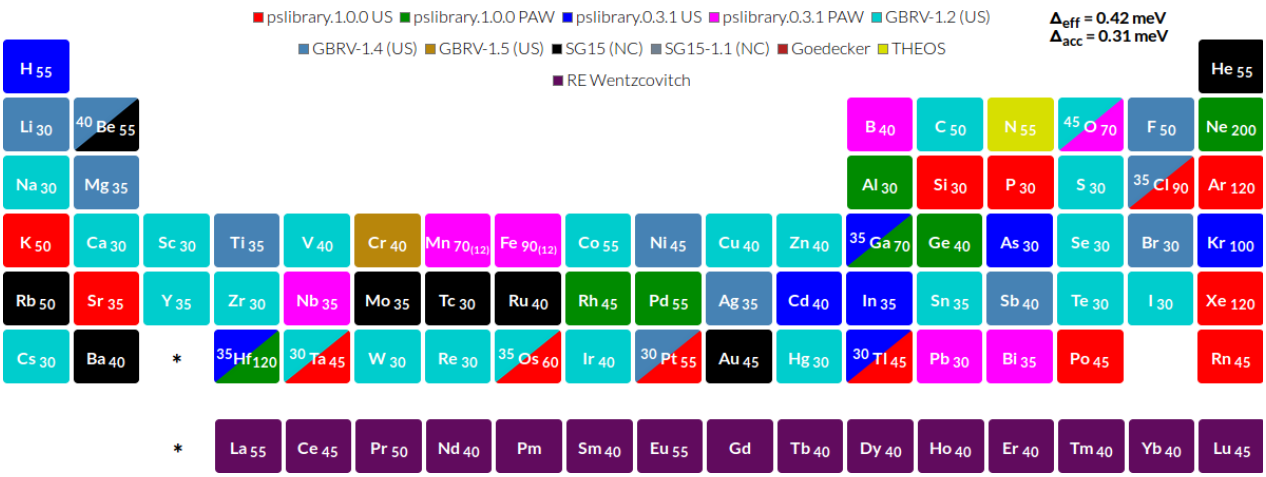

Fig. 2.15 The standard solid-state pseudo potential libraries

Figure 2.15 shows the selected pseudopotentials for the SSSP libraries and the suggested wave function cutoffs. Each square indicates the original library from which the optimal pseudopotentials are taken. For some selected elements, two pseudopotentials have been identified with specific focus on efficiency (top left triangle) and accuracy (bottom right triangle). The SSSP accuracy is the currently available pseudopotential library with the smallest delta. The convergence patterns for around 80 elements are all available on line and are constantly updated with the expansion of the protocol to include, for example band structures and with more tested pseudopotential libraries. This study is also a part of a broader effort that a group of 70 scientists is making to systematically investigate the verification and validation of quantum mechanical calculations.

Consequently, in order to identify novel catalysts for the oxygen evolution reaction (OER) the first step has been to investigate by means of Density Functional Theory a handful of pyrochlores with formula $A_2Ir_2O_7$ (with A = Y, Bi, or Pb). Later on, we have performed a high-throughput screening of rare-earth Ir-pyrochlores and selected few interesting candidates for experimental synthesis and characterization. Both the projects have been carried out in close collaboration with the group of Christophe Copéret (ETHZ, for the synthesis) and Thomas Schmidt (PSI, for the characterization).

Regarding the first point, we have investigated the phase stability and Pourbaix diagrams of $A_2Ir_2O_7$ (with A = Y, Bi, Pb and their combinations). In the phase stability diagram, the convex hull defines the stability frontier at 0K and is obtained by comparing the total energies of the pyrochlore with all the competing phases in which the material can separate. Pourbaix diagrams are used to address the issue of stability in water as a function of pH and electrochemical potential. The scheme used to produce these diagrams has been explained by Castelli et al.,[11] and already used, together with the phase diagrams, to identify novel materials for light harvesting in a water splitting device. All the structures (pyrochlores and the competing phases, as present in the Materials Project database) have been fully optimized using PBEsol as exchange-correlation functional in the Generalized Gradient Approximation and the pseudopotentials from the Standard Solid State Pseudopotential library (SSSP accuracy, which has been a preliminary step for the theoretical part of the project and has been recently published[12] as implemented in the Quantum ESPRESSO package. The phase diagram module present in the Atomic Simulation Environment (ASE) has been used to generate the phase and Pourbaix diagrams. Our goal here was to support and confirm the experimental results regarding the stability of various compounds under different conditions.

An example is shown in Figure 2.16 and 2.17. Figure 16 on the left shows the phase diagram: materials that are stable are on the convex hull frontier and are indicated with green dots. Figure 16 on the right shows the Pourbaix diagram for PbIrO as a function of pH and potential. The candidate pyrochlore material is stable for a positive potential at all the considered pHs.

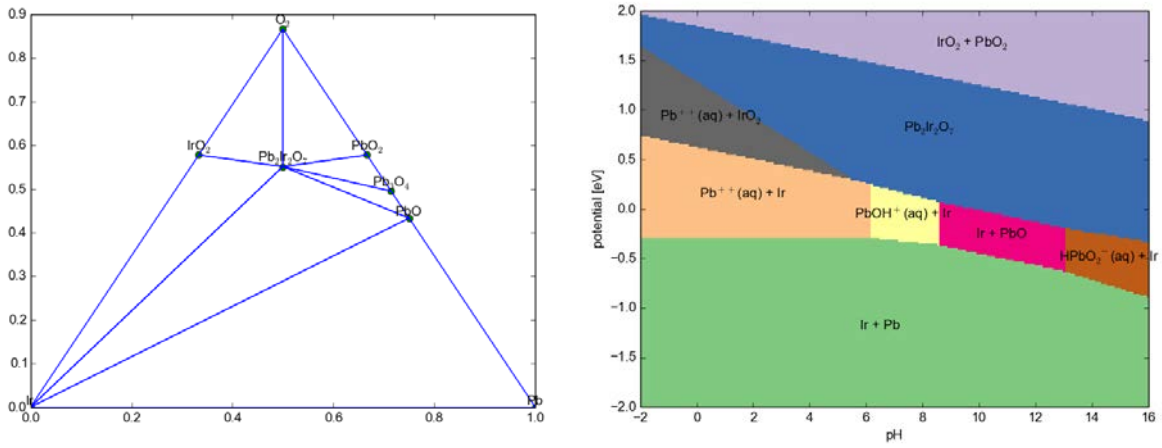

Fig. 2.16 Phase and Pourbaix diagram of $Pb_2Ir_2O_7$

In most of the cases, our stability analysis agrees with experiments and helps in understanding the reason why a possible catalyst is seen unstable. We consider also important to go beyond the analysis of available catalysts and we are interested in finding novel materials that can be used as catalysts for OER.

We thus started from what we have learned so far for the pyrochlore structure and expand the search space to include the rare-earth elements in the A side of the pyrochlore, and Ir, Ru, and Rh for the B side. We then have to identify useful descriptors that connect the calculated quantities with the measured properties that we would like to have in a candidate compound. The first descriptor is stability against phase separation and corrosion in water. For this, we use the phase and Pourbaix diagrams, as shown before. In addition, we would like the candidate material to be conductive.

In fact, a good conductivity is required to have the possibility to transfer electrons between the fragments and thus to have the reaction running. Many efforts have been made to evaluate the conductivity in a highly-accurate way. All this methods are a bit too expensive to be used in a screening project. That for, we consider a necessary condition for a material to be a possible candidate if the pyrochlore has at least one band crossing the Fermi level, i.e. it is not a semiconductor. This is of course not optimal, but can give us an initial idea of where to look for. An example of the the three descriptors is shown in Figure 17. $Yb_2Ir_2O_7$ is stable against phase dissociation and corrosion in water and it has bands crossing the Fermi level.

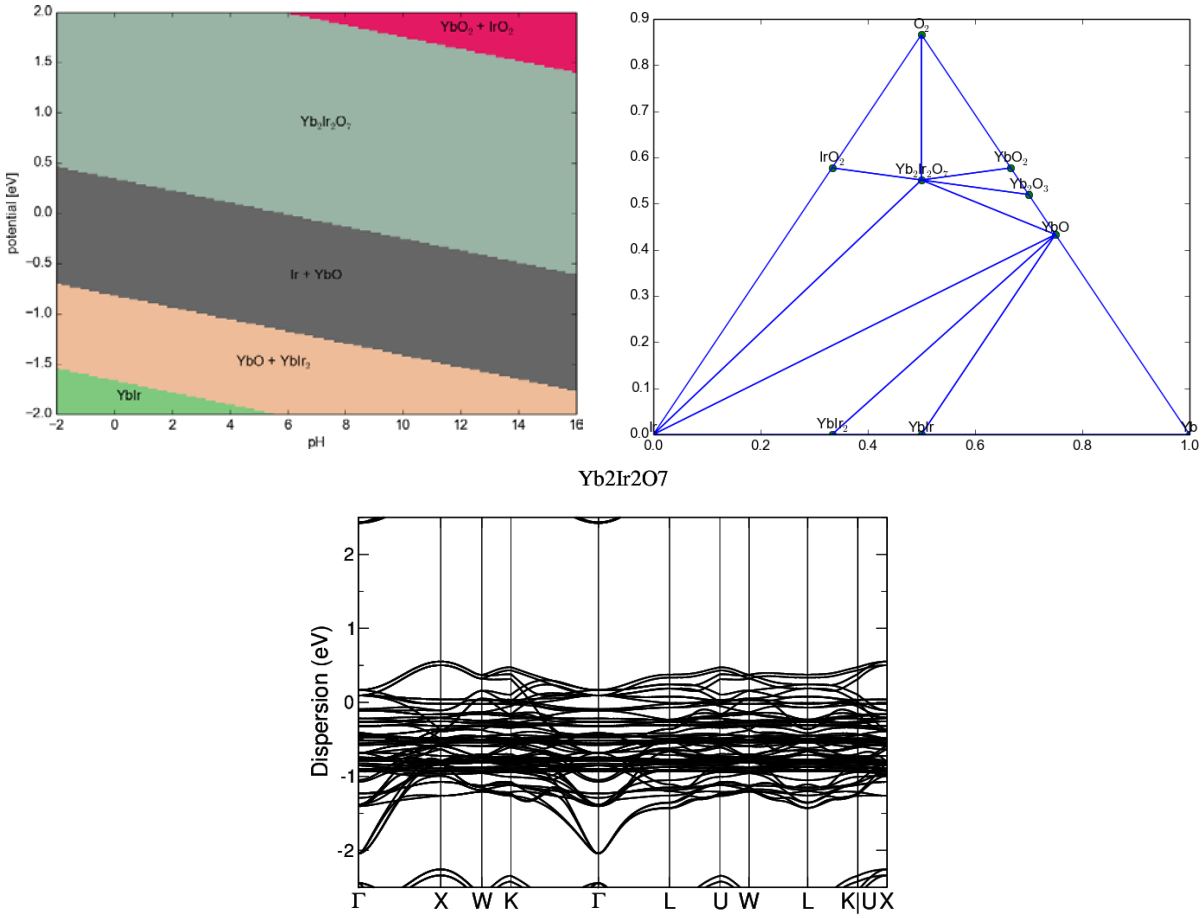

Fig. 2.17 Descriptors used to identify novel catalysts for OER: Phase and Pourbaix diagrams and band structures for $Yb_2Ir_2O_7$

In addition to these studies of technologically relevant systems we are as well working on improving and assessing the accuracy of the current methodology of describing electrochemical systems based on ab-initio calculations. On the one hand, we investigated the accuracy of theoretically predicted Pourbaix diagrams. On the other hand, we studied electrochemical interface properties of coinage metals and Pt in water using a methodology that goes beyond the computational hydrogen electrode approach.

As elaborated above, Pourbaix diagrams allow to analyze the stability of solid materials against decomposition in water at given pH and potential. Errors in the DFT 0 K energies can, however, have significant influence on the predicted stability diagrams. As an example, the formation free energy of liquid water is wrong by approximately 0.21 eV within PBE. Furthermore oxidation energies of many metals can be wrong even by a larger amount (see Fig. 18, left panel). A viable method to correct for these errors is a shift of elemental reference energies, typically of the molecular reference species. In the case of Pourbaix diagrams, these are the H_2 and the O_2 molecular 0 K ground state energies. Furthermore, vibrational free energy and other temperature contributions are typically not taken into account in most phase stability predictions. In order to get a better understanding of an optimum choice of parameters for more accurate Pourbaix diagrams, we augmented DFT 0 K total energies with the vibrational free energy contributions from a DFT-parametrized Debye model. A preliminary analysis showed that temperature effects at 300 K can be determined up to an accuracy of approx. 10 meV/atom using this approach (see Fig. 2.18, right panel).

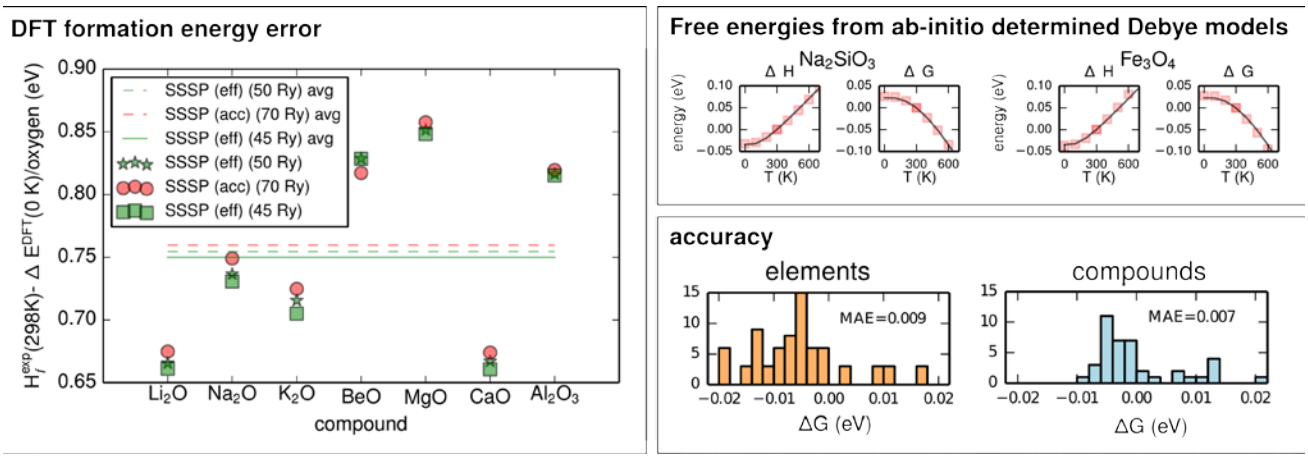

Fig. 2.18 Left panel: Formation energy error of simple s and p metal oxides when determined from PBE. Right panels: (top) Accuracy of the Debye model for the determination of free energies at elevated temperatures. The red squares correspond to experimental values. (bottom) Histograms of the error distributions of Debye model free energies at room temperature.

In Fig. 2.19 we compare the Pourbaix diagrams determined with two approaches, shifting only the O_2 energy to reproduce the water formation energy - the standard method, also used for the Pourbaix diagrams of Fig. 2.16 and 2.17 – and by shifting both the O_2 and H_2 molecular reference energies to reproduce at the same time water as well as the formation enthalpies of the simple oxides of Fig. 2.18. In both cases we use the estimated Debye model to also include vibrational temperature effects of the solids. It should be noted that those shifts are indeed considerable and considerably different from each other (O_2 (0.214 eV) vs O_2 + H_2 (0.894 eV / -0.340 eV). This results in different phase stability and Pourbaix diagrams.

As an example, the underestimation of the stability of Al_2O_3 in PBE leads to a Al Pourbaix diagram that shows no region where Al_2O_3 is stable when one only corrects for O_2. However, the O_2 + H_2 correction scheme seems to agree rather well with experiment. On the other hand the O_2 corrected Cu Pourbaix diagrams seem to be slightly better compared to the O_2 + H_2 corrected versions. Furthermore ASE uses a slightly different construction scheme of Pourbaix diagrams that exclude potentially metastable hydrides and hydroxides (See Cu Pourbaix diagrams). In terms of interpretation, hydride and hydroxide formation, however, seems to exhibit valuable information e.g. for experiments at negative potentials, e.g. under hydrogen evolution or CO_2 reduction conditions. At the moment, we are evaluating in collaboration with the Wolverton group (Northwestern University) the accuracy of formation energies of compounds in order to understand better how and when to apply which correction schemes to DFT energies to obtain more reliable phase diagrams. To this point we think that for strong oxides, with large formation energy errors, it is advisable to go beyond a simple O_2 correction scheme.

b) Catalysts for the CO_2 Reduction Reaction

For the electrochemical reduction of CO_2, also named the co-electrolysis of CO_2 and water, the key challenges are to increase the overall catalyst activity and to increase the product selectivity towards one desired product. In order to understand both quantities, the first part of the project was to setup and built in-situ product analysis measurement tools being essential to understand both activity and selectivity for a given catalyst.

Operando DEMS setup for CO_2-electroreduction

Differential Electrochemical Mass Spectrometry (DEMS) is as an excellent tool for the in-operando quantification of the volatile species produced upon CO_2 reduction. Figure 2.20 displays a scheme and a partial picture of the custom-made DEMS setup designed by our group. It consists of a two-compartment electrochemical flow cell (discussed below) separated from the first vacuum chamber through a PTFE porous membrane of 0.02 µm porosity that allows for the crossing of volatile products. An aperture of 0.2 mm diameter results in a differential pressure between this first and the second vacuum chamber (at $\approx 10^{-2}$ and $\approx 10^{-5}$ mbar, respectively), whereby the latter holds the ion source and quadrupole mass analyzer.

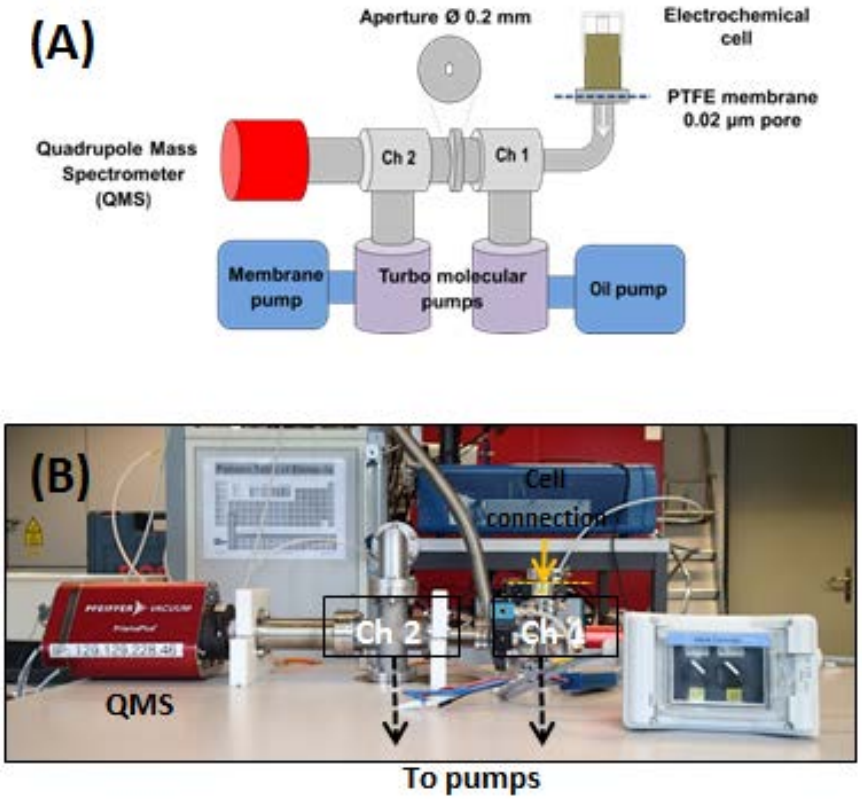

Fig. 2.20 Scheme (A) and partial photograph (B) of the custom-made DEMS-setup designed by our group.

Following their installation in our laboratory, the mass spectrometer and the vacuum system are currently fully operational. Nevertheless, the DEMS setup also includes the electrochemical cell, which in this case consists of a dual thin-layer flow cell. The cell's operating principle is illustrated in Figure 21. In brief, the electrolyte of choice is flowed through the cell's inlet and hits the surface of the working electrode in a jet-like fashion. The electrolyte carrying the reaction products then escapes this upper cell compartment through four lateral channels that direct it to the second chamber, which is in terms connected to the vacuum system through the porous PTFE-membrane described above. Volatile species cross this membrane and are analyzed by the mass spectrometer, whereas the electrolyte flows to the outlet capillary and leaves the cell.

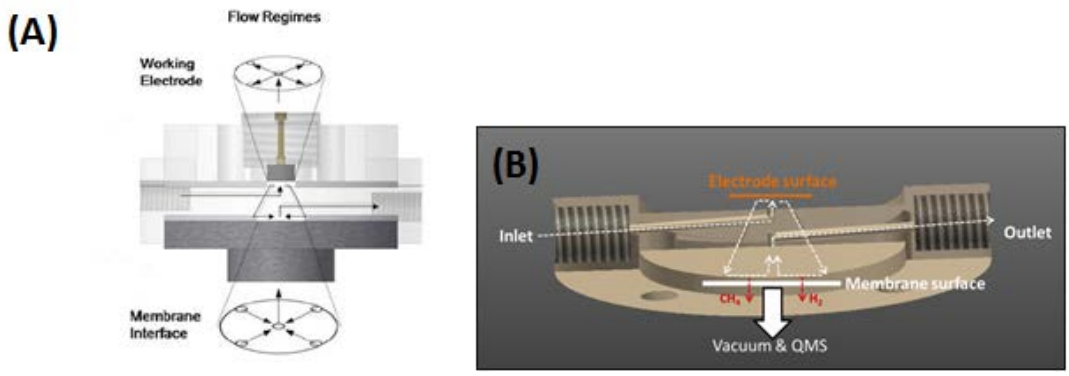

Fig. 2.21 Schemes of the dual thin-layer flow cell implemented in our DEMS-setup.5

A detailed description of the complete flow cell, including the electrolyte injection system and cell assembly, is provided in Figure 2.22. Electrolyte flow from the inlet capillary to the working electrode chamber is granted by a syringe filled with the saturated electrolyte and connected to the cell with FEP tubing. As for the counter and reference electrodes, they were connected through FEP-parts (T's and valves) to the cell's inlet and outlet tubing, respectively.

Unfortunately, our preliminary electrochemical measurements with this configuration suffered from a very high resistivity (≈ 40 kΩ) and from the intrusion of oxygen (air) into the system. In an effort to circumvent this last issue, we have recently proceeded to re-design some of the setup's components, as to improve its tightness/sealing. As for the cell's high resistivity, we have also implemented modifications in the design of the electrolyte-inlet and outlet tubing that should result in a reduction of the distances between the electrodes. While we expect a 2-4 fold reduction of these ohmic losses using this approach, the high resistance is an intrinsic property of the cell caused by the used of narrow capillaries. Ultimately, though, this should not prevent us from performing proper electrochemical measurements using the ohmic compensation feature included in the potentiostat devoted to this project.

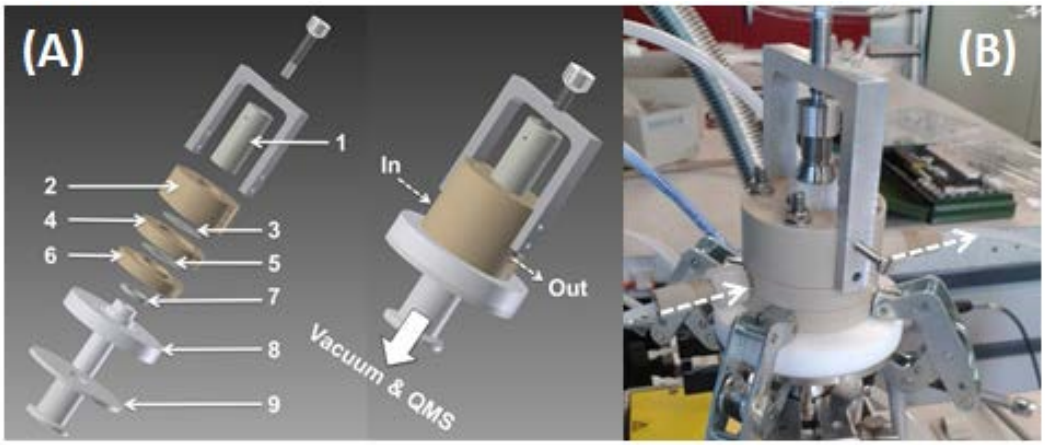

Fig. 2.22 Scheme of the dual thin layer flow cell (A), consisting of the PTFE working electrode holder (1), the PEEK working electrode compartment with a volume of 24 µL (2), an upper PTFE gasket (3), the PEEK flow distributor (4), a lower PTFE gasket (5), the PEEK membrane compartment (46 µL, 6), the PTFE membrane and membrane and frit support (7,8), and the stainless steel connector to the vacuum system (9). The right-hand panel in (b) displays an actual picture of the setup.

Preliminary CO_2-electroreduction measurements

We have performed some preliminary electrochemical measurements using a standard three-electrode glass cell. More precisely, a polycrystalline Cu disk working electrode of 10 mm diameter was mechanically polished on a microcloth with 0.3 and 0.05 µm Al_2O_3-suspensions. The disk was then sonicated three times in five minute intervals in ultrapure water (18.2 MΩ·cm, ELGA) and assembled onto the electrochemical cell connected to the DEMS (Figure 2.23). A flame-annealed Pt mesh was used as the counter electrode, along with a $Hg/HgSO_4$ reference. The electrolyte was 0.1 M $KHCO_3$ saturated with CO_2 for 30 min prior to the measurement. After this saturation, the working electrode was pressed on the PTFE membrane as to allow collection of the volatile reduction products. This approach results in a poorly-defined diffusion of electrolyte, CO_2 and products towards and away from the electrode surface. However, it did allow for the observation of qualitative reactivity trends described in the following.

In an exemplary experiment, potential steps were applied to the system, starting from -0.5 V/RHE and decreasing by 50 mV in each step. Every step was 5 min long and between two steps, the potential was held for 5 minutes at -0.5 V/RHE. Different mass fractions were recorded by the MS during the reaction. Figure 4 shows the time evolution of the potential profile and the mass fragment signals m/z=2 (H_2^+), m/z=15 (CH_3^+) and m/z=44 (CO_2^+). Both H_2 and hydrocarbon production are observed, while CO_2 gets progressively consumed, confirming the viability of the vacuum and MS-setup.

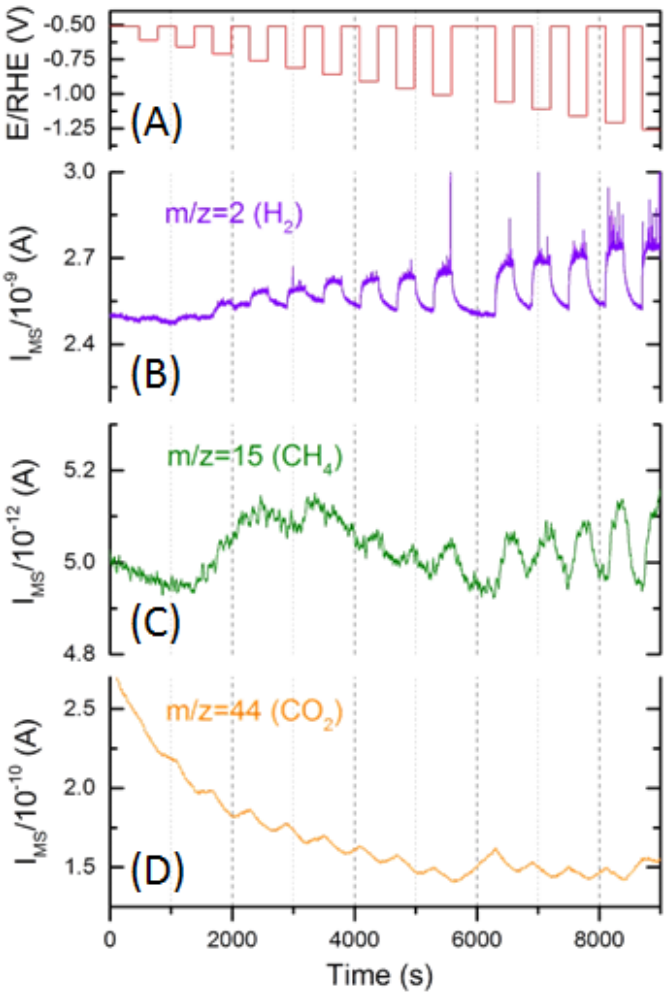

Fig. 2.23 Potential steps in cathodic region of Cu (A). Ion current recorded by MS for mass fraction m/z=2 (B), m/z=15 (C) and m/z=44 (D).

In summary, we have succeeded at designing and implementing a vacuum and mass spectrometry system that already allows for the in-operando detection of the volatile species evolved upon CO_2-electroreduction. We expect that these measurements will become quantitative as soon as we will receive and verify the new pieces recently designed to suppress air intrusion and decrease ohmic drop within the electrochemical flow cell.

Quantification of Cu roughness factor

In an initial effort to validate the operation of the DEMS-setup, we attempted to study the reduction of CO_2 on polycrystalline copper (Cu_{PC}), which has historically gathered a lot of attention due to the possibility of yielding added-value hydrocarbons like ethylene or methane.

Prior to this analytical work, though, we developed a procedure to quantify the roughness factor (RF) of the Cu_{PC}-surface, which is of great importance for the comparison with other Cu-based catalysts (e.g., in the form of nanoparticles) envisaged in a later stage of this project. Inspired by previous studies dealing with Cu single crystals,[4,5] we used rotating ring disk electrode (RRDE) voltammetry to estimate the RF of Cu_{PC} from the charge associated to the (sub)monolayer adsorption of Pb at potentials positive of the Pb^{2+}/Pb^0 equilibrium (i.e., lead underpotential deposition — Pb_{upd}).

The experiments were performed in 0.01 M $HClO_4$ with 50 □ M Pb^{2+} and 100 □ M Cl^-, whereby the chloride required in order to speed up the adsorption process implies an added adsorption/desorption charge that must be accounted for upon RF-quantification. This was done by scanning the disk between 0.3 and — 0.25 V vs. RHE while rotating the electrode at a given speed and holding the ring at a potential of - 0.25 V vs. RHE, at which Pb-plating is under diffusion control and takes place without Cl^--coadsorption. Thus, as shown in Figure 2.24, the *shielded* ring current (j_{ring}) recorded in this fashion is selectively sensitive to the changes in the local Pb^{2+}-concentration caused by the adsorption and desorption of lead (and not of Cl^-) at the disk. As a result, one can estimate the disk charge exclusively related to Pb_{upd} from the corresponding ring charges at ≈ 0 and 0.1 V vs. RHE in Figure 2.24 (which account for 15 °C).

When the RRDE's collection efficiency (0.24) and the disk's geometrical area (0.196 cm_{geom}^{-2}) are taken into consideration, the resulting (Cl^--unaffected) Pb_{upd}-charge of 320 □ $C{\cdot}cm_{geom}^{-2}$ yields a reasonable RF of 1.3 $cm_{Cu}^{2}{\cdot}cm_{geom}^{-2}$ (assuming a normalization charge of 480□ $C{\cdot}cm_{Cu}^{-2}$ and a lead-on-copper packing density[4,5] of 0.53).

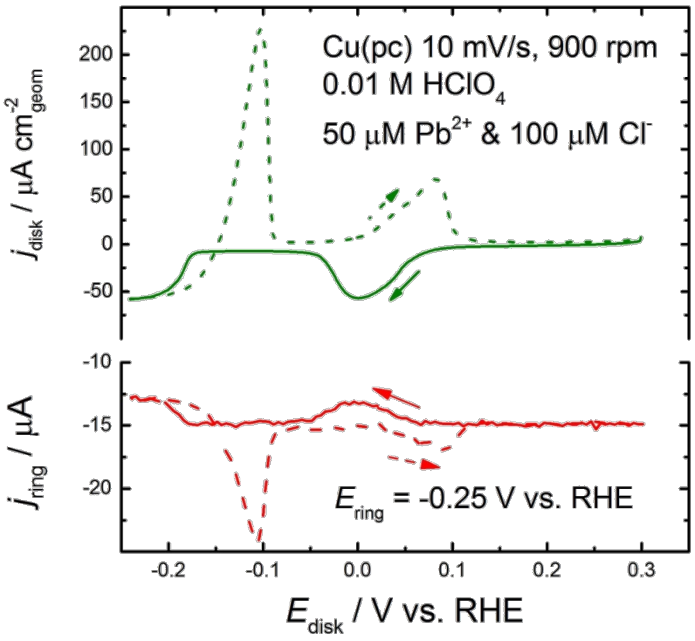

Fig. 2.24 Disk and ring currents (jdisk, jring) recorded on an RRDE consisting of a CuPC-disk and a Pb-covered Pt-ring, whereby the charge related to the shielded jring can be used to quantify the roughness factor of the copper disk.

After developing this RF-quantification procedure, we attempted to study the reduction of CO_2 on Cu_{PC} using our DEMS-setup. Unfortunately, the large ohmic drop of ≈ 15 kΩ intrinsic to the electrochemical flow cell geometry restricts its operation to relatively small faradic currents (< 5 mA cm_{geom}^{-2}) within which only H_2 is produced and detected (not shown). We are currently trying to circumvent this issue by implementing a booster that should allow us to assess faradic processes beyond the limited potential window of ± 10 V normally accessible with our potentiostat.

DEMS results of CO_2 reduction on Gold electrodes

Looking for an alternative way of proofing the DEMS-setup under conditions relevant to CO_2-electroreduction, we shifted our interest towards Au-based catalysts on which relatively smaller overpotentials are needed to produce CO (along with minor amounts of formate and H_2 as a by-product). As illustrated in Figure 25, the reduction of CO_2 in 0.5 M $KHCO_3$ (with 15 % CO_2 in Ar) resulted in the expected evolution of H_2 (m/z=2) and consumption of CO_2 (m/z=44), along with an increase in m/z=28 (relatable to both CO_2 and CO) that univocally points at the production of carbon monoxide.

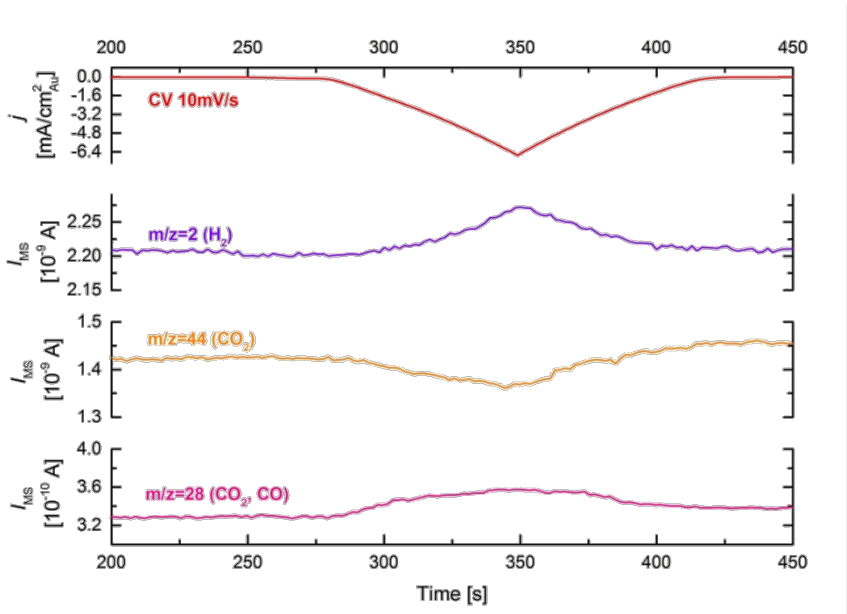

Fig. 2.25 Cyclic voltammogram (CV at 10 mV·s-1, top) and corresponding DEMS m/z-signals recorded on a polycrystalline gold disc embedded in a thin layer flow cell fed with 15 µL·s-1 of 0.5 M $KHCO_3$ with 15 % CO_2 in Ar.

Beyond this qualitative result, subsequent measurements were performed by holding the potential at a given potential for 30 seconds and recording the current and the m/z=2 (i.e., H_2) signal. The latter was then related to a hydrogen-specific charge (Q_{H2}) through a regression line derived from a preliminary H_2-evolution measurement performed in the absence of CO_2 (not shown). Assuming that the overall charge in each potential step is a combination of the moles of CO and H_2 produced (i.e., $Q_{total} = Q_{CO} + Q_{H2}$), and considering the corresponding value of Q_{H2} derived through the regression line, we could estimate Q_{CO} and the Faradic efficiency for this product [$FE(CO)=Q_{CO}/Q_{total}$]. The results obtained following this approach are plotted in Figure 2.26.

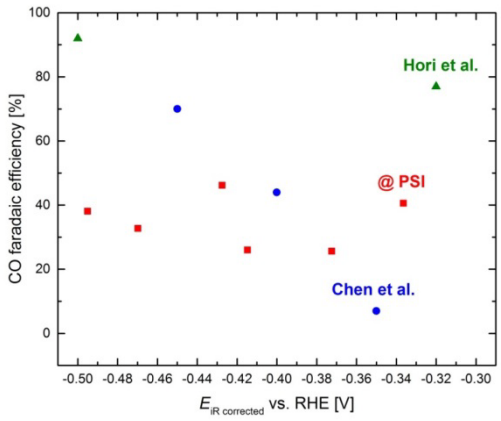

Fig. 2.26 Evolution of the CO-specific faradaic efficiency [FE(CO)] with the iR-corrected potential upon stepwise, chronoamperometric CO_2-reduction on AuPC (0.5 M $KHCO_3$ with 15 % CO_2 in Ar, 15 □ L·s-1), and comparison to the result of Chen et al. 13 or Hori et al.14

The limited agreement between our results and those reported in the existing literature (cf. Figure 26) could arise from differences in the cell/electrode configuration and/or electrolyte composition, along with imprecisions in the iR-correction and the back-calculation of FE(CO) from the DEMS H_2-signal. For this purpose, we are currently implementing an appropriate calibration add-up, and complementing our DEMS-results with RRDE-voltammetry using a Pt- or an Au-ring to selectively detect H_2 or CO, respectively.

Economical model

Beyond the kinetic and selectivity constrains associated to the electroreduction of CO_2, the mere identification of the reaction products of interest (i.e., cost-competitive) is of great importance to set performance milestones and assess the commercial feasibility of co-electrolysis technology. In sight of the limited number of studies devoted to this relevant topic, we decided to perform such a cost analysis by considering the main CO_2-reduction products described in the literature (i.e., H_2, CH_4, C_2H_4, CO, $HCOO^-$ and CH_3OH) and summarized in Table 2.2,[15] in which cost figures for well-established chemical synthesis routes are compared to estimates for the electrochemical production of each specific product. For the latter purpose, we considered the production of H_2 in alkaline water electrolyzers (AWEs), which currently attain daily productions in the order of ≈ 1000 kg_{H2} at prices of ≈ \$4 kg_{H2}^{-1} (on the basis of electric energy costs of \$0.05 kWh^{-1}), yielding an operative cost of ≈ \$167 h^{-1}. Assuming that co-electrolysis cells were to attain capital costs and operating currents (≈ 0.2 $A{\cdot}cm_{geom}^{-2}$) similar to those of AWEs, the above, AWE-based H_2-production volume (V_{H2}, in $kg{\cdot}h^{-1}$) can be converted into the respective values for each CO_2-reduction product (V_{CxHyOz}, in $kg{\cdot}h^{-1}$) using Equation 1:

$$V_{CxHyOz} = V_{H2} \cdot \frac{M_{CxHyOz}}{M_{H2}} \cdot \frac{n_{H2}}{n_{CxHyOz}} \qquad [1]$$

where M refers to the product's molar mass (in $g{\cdot}mol^{-1}$), and n is the corresponding number of electrons exchanged to produce 1 mol of product (i.e., 2 for H_2, CO or $HCOO^-$, 6 for CH_3OH, 8 for CH_4, and 12 for C_2H_4).

Table 2.2 Current and estimated co-electrolysis production costs for the main (i.e., more abundant) CO_2-reduction products described in the literature.

Product	Current market price [$\$\cdot kg^{-1}$]	Current production volume [$Mt\cdot year^{-1}$]	Co-electrolysis production costs [$\$\cdot kg^{-1}$]	Production volume per co-electrolysis unit [$Mt\cdot year^{-1}$]
H_2	2 – 4	65	4	0.0003
CH_4	< 0.08	2,400	4	0.0007
C_2H_4	0.8 – 1.5	141	3.2	0.0009
CO	0.65	210,000	0.54	0.005
$HCOO^-$/HCOOH	0.8 – 1.2	0.8	0.34	0.008
CH_3OH	0.4 – 0.6	100	1.4	0.002

Considering these computed production volumes and assuming that the energy efficiency of a co-electrolyzer would be ≈ 50 % that of an AWE (setting an operating cost of ≈ $\$334\ h^{-1}$), the resulting production costs of all CO_2-reduction are listed in Table 1. The latter unveils that products like CH_4, C_2H_4 and CH_3OH (with co-electrolysis production costs of ≈ \$4, ≈ \$3.2 and ≈ $\$1.4\ kg^{-1}$, respectively) will hardly become cost-competitive with the conventional production routes (at < \$0.08, ≈ \$1.5 and ≈ $\$0.6\ kg^{-1}$, respectively).

On the other hand, the projected production costs of ≈ $\$0.54\ kg^{-1}$ for CO (which, in combination with H_2, constitutes a chemical precursor for numerous industrial processes) are below the current market price of ≈ $\$0.65\ kg^{-1}$. Additionally, the electrosynthesis of formate (which would need to be protonated into formic acid prior to application) is ≈ 2-fold less expensive than the current market price of HCOOH. Considering the limited size of this market (≈ $0.8\ Mt\cdot year^{-1}$) the electrochemical conversion of CO_2 into formate / formic acid has a greater potential than that into CO to become economically competitive.

DEMS results of CO_2 reduction on Gold particles

Having identified the products of interest ($HCOO^-$, CO), and considering the need for high surface area catalysts in order to attain co-electrolysis implementation, we proceeded to study the reduction of CO_2 on self-assembled gold nanoparticles (so called "Au-black") using our online electrochemical mass spectrometry (OEMS) setup. Figure 27 features a comparison of the MS-response upon potential scans on polycrystalline gold (AuPC) and Au-black, which in both cases display a rise in the m/z=2 signal commensurate with the evolution of H_2. On the other hand, while the decrease in m/z=44 and corresponding increase in m/z=28 observed for Au_{PC} are unambiguously indicative of the reduction of CO_2 to yield CO, the measurement on Au-black does not show any indications of CO_2-consumption.

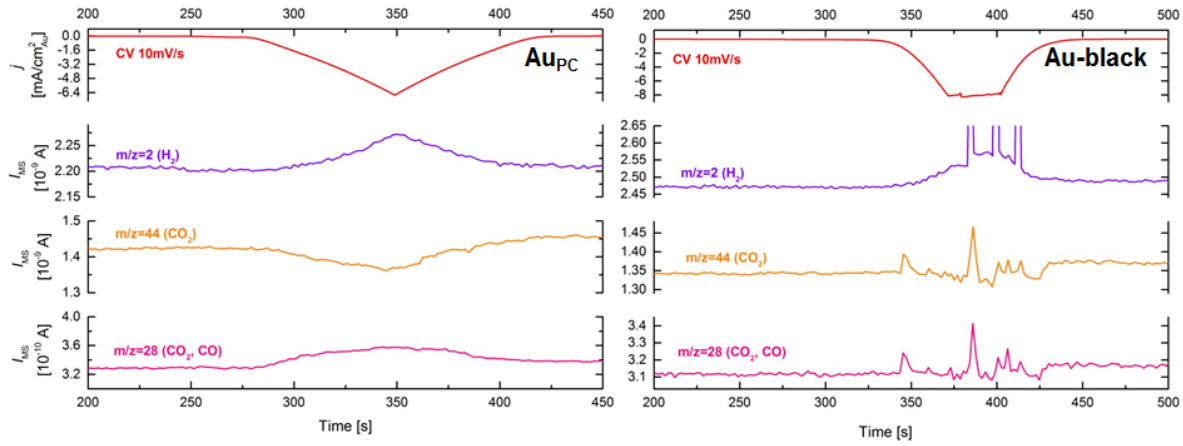

Fig. 2.27 Online electrochemical mass spectrometry results for the reduction of CO_2 on polycrystalline gold (AuPC, left panel) and self-assembled gold nanoparticles (Au-black, 100 □ gAu·cmgeom−2, right). The measurements were performed in 0.5 M KHCO3 saturated with a 15 % volumetric mixture of CO_2 in Ar, at a flow rate of 15 □ L·s−1.

The same qualitative behavior was observed when the OEMS-measurements were performed as short-termed potential holds (not shown), from which one can additionally infer the reaction's Faradic efficiency (FE – see last year's report). Interestingly, this approach yielded FE-values < 100 % for the evolution of H_2 at all tested potentials, indicating that a fraction of the exchanged charge is devoted to a process other than this reaction (or the reduction of CO_2 disregarded above). Alternatively, this "missing charge" could be assigned to the reduction of the Au-surface, which may originally consist of a thick oxide layer – a possibility that is currently under investigation in our laboratory. Regardless of this aspect, the shift of the reaction's selectivity towards H_2-evolution upon transitioning from quasi-flat surfaces to Au-nanoparticles is consistent with recent studies that have stablished a link between the reaction's selectivity and the relative abundance of under-coordinated surface sites.[16]

References

1. Fabbri, E.; Habereder, A.; Waltar, K.; Kotz, R.; Schmidt, T. J., Developments and Perspectives of Oxide-Based Catalysts for the Oxygen Evolution Reaction. Catalysis Science & Technology 2014, 4, 3800-3821.
2. Abbott, D. F.; Lebedev, D.; Waltar, K.; Povia, M.; Nachtegaal, M.; Fabbri, E.; Copéret, C.; Schmidt, T. J., Iridium Oxide for the Oxygen Evolution Reaction: Correlation between Particle Size, Morphology, and the Surface Hydroxo Layer from Operando Xas. Chem. Mater. 2016, 28, 6591-6604.
3. Pauporté, T.; Aberdam, D.; Hazemann, J.-L.; Faure, R.; Durand, R., X-Ray Absorption in Relation to Valency of Iridium in Sputtered Iridium Oxide Films. J. Electroanal. Chem. 1999, 465, 88-95.
4. Oakton, E.; Lebedev, D.; Fedorov, A.; Krumeich, F.; Tillier, J.; Sereda, O.; Schmidt, T. J.; Copéret, C., A Simple One-Pot Adams Method Route to Conductive High Surface Area Iro2–Tio2 Materials. New J. Chem. 2016, 40, 1834-1838.
5. Bernt, M.; Gasteiger, H. A., Influence of Ionomer Content in Iro2/Tio2electrodes on Pem Water Electrolyzer Performance. J. Electrochem. Soc. 2016, 163, F3179-F3189.
6. Binninger, T., et al., Electrochemical Flow-Cell Setup for in Situ X-Ray Investigations. J. Electrochem. Soc. 2016, 163, H906-H912.
7. Cruz, A. M., et al., Iridium Oxohydroxide, a Significant Member in the Family of Iridium Oxides. Stoichiometry, Characterization, and Implications in Bioelectrodes. J. Phys. Chem. C 2012, 116, 5155-5168.
9. Pfeifer, V., et al., The Electronic Structure of Iridium and Its Oxides. Surface and Interface Anal. 2016, 48, 261-273.
10. Lejaeghere, K.; Van Speybroeck, V.; Van Oost, G.; Cottenier, S., Error Estimates for Solid-State Density-Functional Theory Predictions: An Overview by Means of the Ground-State Elemental Crystals. Critical Reviews in Solid State and Materials Sciences 2014, 39, 1-24.
11. Castelli, I. E.; Thygesen, K. S.; Jacobsen, K. W., Calculated Pourbaix Diagrams of Cubic Perovskites for Water Splitting: Stability against Corrosion. Topics in Catalysis 2014, 57, 265-272.
12. Lejaeghere, K., et al., Reproducibility in Density Functional Theory Calculations of Solids. Science 2016, 351, 1415-U81.
13. Chen, Y.; Li, C. W.; Kanan, M. W., Aqueous Co2 Reduction at Very Low Overpotential on Oxide-Derived Au Nanoparticles. J Am Chem Soc 2012, 134, 19969-19972.
14. Hori, Y.; Murata, A.; Kikuchi, K.; Suzuki, S., Electrochemical Reduction of Carbon Dioxides to Carbon Monoxide at a Gold Electrode in Aqueous Potassium Hydrogen Carbonate. Journal of the Chemical Society, Chemical Communications 1987, 728-729.
15. Durst, J., et al., Electrochemical Co2 Reduction – a Critical View on Fundamentals, Materials and Applications. CHIMIA International Journal for Chemistry 2015, 69, 769-776.
16. Herranz, J.; Durst, J.; Fabbri, E.; Patru, A.; Cheng, X.; Permyakova, A. A.; Schmidt, T. J., Interfacial Effects on the Catalysis of the Hydrogen Evolution, Oxygen Evolution and Co2-Reduction Reactions for (Co-)Electrolyzer Development. Nano Energy.

2.3 **Publications / patents**

J. Herranz, J. Durst, E. Fabbri, A. Patru, X. Cheng, A. Permyakova, T.J. Schmidt, Interfacial Effects on the Catalysis of the Hydrogen Evolution, Oxygen Evolution and CO_2-Reduction Reactions for (co-) Electrolyzer Development, *Nano Energy 29 (2016) 4-28*

J. Durst, A. Rudnev, A. Dutta, Y. Fu, J. Herranz, V. Kaliginedi, A. Kuzume, A. Permyakova, Y. Paratcha, P. Broeckmann, T.J. Schmidt, Electrochemical CO_2 Reduction - A Critical View on Fundamentals, Materials and Applications, *Chimia 69 (2015) 769-776*.

Abbott, D. F.; Lebedev, D.; Waltar, K.; Povia, M.; Nachtegaal, M.; Fabbri, E.; Copéret, C.; Schmidt, T. J., Iridium Oxide for the Oxygen Evolution Reaction: Correlation between Particle Size, Morphology, and the Surface Hydroxo Layer from Operando XAS. Chem. Mater. 2016, 28, 6591-6604.

E. Oakton, D. Lebedev, A. Fedorov, F. Krumeich, J. Tillier, O. Sereda, T.J. Schmidt, C. Coperet, A Simple One-Pot Adams Method Route to Conductive High-Surface Area IrO_2-TiO_2 Materials, *New J. Chem. 40 (2016) 1834-1838*

D. Lebedev, M. Povia, K. Waltar, P.M. Abdala, I.E. Castelli, E. Fabbri, M.V. Blanco, A. Fedorov, C. Coperet, N. Marzari, T.J. Schmidt, Highly Active and Stable Iridium Pyrochlores for Oxygen Evolution Reaction, *Chem. Mater. 29 (2017) 5182-5191*

E. Oakton, D. Lebedev, M. Povia, D.F. Abbott, E. Fabbri, A. Fedorov, M. Nachtegaal, C. Coperet, T.J. Schmidt, IrO_2-TiO_2: A High-Surface Area, Active and Stable Electrocatalyst for the Oxygen Evolution Raection, *ACS Catalysis 7 (2017) 2346-2352*

B.J. Kim, D. Abbott, X. Cheng, E. Fabbri, M. Nachtegaal, F. Bozza, I. Castelli, D. Lebedev, R. Schaeublin, C. Copéret, T. Graule, N. Marzari, T.J. Schmidt Unraveling Thermodynamics, Stability, and Oxygen Evolution Activity of Strontium Ruthenium Perovskite Oxide. ACS Catal. 7 (2017) 3245-3256.

Castelli I. E., Mounet N., Prandini G., Marrazzo A. and Marzari N., Verification and reproducibility of quantum-mechanical simulations: the Standard Solid-State Pseudopotential Library, in preparation (2017).

Lejaeghere K. et al., **The Kahn-Sham equation of state for elemental solids: a solved problem,** *Science* 35 (6280), 1415 (2016).

2.5 **Industrial and institutional WP1 partners**

Belenos Clean Power Holding

Swiss Electric Research, Proton OnSite

3. Methanation (WP2)

PSI, Combustion Research Laboratory: ***Tilman Schildhauer, Julia Witte***
PSI, Bioenergy and Catalysis Laboratory: ***Frédéric Vogel***

3.1 General targets and state of WP2 compared to the proposal aims/milestones

a) *Hydrogen addition to hydrothermal gasification/methanation*

Catalytic Hydrothermal Methanation (CHM) of wet biomass is an efficient process developed at PSI during the last fifteen years. The product gas contains ca. 54 vol% CH_4, 40 vol% CO_2, and 5 vol% H_2, as well as ca. 1 vol% of C_{2+}. Its thermal process efficiency "biomass to biomethane" in autothermal operation reaches 60 - 70%, depending on the feedstock composition. The key element of this process is a ruthenium-based catalyst that is able to decompose the larger organic molecules to small fragments and to reform them to the gases CH_4, CO_2, and H_2. Addition of H_2 to the process should shift the product composition towards more methane and less CO_2, as the CHM process is mostly conducted close to the thermodynamic equilibrium, at around 450°C and 28 MPa. Our contribution in this project was (i) to perform process simulations with added H_2, (ii) to validate these simulations by experiments in an existing continuous test rig using a model solution, and (iii) to propose a concept for a process heater for the hydrothermal gasification suited for dual operation on both natural gas and electricity.

All three deliverables/milestones were completed, although somewhat delayed compared to the original research plan. In 2016 we successfully performed an experimental campaign with our test rig KONTI-C, upgraded for the addition of pressurized hydrogen (see section below and Reimer et al., 2017 for details). Simulations of the hydrothermal gasification process with added H_2 were performed with the software package Aspen plus and documented both in Reimer et al., 2017 and in Vogel, 2017. A concept for a dual natural gas/electricity process heater was proposed using commercial components (see section below).

b) *Hydrogen-rich methanation of CO_2-containing gases*

The goal of the activities was to increase know-how on CO2 methanation (converting biogas and pure CO2, e.g. from industrial sources) and hydrogen-rich methanation of gasification derived producer gas by modelling and (dynamic) pilot scale experiments.

The pilot scale set-up "GanyMeth" (that originally was planned to be used for the experimental part) unfortunately was delivered late in 2016; moreover, recent control of the delivered tubing showed severe problems with respect to the welding quality which raises questions for the plant safety. At the moment replacement of all questionable tubing is ongoing. Although the erection of the set-up is funded by another project, the recent issues made it impossible to conduct reactive experiments before end of the project time. Instead, an synergy with another project ("Direct methanation of biogas", DMB) was used. Within the DMB project, the TRL 5 plant Cosyma was connected to a biogas plant in Zürich. After achieving the goals of the DMB project (1000h operation), the operation of the installation was continued to conduct optimisation experiments. These experiments (combined with characterization of catalyst samples) focused especially on the addition of water, which has a significant influence on coke formation and the yield in the main reactor and the effort (CAPEX and OPEX) in the upgrading step of the process.

Further, the efforts were increased to model and optimise in detail the complete process chain of biogas based power-to-gas. For this, the main units (reactors, membranes) were represented by rate-based models, while other process units were calculated with thermodynamic and short-cut models. The detail description of six different process concepts allowed also detailed cost calculations. The results obtained in this thermo-economic analysis can also be applied for the optimization of all other Power-to-Methane process chains.

3.2 **Main Achievements of WP2**

a) *Hydrogen addition to hydrothermal gasification/methanation*

Catalytic Hydrothermal Methanation (CHM) – experimental validation

For this study, we used the existing hydrothermal gasification unit KONTI-C and modified it for hydrogen co-feeding (Fig.). The model solution consisted of a mixture of 10 wt.% glycerol in de-ionized water. The feed mass flow rate was manually adjusted to 1.00 ± 0.02 kg/h and measured online using a Coriolis mass flow meter. The pressure of the test rig was adjusted to 28 or 26 MPa. Hydrogen from a cylinder (Messer Schweiz AG 4.5) was compressed to pressures of ~2-3 MPa above that pressure by a pneumatically controlled compressor (SITEC AG, Switzerland) and injected continuously upstream of the salt separator. The hydrogen flow rate was controlled by a mass flow controller.

The lower part of the catalytic reactor was filled with 713 g of a dry sulfur adsorbing material (Katalco 32-5, Johnson-Matthey; up to ca. 60 cm height), followed by a layer of dry 5 wt.% Ru/C catalyst (BASF; 493 g). Katalco 32-5 was filled in the reactor to adjust the height of the catalyst bed and to be comparable with other experiments having been conducted in the test rig KONTI-C.

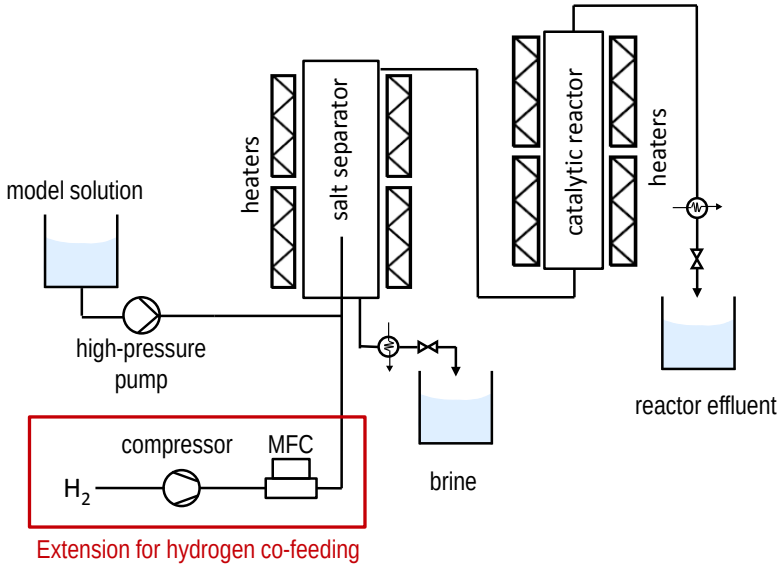

Fig. 3.1 Simplified representation of the hydrothermal gasification test rig KONTI-C including the possibility of hydrogen co-feeding with a mass flow controller (MFC). Some valves, pressure sensors, and thermocouples are omitted for clarity.

We selected seven different operating conditions including two different pressures and three different hydrogen flow rates (Table 3.1). The feed flow rate and the nominal reactor temperature were kept constant. Upon hydrogen addition the temperature profile in the reactor changed drastically (Figure 3.2). An increase of 75 K was measured at the beginning of the catalytic bed, indicating a vigorous reaction involving H_2. The peak temperature decreased along the catalytic bed and reached the same value as without H_2 at the end of the bed.

Table 3.1 Set points for the hydrothermal gasification experiments with 10 wt.% glycerol in water conducted in the test rig KONTI-C (T_SA: Temperature at the outlet of the salt separator, T_R: Temperature along the catalyst bed when operated on pure water; STP: 25 °C, 0.1 MPa)

Exp.	p / MPa	λ (H_2)	$\dot{V}_{STP}$ (H_2) / L/min	$\dot{m}^{H_2} / \dot{m}^{Glycerol}$	T_SA / °C	T_R / °C	$\dot{m}^{Feed}$ / kg/h
A	28	0	0	0	420	400	1.00
BA	28	0	0	0	420	400	1.00
BB	28	0.6	1.2	0.07	420	400	1.00
BC	28	1	2.0	0.11	420	400	1.00
CA	26	0	0	0	420	400	1.00
CB	26	0.6	1.2	0.07	420	400	1.00
CC	26	1	2.0	0.11	420	400	1.00

The gas composition shifted towards more methane and less CO_2, as expected, upon addition of hydrogen (Figure 3.3). The highest methane concentration of 86 vol% was reached when hydrogen was added stoichiometrically (λ = 1) at 28 MPa. Without added hydrogen, the methane concentration was 56 vol%. Decreasing the pressure to 26 MPa had almost no influence on the gas composition (not shown). This measured gas composition at 28 MPa comes close to the composition calculated for equilibrium conditions (see next section). This equilibrium limitation means that a further increase in methane concentration is only possible by reducing the temperature, which is undesired for kinetic reasons. A separation and recycling of the remaining H_2 would be the preferred method.

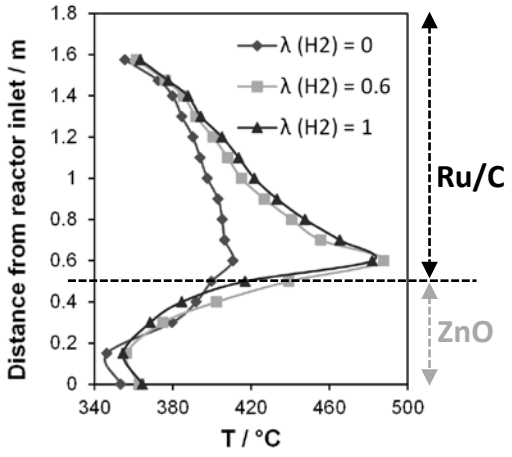

Fig. 3.2 Temperature profiles in the fixed-bed reactor during hydrothermal gasification of 10 wt.% glycerol in water for different hydrogen-to-glycerol ratios (Exp. BA, BB and BC, Tab. 3.1) at a total pressure of 28 MPa. The solid lines are guides to the eye

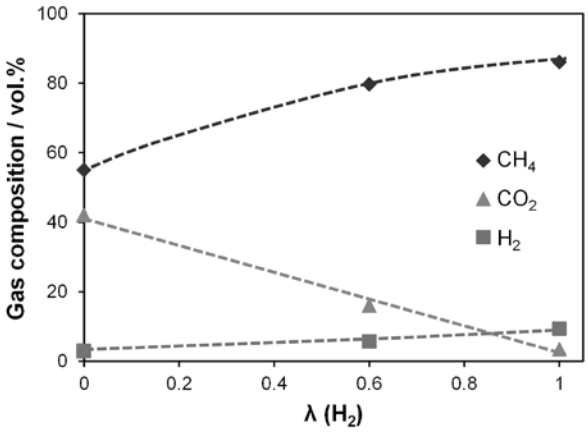

Fig. 3.3 Gas composition during the experiments at 28 MPa pressure (Exp. BA, BB and BC, Tab. 3.1) as a function of the parameter λ which defines the stoichiometric dosage of hydrogen according to Eq. (1). The broken lines are guides to the eye

Full catalytic activity was maintained during and after the hydrogen co-feeding experiments, verified by comparing the performance of a run with a 10 wt.% glycerol in water feed after co-feeding hydrogen, for which the product distribution was very close to the experiments before hydrogen co-feeding (Reimer et al., 2017).

Catalytic Hydrothermal Methanation (CHM) – process simulations

We have set up a flowsheet simulation of our continuous test rig using the software ASPEN plus V 8.0 (Fig. 3.4).

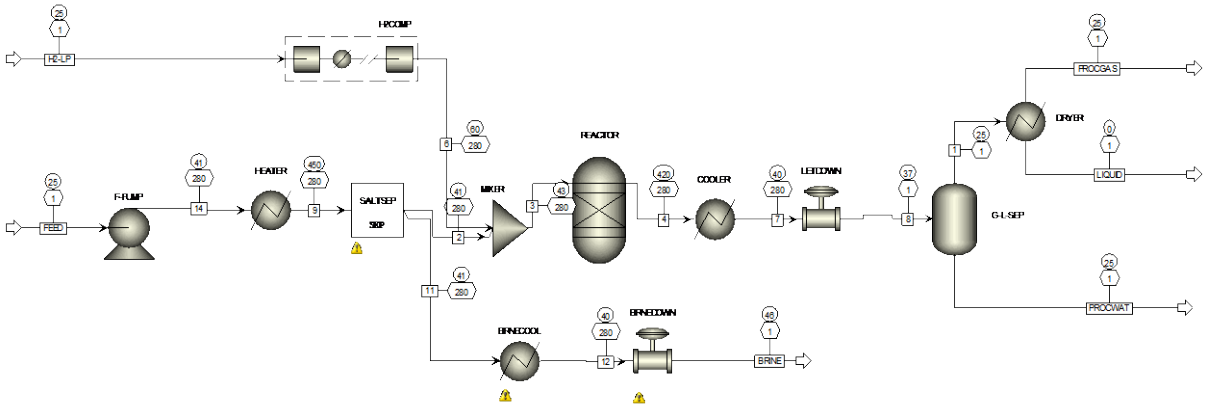

Fig. 3.4 Flowsheet for the simulated CHM process.

A water-glycerol mixture is pumped at 28 MPa and at a flow rate of 1 kg/h, corresponding to the capacity of our test rig "KONTI-C". It is then heated to 450°C and mixed with a hydrogen stream pressurized to 28 MPa. Prior to mixing, salts optionally added to the feed mixture can be removed from the process stream in PSI's patented salt separator. This brine is cooled and depressurized and collected for further use e.g. as fertilizer. The main process stream with the water-glycerol-H_2 mixture is reacted over the catalytic fixed-bed reactor containing the carbon-supported ruthenium catalyst at 420°C and 28 MPa. After cooling and depressurizing the liquid water phase and the gas phase are separated. The gas phase is cooled in a chiller to remove water vapor.

A series of simulations was run as indicated in Table 3.2.

Table 3.2: Process conditions used in the flowsheet simulation of the CHM process.

w_Glyc kg/kg	m*_Feed kg/h	Brine frac kg/kg	V*_H_2 NL/h	λ_H_2 mol/mol	p MPa	T_reac °C
0.2	1	0.15	210	0.86	28	420
0.2	1	0	0	0.00	28	420
0.2	1	0	49	0.20	28	420
0.2	1	0	98	0.40	28	420
0.2	1	0	146	0.60	28	420
0.2	1	0	195	0.80	28	420
0.2	1	0	244	1.00	28	420
0.2	1	0	268	1.10	28	420
0.2	1	0	292	1.20	28	420
0.2	1	0	219	0.90	28	420
0.2	1	0	317	1.30	28	420

The concentration of the glycerol was fixed to 20 wt%, which is a typical value for the CHM process. In the first simulation, a brine stream corresponding to 15% of the total feed stream was withdrawn before the catalytic reactor. In all other simulations, no brine stream was withdrawn. Hydrogen was added in varying amounts to yield the lambda values indicated in Table 3.2. Here, lambda is defined as:

$$\lambda = \frac{\dot{n}_{H2}}{5\,\dot{n}_{glycerol}} \tag{1}$$

This value describes the effective amount of hydrogen fed to the amount needed for stoichiometric conversion of the glycerol to methane and water according to:

$$C_3H_8O_3 + 5\ H_2 = 3\ CH_4 + 3\ H_2O$$

In the flowsheet simulation the equilibrium composition of the process stream leaving the catalytic reactor is then calculated taking the non-ideal behavior of the water-glycerol-H_2/CO_2/CH_4 mixture into account (Peng-Robinson equation of state). The resulting dry gas composition is shown in Fig. 3.5.

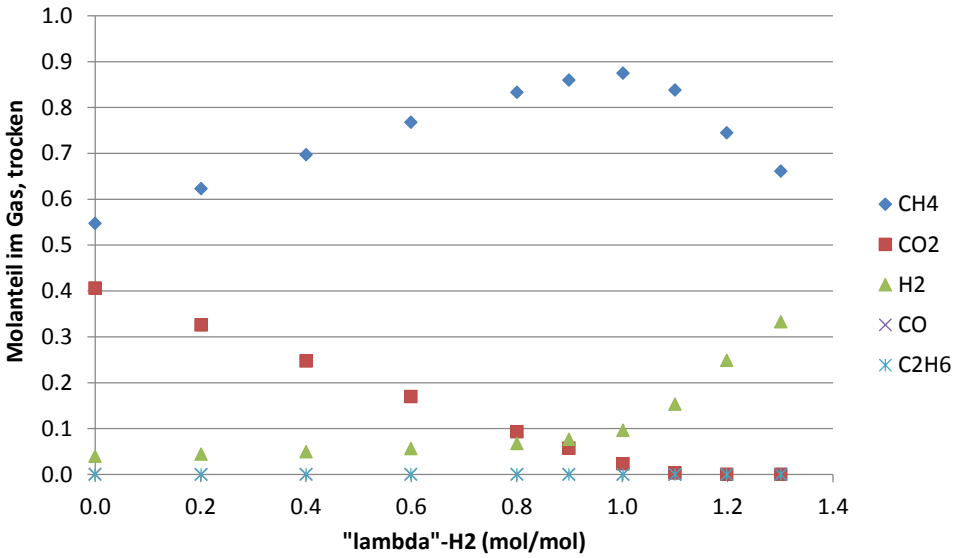

Fig. 3.5 Calculated dry gas compositions for the CHM process with varying amounts of added H_2 at 420°C and 28 MPa.

The gas composition for $\lambda = 0$ corresponds to the "classical" CHM process, i.e. without extra H_2 added. Upon addition of H_2 the methane concentration increases while the CO_2 concentration decreases, and the H_2 concentration remains relatively stable below 10 vol%. At $\lambda = 1$ a maximum in the methane concentration is reached. For higher λ values the CO_2 concentration decreases further but the methane concentration decreases as well, while the hydrogen concentration increases. For $\lambda > 1$ it is thus possible to reduce the CO_2 content to almost zero but at the cost of "diluting" the product gas with the remaining excess H_2. Both carbon monoxide and ethane are not formed at these conditions. The highest methane concentration is thus reached for $\lambda = 1$, but it does not exceed 88 vol% because of the remaining H_2 and CO_2 at these conditions. A higher methane concentration could be reached by operating at lower temperatures, but this would affect the kinetics and thus the space velocity needed to approach the calculated equilibrium composition.

From the simulations a constant value of 15.3 MJ/kg was obtained for compressing the H_2 from ambient pressure to 28 MPa. A two-stage isentropic compression was assumed. For $\lambda(H_2) = 1$ the mass ratio of added H_2 to glycerol was 0.11. Thus ca. 1.7 MJ of external energy need to be supplied per kg of glycerol processed. For other feedstocks the amount of H_2 supplied corresponding to a $\lambda(H_2)$ value of one will vary depending on the H/C and O/C ratio of the feedstock.

Catalytic Hydrothermal Methanation (CHM) – dual source process heater

The overall idea of WP 2 is to integrate as efficiently as possible peak electric power that cannot be used instantly into the methanation or the hydrothermal gasification process. One way to reach this goal is to use the electric power to generate H_2 by electrolysis and to feed the pressurized H_2 into the catalytic processes. This first approach was described in the previous sections. Another approach, proposed here for the hydrothermal gasification (HTG) process only, is to use the electric power to heat the process directly. Since the HTG process must also operate when no peak electric power is available, a gas burner is used as a second energy source. Ideally, one and the same process heater can be operated on both energy sources, minimizing the investment cost. In Fig. 3.6 a schematic layout of such a dual source process heater is shown.

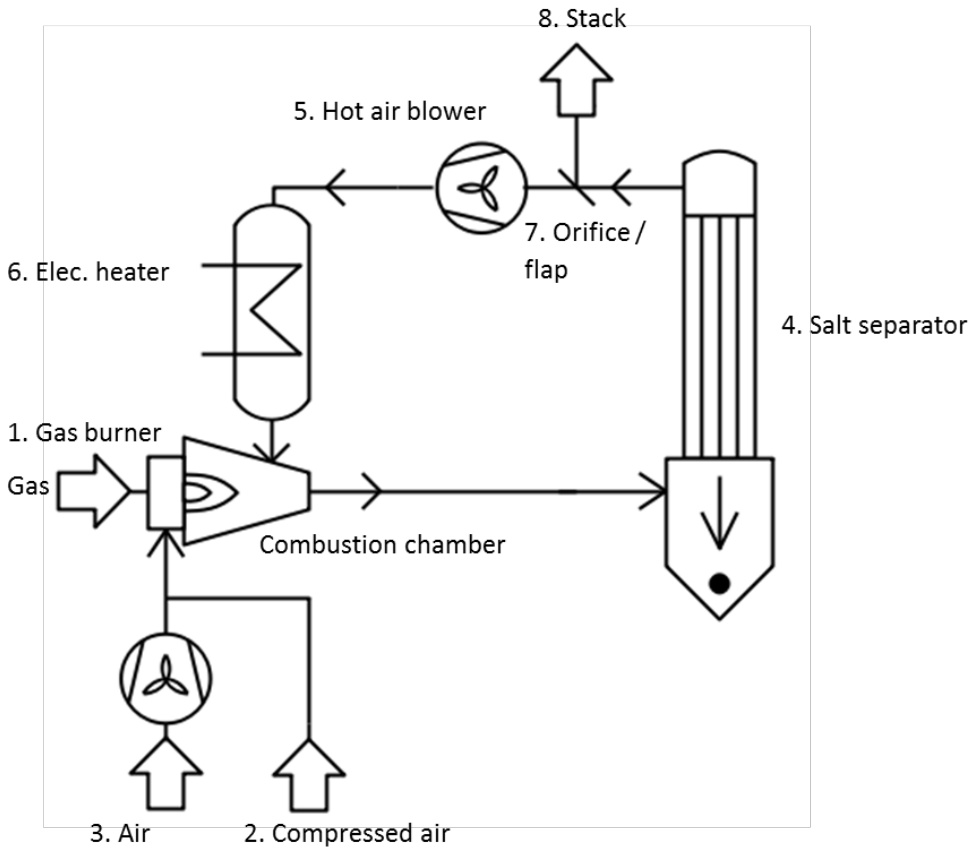

Fig. 3.6 Conceptual design for a dual process heater operated alternatively on a methane-rich gas and electricity. The hot gas circuit is used to heat the fluid inside the high pressure salt separator.

Its operation with a methane-rich gas is as follows:

- Ambient air (3) and gas are mixed and combusted in the burner (1) to produce an exit gas temperature of ca. 700°C.
- The pressure in the hot gas system can be adjusted to max. 0.5 bar using compressed air (2) and/or a hot air blower (5).
- The hot air flows countercurrent to the fluid in the salt separator (4), located inside a high pressure tube bundle.
- Recirculation of the hot air after the salt separator with a temperature of ca. 650°C by the hot air blower via the electric heater (6) into the combustion chamber.
- The gas burner (1) reheats the air to 700°C.
- Some hot air is vented to the atmosphere via a throttle orifice (7) and a stack (8).

Its operation with electric power is as follows:

- Cold air (2 or 3) is routed to the electric heater (6) via the gas burner (1), the salt separator (4) and the hot air blower (5).
- The pressure in the hot gas system can be adjusted to max. 0.5 bar using compressed air (2) and/or the hot air blower (5).
- The fresh air supply (2 or 3) is adjusted, as the hot air blower recirculates the air stream through the system.
- The electric heater (6) increases the temperature of the hot air up to the desired value.
- Some hot air is vented to the atmosphere via a throttle orifice (7) and a stack (8).

Such a system could be switched fast from gas to electric operation and back again. It can use both low and high calorific gases and reaches a high efficiency due to the recirculation loop. When available, air preheated to max. 250°C could be used, further increasing the overall efficiency by reducing the consumption of gas or electricity. Gas burners are commonly used in industrial heating. Electric heating of gases to high temperatures is less common. Fig. 3.7 shows a commercial system that could be used for the HTG process.

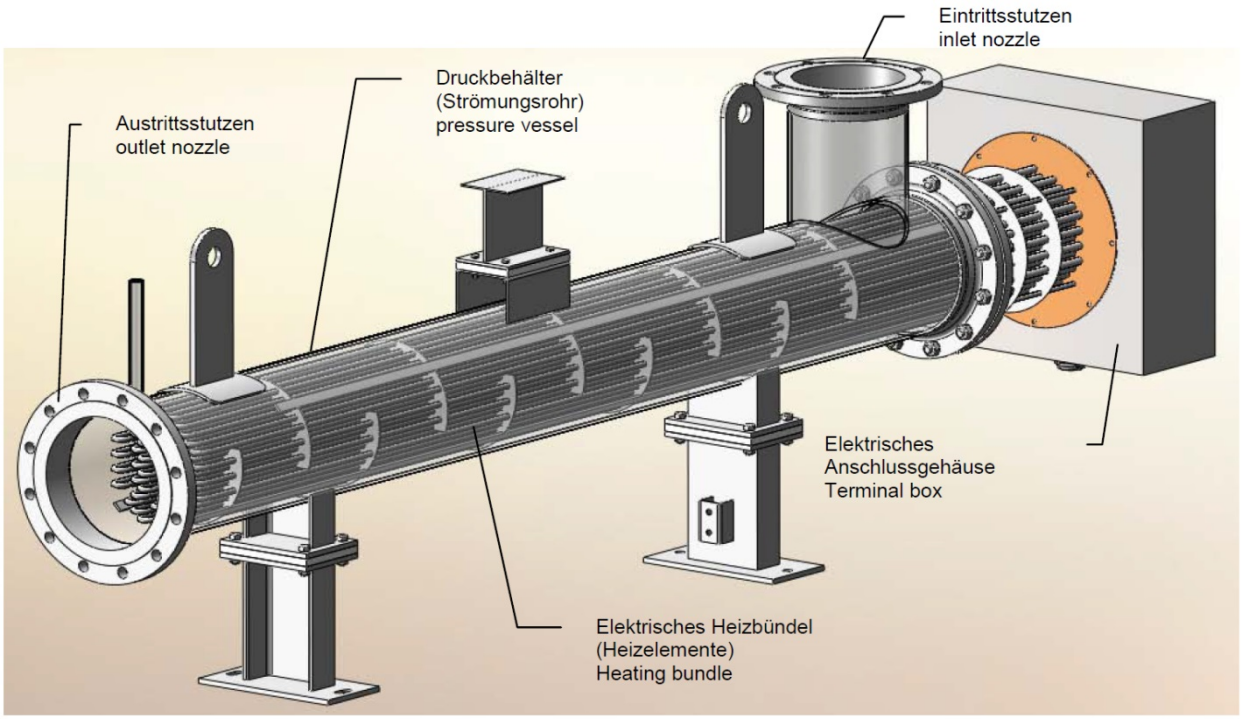

Fig. 3.7 Electric air heater Typ STR (OhmEx GmbH, Germany).

b) *Hydrogen-rich methanation of CO_2-containing gases*

Process modelling

In the modelling of CO_2-methnation processes, different processes were considered in the investigation of biogas upgrading. For this, the main units (reactors, membranes) were represented by rate-based models, while other process units were calculated with thermodynamic and short-cut models. The detail description of four different process concepts allowed also detailed cost calculations. Not only the fluidised bed technology was investigated, but also fixed bed technology in order to convert carbon dioxide into methane. As a result, four considered processes are listed in Table 3.3.

Table 3.3: Overview of the process models for biogas upgrading

Model description	Abbreviation
Biogas upgrade via bubbling fluidised bed (BFB) and fixed bed (FB)	BFB-FB
Biogas upgrade via two-stage FB technology	FB-FB
Biogas upgrade via BFB and H_2-membrane	BFB-Mem
Biogas upgrade via FB and H_2-membrane	FB-Mem

The corresponding flowsheets of the models are illustrated in Figures 3.8 and Figure 3.9. The procedure allows the direct comparison of fixed bed and fluidised bed technology. The approach of the process evaluation was as follows: First an optimisation of the operational conditions via difference-in-cost method was applied. This means that the changing costs due to a specific combination of operation conditions (and according reactor designs) were compared to a base case. Secondly, a detailed economic analysis of the optimised process was conducted, which allowed the comparison with the other optimised processes.

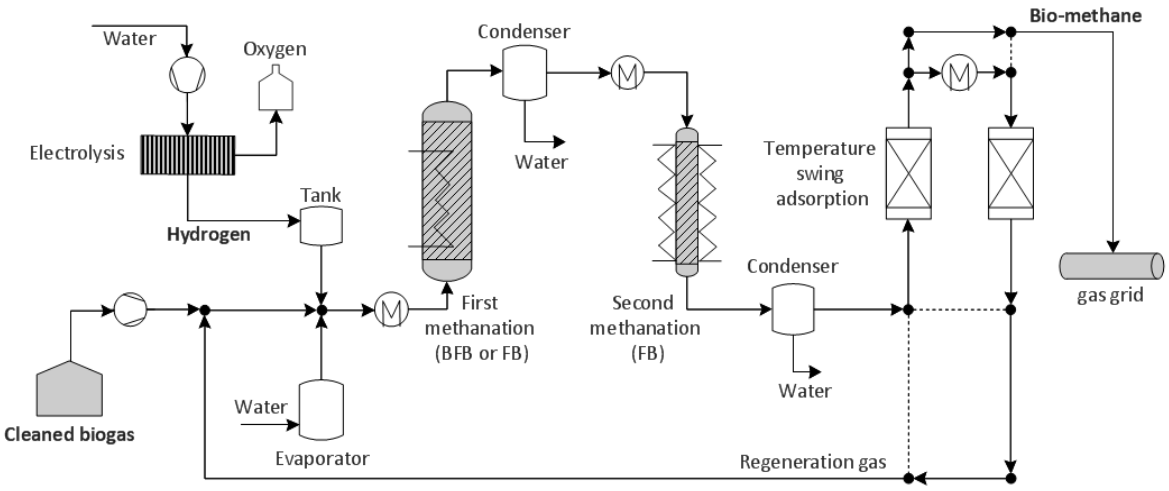

Fig. 3.8 Flowsheet of the upgrade process of biogas via two-stage methanation according to the models BFB-FB and FB-FB

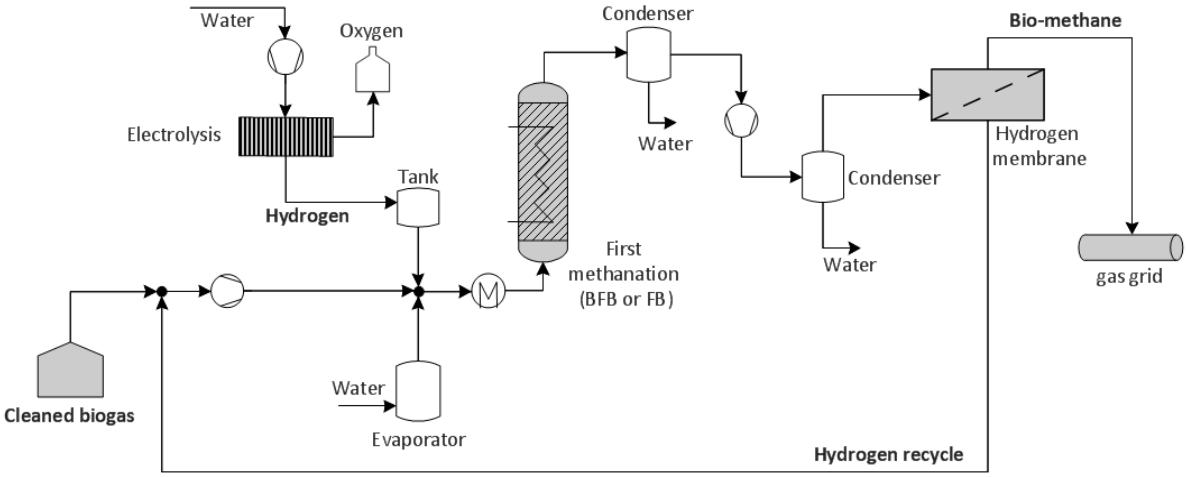

Fig. 3.9 Flowsheet of the upgrade process of biogas via methanation and hydrogen separation with a membrane according to the models BFB-Mem and FB-Mem

Reactor models

Isothermal bubbling fluidised bed reactor. The internally cooled fluidised bed reactor is modelled according to the pseudo-homogeneous two phase approach of Kopyscinski et al. [18] where hydrodynamic correlations for freely bubbling fluidized beds are applied.

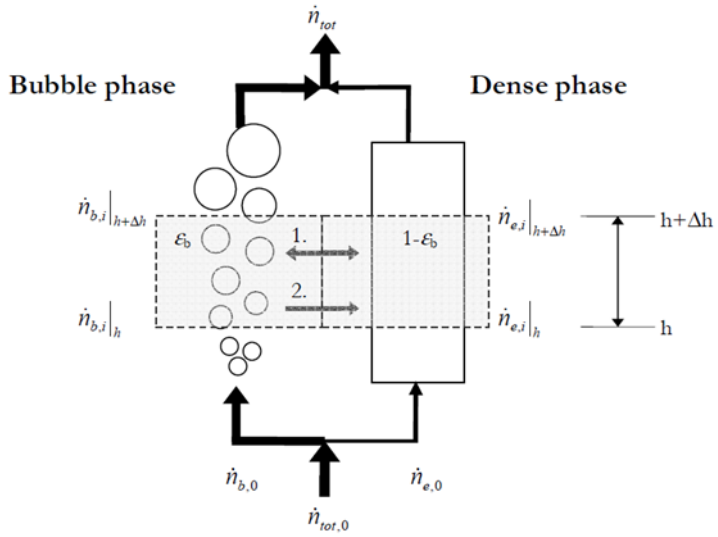

Fig. 3.10 Two phase model used for the bubbling fluidised bed model

According to 3.10, the total inlet gas flow $\dot{n}_{tot,0}$ is divided into the bubble $\dot{n}_{b,0}$ and the dense phase $\dot{n}_{e,0}$ gas flow, corresponding to the volumetric fraction of the bubble phase ε_b and of the dense phase $\varepsilon_e = 1 - \varepsilon_b$. The volumetric fraction of the bubble phase is determined by the following equation from Hilligart et al. [19] via superficial velocities u and bubble diameters d_b derived from bubble size correlations :

$$u_b = \psi\left(u - u_{mf}\right) + 0.711\, v\sqrt{g\, d_b} \tag{3}$$

$$\varepsilon_b = \frac{\psi\left(u - u_{mf}\right)}{u_b} \tag{4}$$

The parameters ψ and υ consider the different types of Geldart particles and depend on reactor height and diameter. The molar balances for the bubble and dense phase are shown in Equation (5) and (6), respectively.

$$0 = -\frac{d\dot{n}_{b,i}}{dh} - K_{G,i} \cdot a \cdot A_{cross} \cdot \left(c_{b,i} - c_{e,i}\right) - \dot{N}_{vc} \cdot x_{b,i} \tag{5}$$

$$0 = -\frac{d\dot{n}_{e,i}}{dh} + K_{G,i} \cdot a \cdot A_{cross} \cdot \left(c_{b,i} - c_{e,i}\right) + \dot{N}_{vc} \cdot x_{b,i} + \left(1-\varepsilon_b\right) \cdot \left(1-\varepsilon_{mf}\right) \cdot \rho_P \cdot A_{cross} \cdot R_i \tag{6}$$

Here, $\left(1-\varepsilon_b\right)$ represents the volume fraction of the dense phase, $\left(1-\varepsilon_{mf}\right)$ express the volume fraction of the particles assuming minimal fluidisation conditions in the dense phase and $\mathrm{R_i} = \sum \nu_{\mathrm{im}} \mathrm{r_m}$ describes the overall reaction, where m represents the WGS and methanation reactions.

Between the two phases, mass transfer occurs due to concentration differences but also due to the mole reducing reaction. The interphase mass transfer is described as the sum of the two phenomena, see Equation (7).

$$\dot{N}_{vc} = \frac{\dot{n}_{vc}}{dh} = \sum_i K_{G,i} \cdot a \cdot A \cdot \left(c_{b,i} - c_{e,i}\right) + \left(1-\varepsilon_b\right) \cdot \left(1-\varepsilon_{mf}\right) \cdot \rho_P \cdot A \cdot \sum_i R_i \tag{7}$$

The following assumptions for the differential equations were made: steady state conditions and ideal gas behaviour are assumed with no reaction in the bubble phase. Laminar boundary layers around the catalyst particles as well as pore diffusion are neglected; hence gas concentrations in the dense phase and on the catalyst particles are equal. Radial gas concentrations differences are neglected. Two main aspects influence the performance of the reactor: the reaction kinetics and the hydrodynamics caused by the bubbles inside of the reactor. For the kinetics, a Langmuir-Hinshelwood approach was implemented with rate equations for the water gas shift reaction:

$$r_{WGS}^{BFB} = \frac{k_{WGS}\left(K_\alpha p_{CO} p_{H_2O} - \left(\frac{p_{CO_2} p_{H_2}}{K_{eq,WGS}}\right)\right)}{p_{H_2}^{0.5}\left(1+K_C p_{CO}^d \, p_{H_2}^e + K_{OH} \, p_{H_2O} \, p_{H_2}^{-0.5}\right)^2} \tag{8}$$

and for the methanation reaction:

$$r_{Meth}^{BFB} = \frac{k_{Meth} K_C \, p_{CO}^a \, p_{H_2}^b \left(1 - \left(\frac{p_{CH_4} p_{H_2O}}{K_{eq,meth} \, p_{CO} \, p_{H_2}^3}\right)\right)^c}{\left(1+K_C p_{CO}^d p_{H_2}^e + K_{OH} p_{H_2O} p_{H_2}^{-0.5}\right)^2} \tag{9}$$

Rate and adsorption constants are based on the Arrhenius and Van't Hoff approach:

$$k_i = k_{i,T_{ref}} \exp\left(\frac{E_{A,i}}{RT_{ref}}\left(1 - \frac{T_{ref}}{T}\right)\right) \quad , i = WGS, Meth \tag{10}$$

$$K_j = K_{j,T_{ref}} \exp\left(\frac{\Delta H_j}{RT_{ref}}\left(1 - \frac{T_{ref}}{T}\right)\right) \quad , j = \alpha, C, OH \ldots \tag{11}$$

The values of the kinetic parameters are given in 3.4 [11].

Table 3.4: Kinetic and adsorption constants of the methanation and water-gas-shift rate expressions for the bubbling fluidized bed methanation [11].

Parameter	Unit	Value
$k_{WGS,ref}^{BFB}$	-	8.40
$k_{Meth,ref}^{BFB}$	-	1.08
$E_{A,WGS}^{BFB}$	kJ/mol	155.7
$E_{A,Meth}^{BFB}$	kJ/mol	63.1
$K_{\alpha,ref}$	bar^{-2}	0.36
$K_{C,ref}$	$bar^{-1.5}$	2.53
$K_{OH,ref}$	$bar^{-0.5}$	0.67
ΔH_{α}	kJ/mol	-1.7
ΔH_{C}	kJ/mol	-50.7
ΔH_{OH}	kJ/mol	-87.5
a	-	0.5
b	-	1
c	-	1
d	-	0.5
e	-	0.5
T_{ref}	K	598.15

The hydrodynamics of the reactor are expressed through bubble size correlations, with which bubble rise velocities and the bubble holdup ε_b are determined in a next step. This procedure allows the determination of the total surface area of the bubbles and then the interphase mass transport from the bubble into the dense phase. Then, the kinetic expressions are applied, which result in new molar flows of the components due to the reactions in the dense phase at a specific reactor height.

Different bubble size correlations for fluidised beds exist in the literature [20] - [21], but only at non-reactive conditions and without heat exchanger internals. Another study has shown that bubble growth is inhibited by the presence of internals [22], therefore the bubble size correlation with the smallest overall bubble size was chosen, as given by Werther [20]:

$$d_B = 0.835\left(1 + 0.272\,(u - u_{mf})\right)^{1/3}(1 + 0.0684\,h)^{1.21} \tag{12}$$

Since the bubble diameter influences the gas composition in the dense phase via the mass transfer area and therefore the reaction performance, a precise correlation is essential for the accuracy of the model.

Fixed bed reactor. The fixed bed (FB) methanation model is also based on kinetic expressions and considers the same chemical equations (1) and (2) as the bubbling fluidized bed (BFB) model. The shell-side cooled reactor includes internal tubes with an inner diameter of 2.5cm each, which contain the catalyst. The description of the applied pseudo-homogeneous first order model can be found from [12]. Steady state conditions and ideal gas behaviour are assumed again with no radial concentration changes.

The applied axial molar balance and the energy balance for the fixed bed reactor are given by:

$$\frac{d\dot{n}_i}{dz} = \sum_m \nu_{im} r_m \cdot A_{cross} \cdot \rho_{cat} \tag{13}$$

$$G \cdot c_p \cdot \frac{dT}{dz} = \sum_j r_j \cdot \Delta H_{\mathrm{Re}ac,m} \cdot \rho_{cat} + \frac{4 \cdot U}{d_{tube}} \cdot \left(T_{wall} - T\right) \tag{14}$$

The overall thermal transmittance U is calculated at each step based on the actual gas composition according to the correlation for a particle bed for spherical particles of 1.8 mm diameter [23]:

$$\mathrm{Nu} = 0.223 \cdot \mathrm{Rep}\ 0.6109 \cdot \mathrm{Pr}\ 0.333 \tag{15}$$

And the corresponding expressions for the Nusselt, Reynolds and Prandtl numbers:

$$Nu = \frac{\alpha_{\mathrm{int}ernal} \cdot d_p}{\lambda_{Fluid}} \tag{16}$$

$$\mathrm{Pr} = \frac{c_p \cdot \eta}{\lambda_{Fluid}} \tag{17}$$

$$\mathrm{Re}_p = \frac{G \cdot d_p}{\eta} \tag{18}$$

The main thermal resistance is assumed to be in the internal gas phase between the catalyst particle and the inner reactor wall, hence the thermal transmittance is expressed through $\frac{1}{\mathrm{U}} = \frac{1}{\alpha_{\mathrm{internal}}}$, where the thermal resistance in the wall and outside the tube is neglected.

Two different sets of kinetic parameters were applied. For the main fixed bed reactor, kinetic data were taken from [12]. The catalyst described is thermally stable at high temperatures, but is less active at lower temperatures. The kinetics for the methanation reaction in Equation (14) are originally retrieved from the perspective of steam reforming [13], where the methanation reaction from CO to methane was defined as reversed reaction. Hence, the parameter $\mathrm{K_{Meth}}$ in equation (14) represents the equilibrium constant of steam reforming.

$$\mathrm{r}_{\mathrm{WGS}}^{\mathrm{FB}} = \frac{\mathrm{k_{WGS}}\left(\mathrm{p_{CO}p_{H_2O}} - \mathrm{p_{CO_2}p_{H_2}}/\mathrm{K_{WGS}}\right)}{\mathrm{p_{H_2}}\left(1+\mathrm{K_{CO}p_{CO}}+\mathrm{K_{H_2}p_{H_2}}+\mathrm{K_{CH_4}p_{CH_4}}+\mathrm{K_{H_2O}p_{H_2O}p_{H_2}^{-1}}\right)^2} \tag{19}$$

$$\mathrm{r}_{\mathrm{Meth}}^{\mathrm{FB}} = \frac{\mathrm{k_{Meth}}\left(\mathrm{p_{CO}p_{H_2}^3}/\mathrm{K_{Meth}} - \mathrm{p_{CH_4}p_{H_2O}}\right)}{\mathrm{p_{H_2}^{2.5}}\left(1+\mathrm{K_{CO}p_{CO}}+\mathrm{K_{H_2}p_{H_2}}+\mathrm{K_{CH_4}p_{CH_4}}+\mathrm{K_{H_2O}p_{H_2O}p_{H_2}^{-1}}\right)^2} \tag{20}$$

Rate and adsorption constants are determined analogously by the Arrhenius and Van't Hoff approach.

For the second stage fixed bed model, the same kinetic parameters as for the bubbling fluidised bed are applied (see Table 3.4). In comparison to the main reactor, the kinetic values applied here describe a more thermodynamically beneficial catalyst, because it is more active at lower temperatures. But the thermal stability is not as high as for the first catalyst bed. However, in the second stage fixed bed only medium temperatures are reached, because the reaction extent and therefore the reaction heat produced are low due to the small amount of remaining carbon dioxide in the inlet gas to the second stage reactor.

Membrane Model

For the membrane unit, a detailed model was implemented. Figure 3.11 shows a scheme of a membrane module with one fibre in co-current flow. The feed enters the module and flows outside along the fibre. Over the length of the module, gas components are permeating through the membrane wall into the fibre.

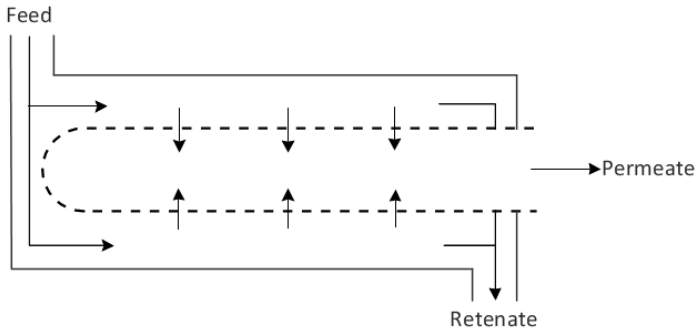

Fig. 3.11 Simplified Scheme of a hollow-fibre module of a membrane

Ideal gas behavior and no pressure drop inside the fibre are assumed. The local permeation of gas through a non-porous membrane can be described by Fick's law [1]. It is assumed that the permeability of a pure component is not changing in a mixture or with varying pressure.

The model was implemented within a Matlab routine and executed inside a Matlab script, which describes the whole process. Values for the permeability constant are taken from [2] and [3]. The new model was compared with a short cut model, which is based on the expression of the selectivity for big pressure differences inside the membrane module [4]:

The result of the comparison between rigorous and short cut model is shown in Figure 3.12 and Figure 3.13, where the permeate flow and the retentate flow is illustrated over the membrane area for the different models. The pressure difference between permeate and retentate side was set to 27 bar. Permeability constants were chosen from [2].

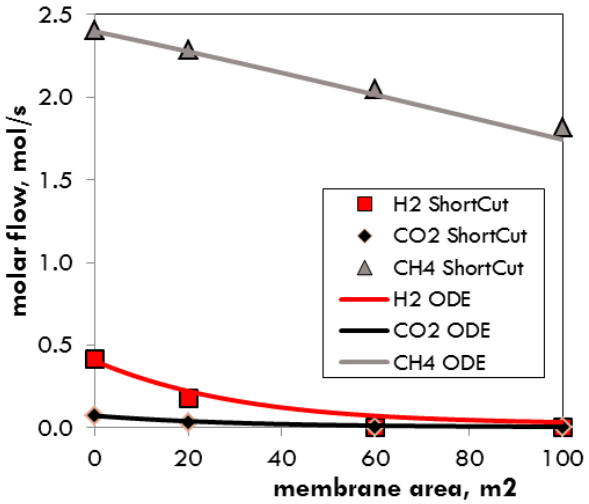

Fig. 3.11 Course of the molar flow of hydrogen, carbon dioxide and methane in the retentate over the membrane area for the short cut and the rigorous (ODE) model at a pressure difference of 27 bar

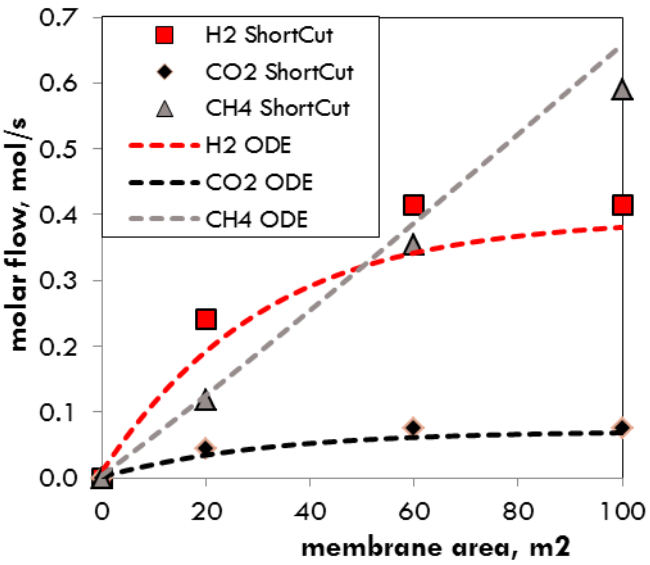

Fig. 3.12 Course of the molar flow of hydrogen, carbon dioxide and methane in the Permeate over the membrane area for the short cut and the rigorous (ODE) model at a pressure difference of 27 bar

It is apparent, that for big pressure differences between permeate and retentate side, the short cut model shows similar results in comparison to the rigorous model. However, small differences in the membrane model result in significant changes for the whole process. The aim of the membrane module is to lower the hydrogen amount in the retentate under 2 mole-%. The short cut model reaches this goal after 60m^2 of membrane area. The decline of hydrogen in the retentate calculated of the rigorous model is slightly weaker, but results in a significant higher membrane area needed for the separation target, which requires an area of 92 m^2.

If a bigger area is needed, it can be seen in Figure 3.12, that the permeate flow becomes more impure. The amount of methane and carbon dioxide in the permeate is increasing. For the whole process, this behavior

results in a bigger recycle stream, which requires more compression power and causes higher electricity consumption. Because the rigorous model represents the real membrane behaviour better than the short cut model, the rigorous model should be used for the evaluation of the four processes mentioned above.

Results

With the improved membrane model, the four complete process chains were calculated in detail. Figure 3.13 shows as example the Sankey diagram (energy and mass flows) of one process concept. Due to optimization with continuous cost and efficiency functions for each process unit, pressures are chosen relative high, because this minimizes reactor dimensions. This procedure does not take into account technology jumps (e.g. choice of a different compressor type with different specific costs at a certain pressure difference), such that a pragmatic optimization considering more realistic technical options and commercially available units which finally may lead to slight deviating results.

While the four options lead to similar heat production and all are able to deliver injectable gas, the fluidized bed options lead to significantly lower reactor size (i.e. catalyst hold-up) and therefore costs.

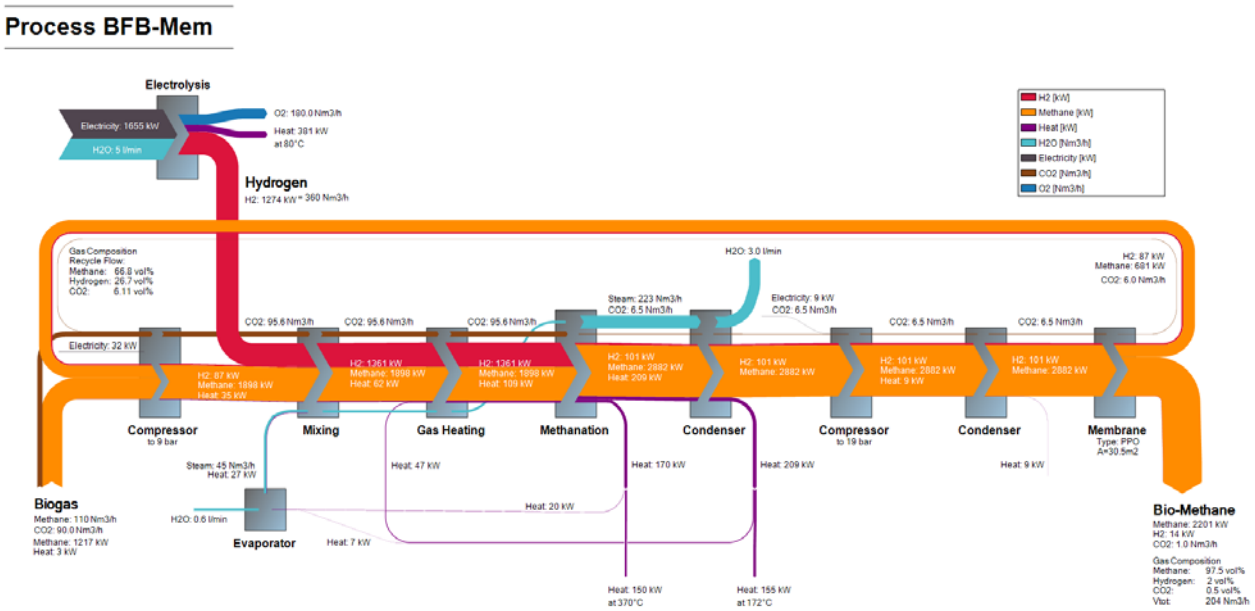

Fig. 3.13 Sankey diagram of modelled process chain

Table 3.5 Operational conditions and properties of optimal case for each process

	BFB-FB	FB-FB	BFB-Mem	FB-Mem
$P_{reactor}$ [bar]	12	14	12	25
p_{Mem} [bar]	-	-	28	28
$H_2/CO_{2,\ input}$	4.03	4.03	4.0	4.0
Membrane type	-	-	PPO	PPO
$T_{1.\ reactor}$ [°C]	375	354	380	373
$\dot{Q}_{excess}$ [kW]	241	223	249	245
$m_{Cat,tot}$ [kg]	88	211	67	193
$\dot{Q}_{el,tot}$ [kW]	1682	1695	1699	1702
Biomethane composition [mol%]:				
H_2	1.97	1.94	1.94	1.94
CO_2	0.16	0.15	0.44	0.48
CH_4	97.86	97.90	97.54	97.55

Experimental

A long-duration experiment was conducted within the project "Direct methanation of biogas". For this, the set-up COSYMA including a bubbling fluidised bed reactor was transported to the biogas plant in Zurich-Werdhölzli. The chosen operation conditions for the long duration experiment were chosen based on simulations conducted within the RENERG^2 project. After achieving the goals of the DMB project (1000h operation), the operation of the installation was continued to conduct optimisation experiments. These experiments (combined with characterization of catalyst samples) focused especially on the addition of water, which has a significant influence on coke formation and the yield in the main reactor and the effort (CAPEX and OPEX) in the upgrading step of the process. Especially the tendency for coke formation could be tested within this set-up, because chemistry-related phenomena are more or less scale-independent.

Compared to the operation conditions during the long duration experiment, water/steam addition was first reduced by half for 45 h, and then stopped completely. This way the catalyst surface area is only covered by the biogas species and the water produced during the methanation reaction.

Figures 3.14 shows the molar fractions of the reaction product methane and the reactants CO^2 and hydrogen. During the first 1000h, activity slightly dropped, mainly due to slow catalyst poisoning by Sulphur breakthrough. After 1000h, the yield and in consequence the methane molar fraction increases again due to the lower addition of steam. A positive effect on the yield was expected because water competes with hydrogen in adsorbing on the catalyst surface, on the one hand, and it changes the thermodynamic equilibrium limitation to lower values, on the other hand.

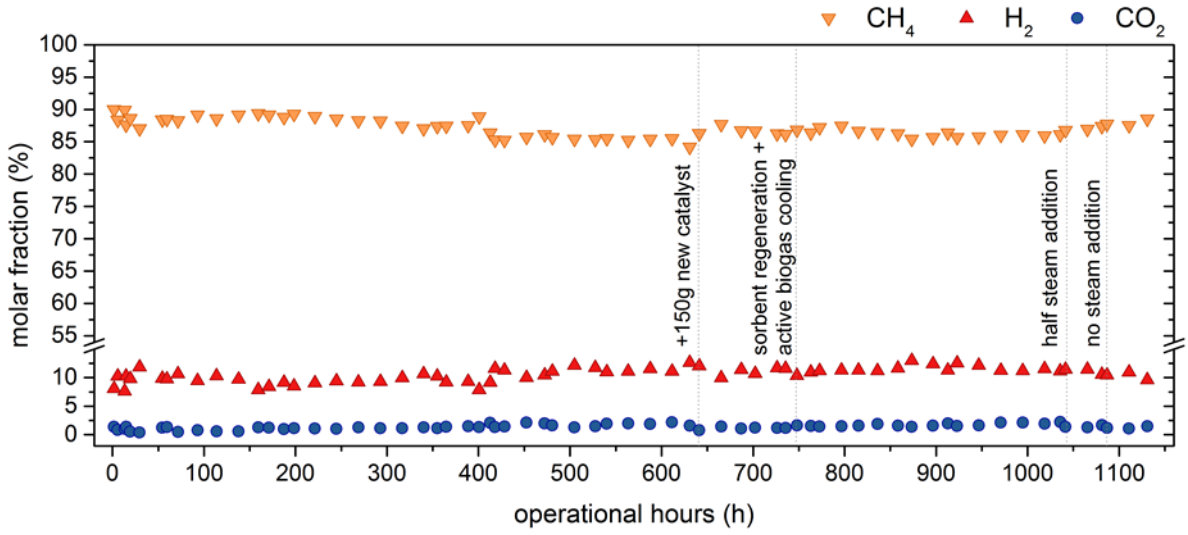

Fig. 3.14 Fractions of methane, hydrogen and CO2 during the field test of COSYMA using real biogas at the biogasplant Zurich. Attention should be focused on the experimental results after 1000 where optimization of the water addition was conducted for the RENERG^2 project.

Lower steam addition, however bears the risk of carbon deposition due to the high amounts of carbon in the system. This was investigated by taking catalyst samples from the reactor (cooled material under nitrogen flow) and subsequent temperature programmed oxidation (TPO). During this analysis, carbon in the catalyst sample will burn and form CO_2 which is detetcted by e.g. a FTIR or a MS. Due to their different chemical stability of the carbon species, the temperature at which a carbon species burns varies. In Figure 3.15, the CO_2 evolution at 800°C (after 150 min) refers to graphite which is a component of the catalyst material and therefore visible even in the fresh material.

The CO_2 peaks rising at temperature between 150°C and 500°C are very typical for polymeric carbon deposition o the catalyst surface. While this peak is very strong for the catalyst samples from experiments with gasification derived producer gas (samples Cosyma 5 and 16), it is very weak for the samples from the biogas upgrading experiments. It can therefore be concluded that lowering the steam addition seems not to compromise the catalyst and process stability.

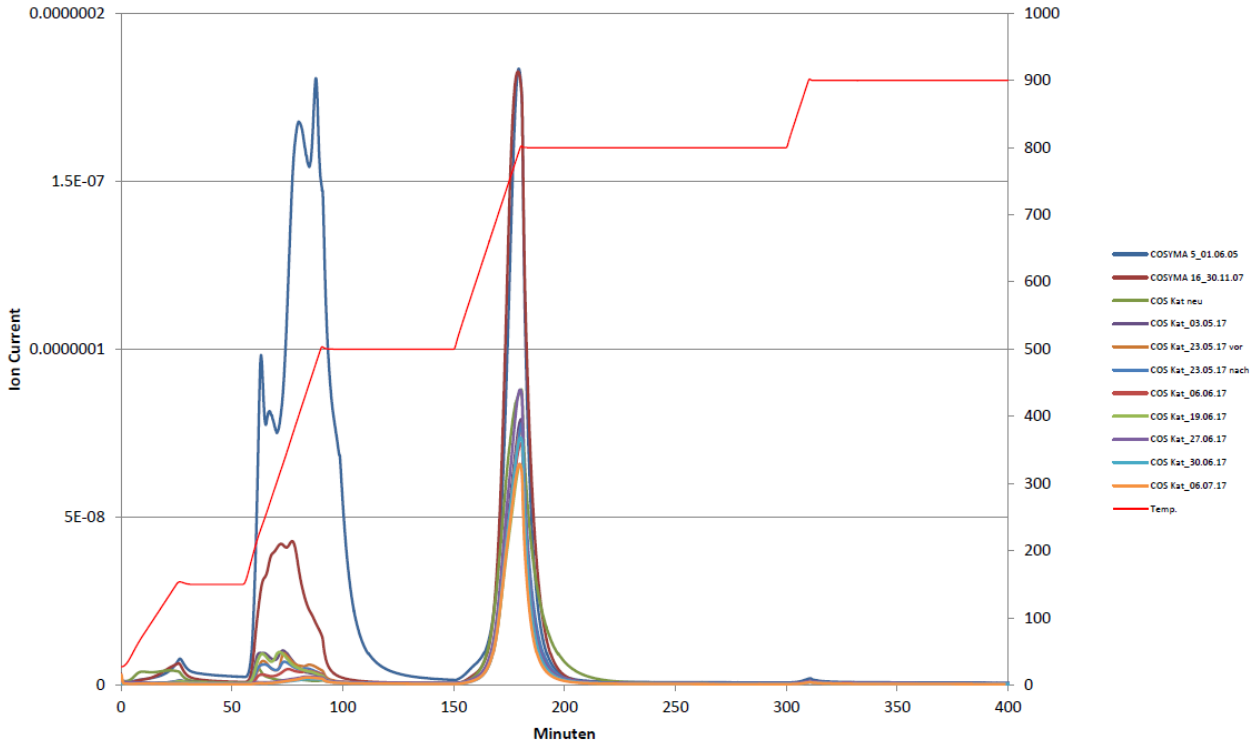

Fig. 3.15 Temperature programmed oxidation (TPO) of different catalyst samples from actual and previous (Cosyma 5, 16) experiments.

References

[11] S. L. Teske, "Integrating Rate Based Models into a Multi-Objective Process Design & Optimisation Framework using Surrogate Models," vol. 6302, 2014.

[12] N. R. Parlikkad et al., "Modeling of fixed bed methanation reactor for syngas production: Operating window and performance characteristics," Fuel, vol. 107, pp. 254–260, 2013.

[13] J. Xu and G. F. Froment, "Methane Steam Reforming , Methanation and Water-Gas Shift : 1 . Intrinsic Kinetics," AIChE J., vol. 35, no. 1, pp. 88–96, 1989.

[17] Evonik, "Factsheet - SEPURAN® Noble - Membrantechnologie für Helium- und Wasserstoffaufbereitung," 2016.

[18] J. Kopyscinski, T. J. Schildhauer, and S. M. A. Biollaz, "Methanation in a fluidized bed reactor with high initial CO partial pressure: Part II- Modeling and sensitivity study," Chem. Eng. Sci., vol. 66, no. 8, pp. 1612–1621, 2011.

[19] K. Hilligardt and J. Werther, "Lokaler Blasengasholdup und Expansionsverhalten von Gas/Feststoff-Wirbelschichten," Chem. Eng. Technol., vol. 57, no. 7, 1985.

[20] J. Werther, "Die Bedeutung der Blasenkoaleszenz fur die Auslegung von GaslFeststoff-Wirbelschichten," Chemie Engenieur Tech., vol. 48, no. 4, p. 339, 1976.

[21] S. Mori and C. Y. Wen, "Estimation of bubble diameter in gaseous fluidized beds," AIChE J., vol. 21, no. 1, pp. 109–115, 1975.

[22] S. Maurer et al., "Correlating bubble size and velocity distribution in bubbling fluidized bed based on X-ray tomography," Chem. Eng. J., vol. 298, pp. 17–25, 2016.

3.3 Publications / patents

Reimer, J.; Müller, S.; De Boni, E.; Vogel, F. Hydrogen-enhanced catalytic hydrothermal gasification of biomass, *Biomass Conversion and Biorefinery*, published online, DOI 10.1007/s13399-017-0253-y.

Vogel, F. *Simulation of the addition of compressed H_2 to the hydrothermal gasification process*, internal report, Bioenergy and Catalysis Laboratory, Paul Scherrer Institut, Villigen PSI, September 6, 2017.

Witte J., Settino J., Biollaz S.M.A., Schildhauer T.J., *Direct Catalytic Methanation of Biogas – Part I: New Insights into Biomethane Production using Rate-Based Modelling and Detailed Process Analysis*, manuscript submitted

3.5 Industrial and institutional WP2 partners

The knowhow gained within the RENERG^2 project was used to start a collaboration with energie360°, Zürich, which finally lead to the long duration test with Cosyma at the biogas plant Zurich which was then financed within a different project.

4. Combustion Fundamentals (WP3)

ETH, Aerothermochemistry and Combustions Laboratory: ***Yuri Wright, Jann Koch***
Empa, Internal Combustion Engines: ***Wolfgang Kreutner, Thomas Kammermann***

4.1 General targets and state of WP3 compared to the proposal aims/milestones

The aim of this WP is the development of a 3-D CFD framework for hydrogen enriched methane combustion suitable for a wide range of operating conditions in the LES context, focusing on a turbulent flame speed closure. The model is to be validated by means of generic data from WP 3.2 and subsequently applied to the full metal engine of WP 4.

The objectives in the experimental part is the understanding of ignition and early flame formation of hydrogen enriched methane/air admixtures by means of optical measurement techniques. By modifying the RCEM for turbulent premixed combustion, detailed datasets of the ignition event, turbulent flow field and early flame kernel growth are required for validation of LES-CFD calculations. A spectroscopic measurement technique to characterize individual ignition events shall be developed and applied to engine experiments.

An optically accessible ignition cell to investigate Spark-Induced Breakdown Spectroscopy (SIBS) was successfully designed, commissioned and used throughout this project. The hydrogen mass fraction in the admixture of hydrogen methane and air was determined effectively by means of atomic hydrogen and swan band emissions. An air-fuel ratio quantification based on SIBS was successfully completed for methane-air mixtures based on hydrogen and nitrogen/oxygen emission lines. A calibration curve was derived at 10 bar ignition pressure, representative for the in-cylinder pressure in the Rapid Compression Expansion Machine (RCEM) at spark timing.

Turbulent flow conditions in the RCEM were achieved by means of an under-expanded gas injection at the beginning of the compression stroke. Temporally resolved Particle Image Velocimetry (PIV) confirmed the achievement of engine relevant turbulence levels at spark timing in the optically accessible region in the vicinity of the spark plug. 3D-CFD simulations were performed and agreed well with the measurements. The additional information on the evolving three-dimensional flow field within the entire domain obtained therewith provided further understanding of the in-cylinder processes. Reactive experiments under laminar and turbulent conditions have been performed, and the impact of hydrogen content in the methane/air admixture on ignition and the early flame kernel formation and subsequent evolution of the flame characterized.

A database for a wide range in pressure, unburned temperature, hydrogen fraction, air-to-fuel ratio and Exhaust Gas Recirculation (EGR) for 1-dimensional unstrained laminar flames has been created. Based on a detailed chemical mechanism, characteristic parameters such as the laminar flame speed and thermal thickness as well as the species profiles have been stored. This data is used as a sound basis for the modeling of the turbulent flame speed in 3D-CFD.

A LES framework has been developed which is capable of reproducing the experimentally observed cycle-to-cycle variations (CCV) in terms of the pressure trace in the full-metal engine under consideration. The numerical data further allowed for identification of correlations as well as the origins of the CCV. Subsequently, different turbulent flame speed closures were been implemented and compared to a commonly used model.

Based on the PIV measurements in the RCEM and a numerical characterization of the flow field in the 250ccm engine, and considering the tabulated laminar flame properties, operating conditions for both, the RCEM and engine have been specified which guarantee comparability in the Borghi diagram.

A wide range in operating conditions has been characterized in the 250ccm engine in WP4.3. This data has been post-processed within WP3 with particular focus on the influence of the hydrogen addition on cycle-to-cycle variations for fixed ignition timings at different methane/air equivalence ratios, thereby providing a broad database for further model development and validation.

4.2 **Main achievements of WP3**

a) Spark-induced breakdown spectroscopy

SIBS in air, methane and hydrogen and the impact of pressure, gating and delay on spectra

Spectral analysis of the light emission produced by the igniting spark and the subsequent combustion can provide information on the species present in the spark and/or the flame kernel. By use of the spontaneous emission it is ascertained that the signal stems from the volume of interest - the spark channel and the flame kernel. Experiments were carried out in a heatable high pressure cell equipped with windows for optical access to the spark plug region as shown in **Fehler! Ungültiger Eigenverweis auf Textmarke.**. A remote-controlled gas supply system permits filling of the cell with pure gas or defined mixtures of fuel (CH_4 and H_2) and air. Commercially available spark plugs were used.

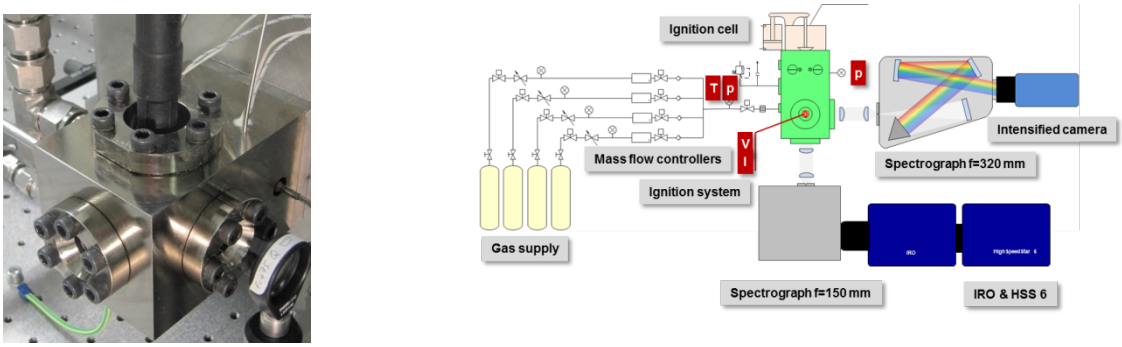

Fig. 4.1 Optical ignition cell and schematic of the ignition test rig at Empa-APTL

For some measurements an "optical spark plug" was employed (*vide infra*). Spectroscopic signals were analyzed with a spectrograph (Princeton Instruments Isoplane 320) and detected with a gated, intensified CCD camera sensitive to visible and UV light (Model: PCO DicamPro). For triggering the electronic shutter of the camera either the falling edge of the coil charging pulse was used or the current rise in a fast probe attached to the spark plug was detected using a high-speed comparator circuit; the latter was developed in-house at Empa.

A set of four spark-induced spectra is shown in Fig. 4.2 The test cell was filled with air, methane, hydrogen and an ignitable mixture of these three components, respectively. The signals show a marked dependence on exposure time, delay between spark breakdown and detection gate, and cell pressure.

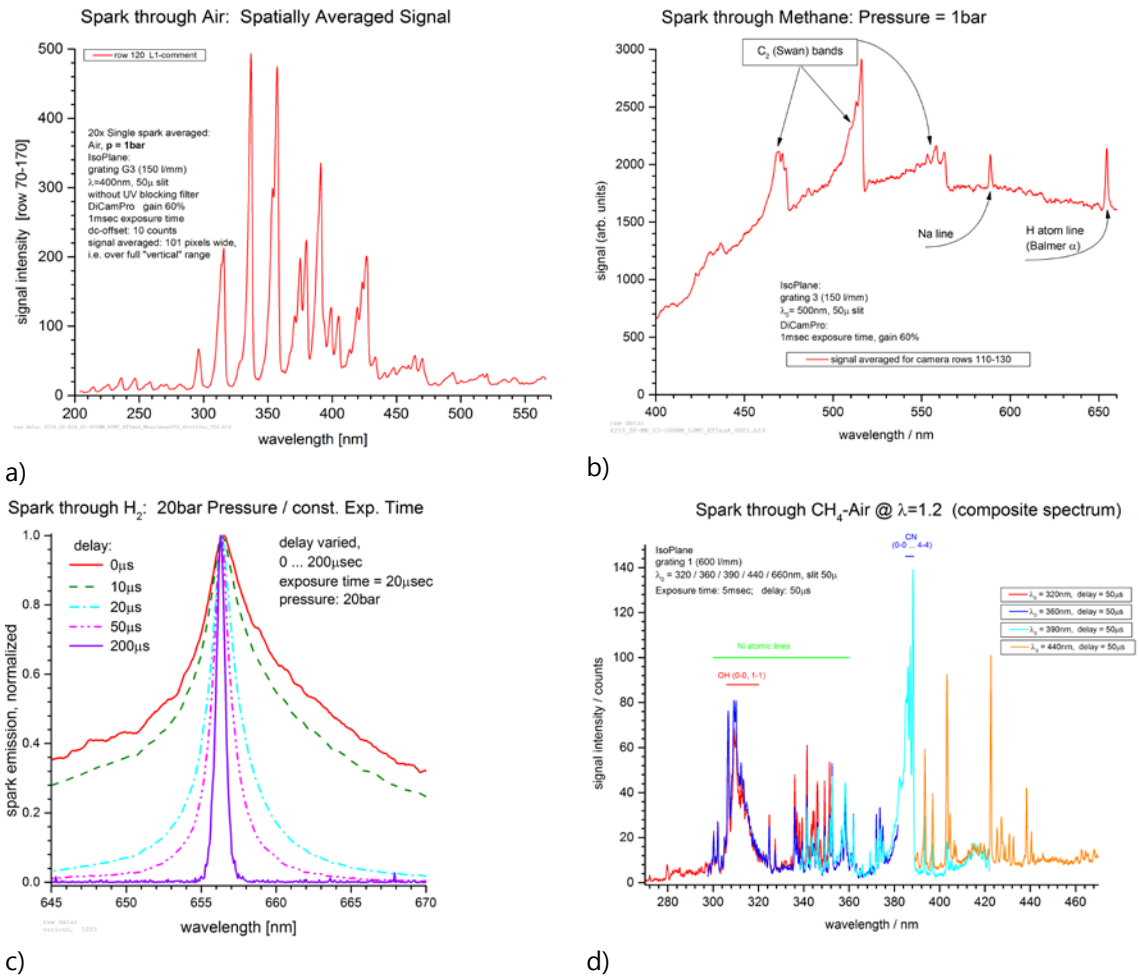

Fig. 4.2 Experimental SIBS spectra in air (a) and methane (b) at atmospheric conditions. A variation of the delay with respect to the charge signal for hydrogen (c) a composite spectrum of a reactive CH_4-air mixture at λ=1.2 (d).

The air spectrum in Figure 4.2 a) is dominated by lines from the second positive system of N_2. Oxygen atom lines become visible in the deep red region of the spectrum, beyond the range shown in this figure. Upon closer inspection it is found that in many spectra additional lines are observed which can be attributed to metals (e.g. Na, Ni, Zn). Scanning electron microscopy (SEM) for visualization combined with energy dispersive X-ray spectroscopy (EDX) for the material composition had been employed, validating the presence of nickel, zinc and sodium in the electrode alloy.

Spectra of pure methane show signals attributable to C_2 (the Swan bands) and, with lower intensity, to CH. Additionally, it was found that some signal due to atomic hydrogen appears, an indication that methane is decomposed by the spark.

The signal from pure hydrogen in Fig. 4.2 c) shows the Balmer alpha atomic line. The Balmer lines exhibit a strong broadening, which is only in part attributable to "ordinary" pressure (collisional) broadening. The Stark effect, caused by the high electric field strength in the spark, is the major contribution to the line width. At elevated pressures, a very substantial broadband background is found; most of this is caused by plasma emission, but some of it may also be due to the far wing of the strongly broadened hydrogen lines.

Spectra of reactive mixtures (methane-air or hydrogen-methane-air) exhibit an overlay of the spectra of the individual components, with varying amplitudes. With somewhat longer exposure times there also appear spectral signatures of flame species, e.g. chemiluminescence of the OH and CN radicals. Again, metal lines appear; this can make the analysis somewhat cumbersome. For example, it was found that fairly strong lines of Nickel overlap the spectrum of OH near 310 and 313nm.

The Hydrogen atom signal shows an asymmetry which is discernible in Fig. 4.2 c). The standard spectral line profiles (Gaussian, Lorentzian, Voigt profile) cannot account for this. A likely explanation is the temporal integration over widely variable degrees of Stark broadening and shifting in the transient spark.

Air-fuel ratio quantification

Well-known spectral features of hydroxyl (OH), nitrogen monohydride (NH) and cyanogen (CN) [1-3] for SIBS have been investigated at different conditions in the ignition cell. A rather high scatter from one ignition event to the next was observed and the low sensitivity of these features on the air-fuel ratio could not be reproduced. Moreover, strong interference of metal emission lines, namely nickel emissions, was found in the range from 300-400 nm. Therefore, different spark plugs geometries and electrode materials were considered to reduce the cyclic variability and signal interference. Fine wire noble metal electrode tips of iridium and platinum on the center and the mass electrode showed the best performance.

Although OH, NH and CN are very prominent SIBS signatures in the near UV range, no distinct dependency on the air-fuel ratio was found. Therefore, further investigations on atomic emission lines from nitrogen, oxygen and hydrogen have been conducted in the range from 480-800 nm as illustrated in Fig. 4.3 a).

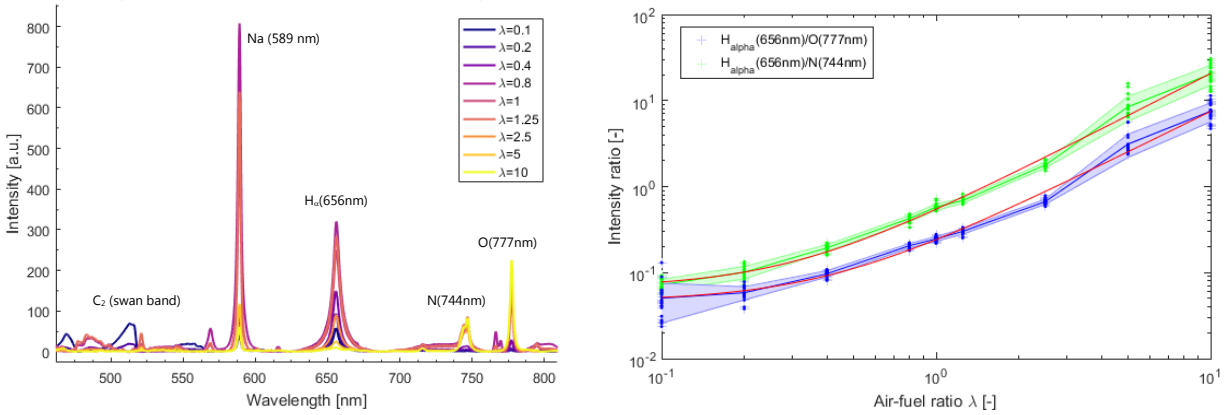

a) Background corrected SIBS spectra for various air-fuel ratio under reactive conditions at 10 bar

b) Intensity ratio of two atomic lines from hydrogen, nitrogen and oxygen at 10 bar

Fig. 4.3 Air-fuel ratio quantification based on SIBS emissions between 480 and 800 nm for methane-air mixtures

Although those emissions are weaker compared to the CN and OH respectively, signal ratios of H_α(656 nm) over N(744 nm) and O(777 nm) show an explicit dependency on the air-fuel ratio with overall higher intensities for oxygen. However, regarding hydrogen enrichment of methane, no distinction can be drawn with respect to the fuel composition. For rich mixtures below the extinction limit, C_2 swan band emissions can help to overcome the limitations of the very low emissivity of oxygen and nitrogen.

In order to conduct air-fuel ratio quantification in an engine, a full calibration map with respect to pressure, air-fuel ratio and hydrogen enrichment ratio should be provided. Proper distinction of hydrogen originating from methane and from molecular hydrogen inhibited the applicability of the measurement technique. Moreover, strong window fouling on the sapphire rods of the optical spark plug limited the use of the optical spark plug in the engine

Temporally resolved SIBS

Gating of the camera with respect to the breakdown event, together with the spectral range and resolution are key questions in SIBS as shown in *Fig.* 4.2 c). By resolving the temporal evolution of the spark-induced emission signal, eventual changes within a spark-event can be observed. *Fig.* 4.4 b) shows the temporal evolution of ensemble averaged ignition events from the near ultraviolet (280 nm) to blue (440 nm) range for stoichiometric mixtures of methane in air at 10 bar. A major trade-off for temporally-resolved spectroscopy is the huge intensity gradient between the breakdown-, arc- and the glow phase, respectively. Breakdown- and arc-phase are very short and powerful. The breakdown phase is typically in the order of nanoseconds at very high power (up to megawatts) and rather small energies. The arc phase lasts usually for microseconds at lower power and still a small share of the total energy supplied. Although the glow discharge operates at the lowest power, most of the energy is supplied in this phase, primarily due to the extremely long duration of up to 2 ms for the ignition system under consideration. Because of the limitations with respect to repetition rate and dynamic range of the high-speed intensifier and camera, focus was put on the last phase at a recording rate of 100 kHz for the spectral signals. At the earliest time, the spectrum is dominated by a spectrally broad continuum background emission from Bremsstrahlung. These very strong background emission levels were found during breakdown and arc, when signal saturation could not be avoided. During the glow discharge, generally dropping intensity levels can be observed over time, in line with the supplied power to the secondary circuit of the ignition system. Moreover, during the first 100 µs, considerable fluctuations in time at a rate of 51°kHz were observed on both, the secondary power and the averaged intensity in the spectra, dampened 200 □ s after the breakdown event. The electrically oscillating dampened circuit of the coil ignition system is characterized by the resonant frequency on the current and given by the inductance, capacitance and resistance of the ignition system. This effect must be considered for the successful application of SIBS in coil ignition systems. These findings are in preparation for publication in the Journal Spectrochemica Acta Part B.

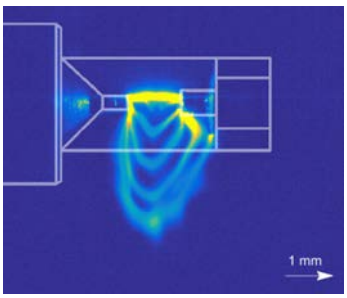

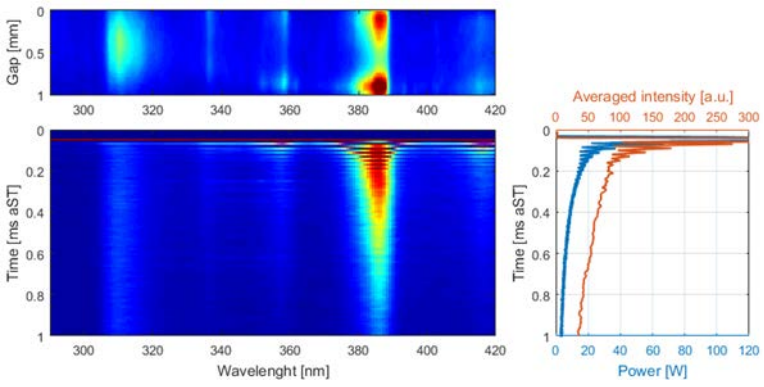

a) Multi-exposure of the plasma channel deflection in the RCEM

b) Conventional one dimensional SIBS spectra along the electrode gap and temporally resolved vertically averaged SIBS spectra. Averaged temporally resolved intensity compared to measured secondary power.

Fig. 4.4 Plasma channel deflection in a turbulent flow field in the RCEM (left) and temporally-resolved SIBS under quiescent conditions in the ignition cell

Considering spark-induced emission spectroscopy as a diagnostic tool for in-cylinder investigations in engines, the effects of the local flow field on the plasma channel must be additionally considered. Local disturbances will deflect the plasma channel, forcing re-attachments and re-strikes and therefore further affect the temporal evolution of the spectroscopic signal as illustrated in Fig. 4.44 a). Acquiring the current and voltage signal on the secondary side of the ignition system helps to identify re-attachments and re-strikes of the plasma channel and, most importantly improving the signal quality in SIBS measurements.

Optical spark plug

Based on the findings in the ignition cell, an optical spark plug suitable for engine application on the SA 250 engine was elaborated. The requirement specifications included optical fibers (OF) for spark-induced breakdown spectroscopy as well as fibers to determine the flame front arrival of the early flame kernel.

For SIBS, a large numerical aperture of the fibers and a viewing direction towards the electrodes were required to collect the plasma signal. Two dedicated sapphire crystals were put next to the mass electrode with a 60° chamfer. To ensure that both electrodes are within the field of view, a cone angle of 20° was chosen. The base spark plug (NGK DIMR8A10) with two laser welded noble metal electrode tips of iridium and platinum, respectively, showed the best performance in the pretests with respect to reduced cycle to cycle variability and low interference of metal emission lines.

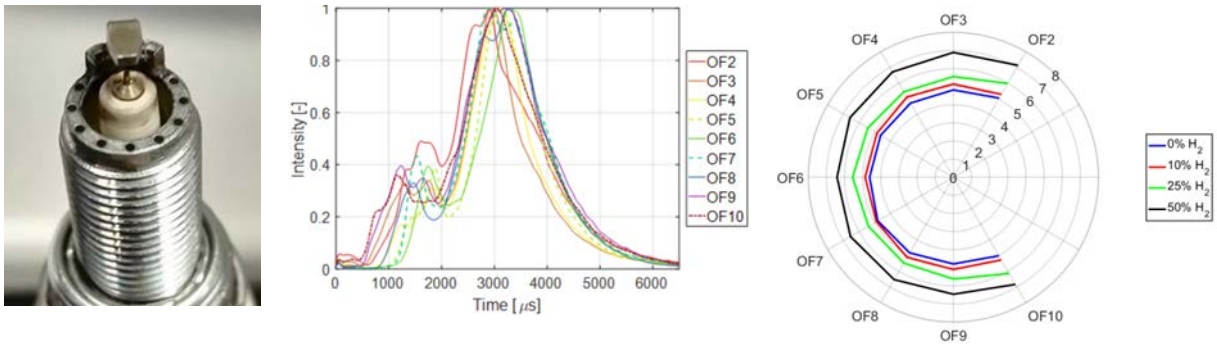

a) M10 optical spark plug

b) Temporal evolution of the PMT signal on nine individual optical fibers at λ=1.4 for methane, time after spark timing.

c) Flame propagation speed on all fibers at λ=1.0 for different hydrogen enrichment ratios

Fig. 4.5 Optical spark plug for SIBS and flame front arrival measurements in a fired engine.

Nine dedicated fibers to determine the flame front arrival of the early flame kernel were arranged in the circumferential direction as indicated in Fig. 4.5 a) with a narrow opening angle of 7°. An array of filter housing, photomultiplier tubes and amplifiers for the detection of the flame front was designed to amplify and convert the optical signals from the flame.

Tests on the ignition cell and in the fired engine revealed that the chemiluminescence signal of OH* during the early stage of flame formation cannot be amplified to an acceptable level to unambiguously detect the flame front arrival. Therefore, unfiltered measurements had to be performed to achieve an acceptable signal to noise ratio.

An example for the temporal evolution of the filtered and normalized PMT signal is shown in Fig. 4.5 b) for a fired engine running at 3000 rpm, fueled with methane at an air-fuel ratio of 1.4 and a spark advance of 45°CA. The first peak indicates the flame front passing the optical fiber, the second peak attributes to the flame luminosity during the main heat release. Based on this data, the flame front propagation was derived for different hydrogen enrichment ratios as illustrated in Fig. 4.5 c).

The method development of SIBS continued, the integration of optical fibers on a spectrograph was successfully tested and compared with the standard SIBS setup. Good agreement was found with respect to spectral characteristics, however, signal intensity, spectral and spatial resolution were reduced but still at acceptable levels in the ignition cell. The application of SIBS via the optical spark plug on the RCEM and in the engine revealed the challenges of the perturbing flow field and fouling on the sapphire rods on the SIBS signal quality. The challenging application of SIBS in an engine environment remains pending, further investigations are ongoing.

b) Laminar and turbulent premixed hydrogen enriched methane combustion in the RCEM

Turbulent flow field generation and validation

Two different mechanisms have been investigated for the turbulence generation in the RCEM. A first approach was considering a stepped piston and an insert in the combustion chamber with four overflow channels. Although the desired levels of the turbulent fluctuation speed u' could be achieved in the RANS simulations, the design was rejected for two main reasons: the late increase of u' with respect to spark timing and the directed flow of the four channels towards the center of the combustion chamber. In the second approach, a secondary air injection at the beginning of the fast compression stroke was examined both by numerical simulations and experimentally. For this purpose, the six-hole nozzle tip of a prototype Hoerbiger gas injector was modified to a single hole injector as indicated in Fig. 4.54.5. Two different injection directions were considered by varying the exit angle of the nozzle from 10° to 30°, respectively. Moreover, the specification allowed operating the injector above the critical pressure ratio, causing choked flow conditions and creating an under expanded jet. The pressure ratio (PR) across the injector was considered as an additional parameter to adjust the desired levels of turbulence intensity.

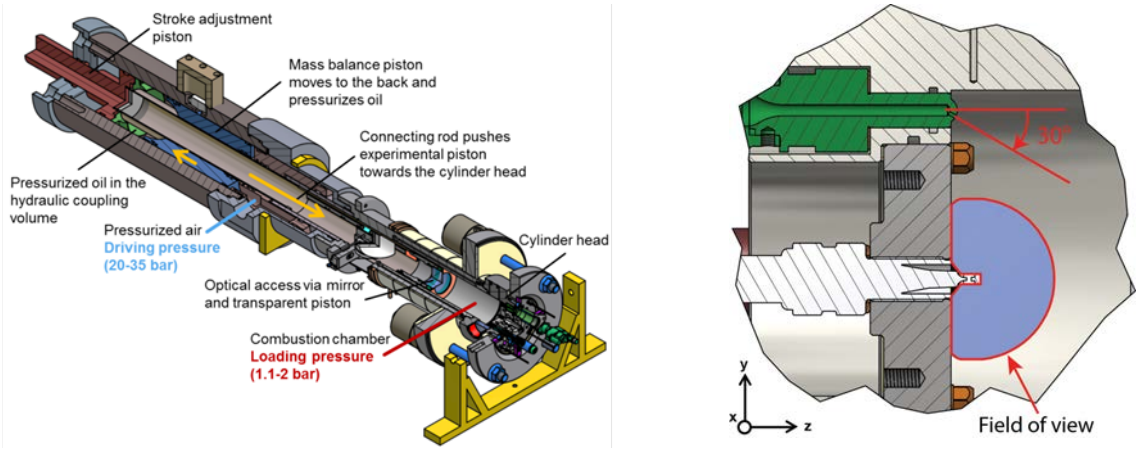

a) Working principle of the rapid compression expansion machine

b) Field of view through the lateral windows on the spark plug.

Fig. 4.5 Schematic of the rapid compression expansion machine and a cut through the cylinder head showing the spark plug orientation and the orifice of the Hoerbiger nozzle tip

Experimental investigations of the 30° nozzle exit angle were performed on a compression stroke in the RCEM by applying temporal-resolved particle image velocimetry (PIV) measurements, using the recently acquired high speed Nd:YAG laser and a monochrome high-speed camera. Injection timing of the secondary gas injection was fixed to 7 ms and 30 mm after bottom dead center (BDC) position, approximately 30 ms before top dead center (TDC) as indicated in Fig. . The resulting flow fields from the PIV data confirmed the general suitability of this method to generate the desired turbulent fluctuations speeds at ignition timing, although a comparably high convective term at the electrodes was found. Because of the limited optical accessibility in the RCEM and to make use of experimental results for modelling purposes, RANS simulations were performed to capture the in-cylinder flow conditions.

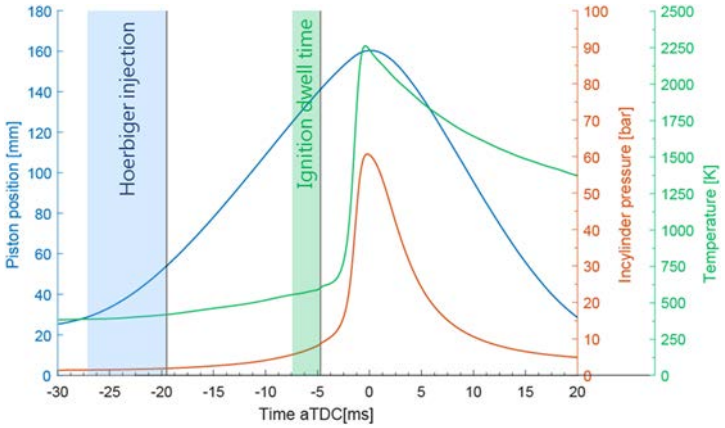

Fig. 4.6 Piston position, in-cylinder pressure and temperature traces and injection and ignition timing for a characteristic RCEM experiment

Therefore, the mass flow rate though the injector was derived and the position of the Mach disc of the underexpanded jet was determined in a constant volume arrangement and under transient conditions using high-speed Schlieren imaging.

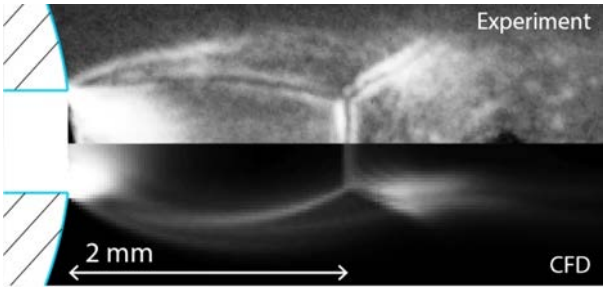

a) Experimental and numerical Schlieren image of the barrel shock

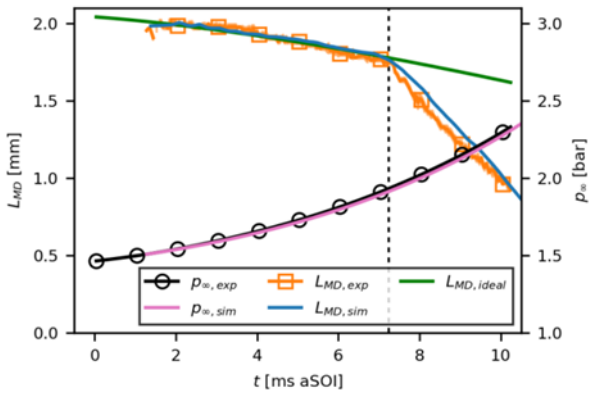

b) Comparison of Mach disc position and in-cylinder pressure

Fig. 4.7 Experimental and numerical comparison of near nozzle region of the secondary air injection

The PIV data has been compared with the CFD in order to validate the numerical predictions and to support interpretation of the optically non-observable regions. Good agreement of the flow structures was found and the predicted turbulent fluctuation speeds were in accordance with the measurement. However, the characteristic increase in u' during the tumble breakdown is shifted towards a later timing in the CFD, leading to a considerable overestimation of the magnitude of the mean flow ū at spark timing. Future numerical work should be devoted towards an improved prediction of the velocity magnitude at this instance in time. The global flow field outside the optically accessible area has been further discussed based on the CFD prediction, where the tumbling motion has been identified.

The flexibility of the turbulence generation has been demonstrated experimentally. Two pressure ratios over the injector (i.e. 20 and 40) have been compared to a setup without injection. Spatially averaged turbulent fluctuation speeds around the spark plug reached values of 4 and 5 m/s at spark timing and mean velocity magnitudes of 1.5 m/s for the two pressure ratios. This allows the investigation of reactive cases at different turbulent fluctuation speeds. The PIV data showed considerably increased turbulent fluctuation levels within the optically accessible area, when compared to the operation without the secondary gas injection as indicated in Fig. 4.74.7 b).

The local mixture stratification has been analyzed based on the CFD data. A relatively homogenous distribution of the air-to-fuel ratio has been found, as the injected air is well-mixed with the surrounding air-fuel mixture. This enables the reactive investigation of a homogenously premixed charge, relevant to port fuel injected engines. These findings have been published in [4] and presented at the SAE Conference on Engines and Vehicles, Sept. 2017 in Capri, Italy.

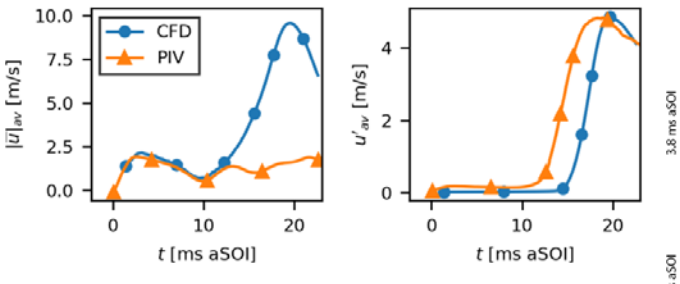

a) Comparison of the mean velocity magnitude and the turbulent fluctuation speed in a 15x15 mm² box around the spark plug as indicated in Figure c) for the pressure ratio PR=20.

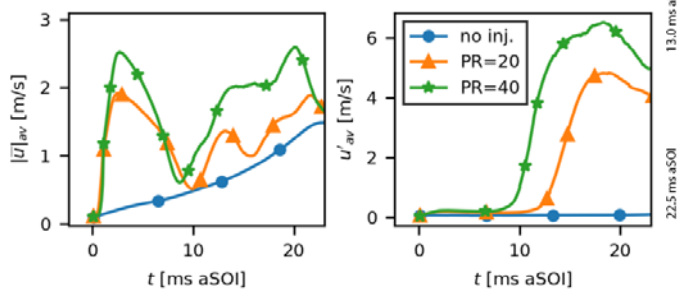

b) Experimental variation of pressure ratio across the injector and its impact on the mean velocity magnitude and turbulent fluctuation speed

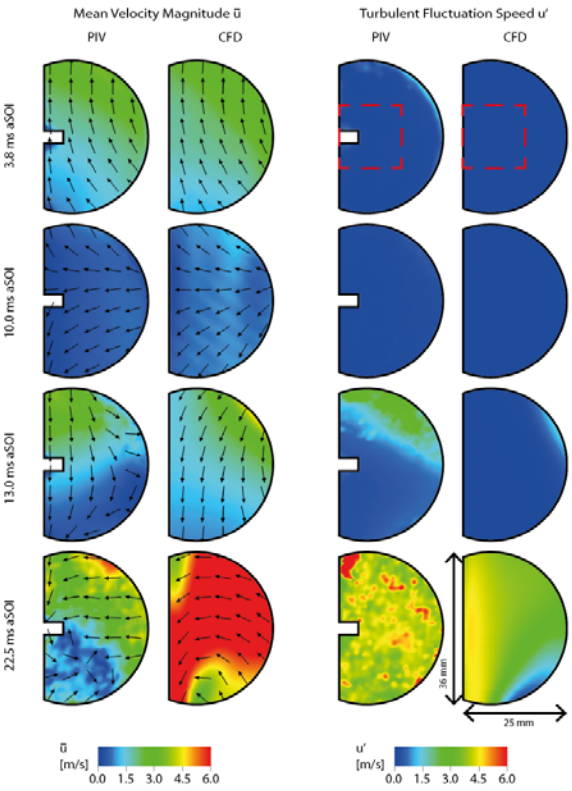

c) Comparison of the flow field in the simulation and the PIV images for a pressure ratio PR=20 through the lateral window in the RCEM

Fig. 4.7 Comparison of flow field around the spark plug location measured by PIV and computed by detailed RANS simulations

Impact of hydrogen enrichment and turbulence levels on early flame kernel formation

Reactive tests under lean conditions have been performed for three different turbulence levels based on a variation of the pressure ratio (PR) between rail and in-cylinder pressure of 10, 20 and 40. Planar time-resolved particle image velocimetry (TR-PIV) along the cylinder axis was used to characterize the flow field in the RCEM. Findings from former PIV measurements regarding optimum seeding density and laser sheet positioning improved the quality of the resulting flow fields. Simultaneously, a high-speed camera coupled to a high-speed image intensifier with a UV lens and a 307 nm filter was used to capture the OH* chemiluminescence signal from the early flame.

Additionally, the in-cylinder pressure was monitored and subsequently heat release rates have been calculated. The timing of the secondary air injection was fixed to the piston position at 30 mm, when the fast pneumatic compression stroke is initiated. Pressure based spark timing was chosen to ignite the mixture at similar p,T-conditions for all fuels of 10 bar and 600 K, respectively as shown in Fig. 4.6.

Ensemble averaged velocity and turbulent kinetic energy increased by 50% and 100%, respectively within the field of view when comparing the cases for PR=10 with PR=40. With increasing pressure ratio, the arrival time of the tumbling flow at the cylinder head advanced. Therefore, differences at spark timing with respect to turbulence intensity were lower. Moreover, mean velocity at spark timing is still considerably high with 4-6 m/s. Reactive tests demonstrated that the evaluation of the flow field after ignition in the unburnt region is still possible, although the number of valid velocity vectors is reduced. Fig. 4.8 illustrates the overlay of the apparent flame area and the flow field for methane and the 10, 25 and 50% hydrogen enrichment in methane at λ=1.6 and a pressure ratio of 40 for four individual cycles.

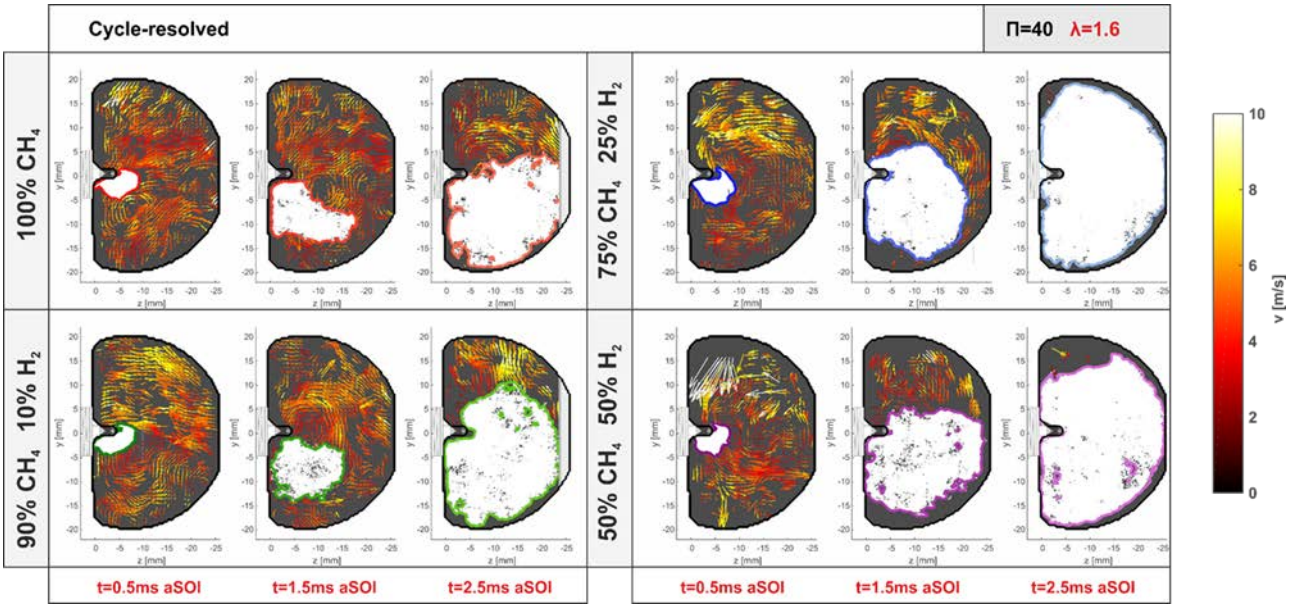

Fig. 4.8 Flow field and apparent flame area for the different hydrogen enrichments of methane for a pressure ratio of 40 at λ=1.6.

Based on the OH* chemiluminescence images an apparent flame area was calculated and the time, when a flame passed a specific apparent area (100, 200 and 300 mm^2) was calculated as indicated in Fig. for different pressure ratios. A comparison of the specific mass fractions burnt and the apparent flame area in *Fig.* reveals that within the field of view of the OH* chemiluminescence setup only the early phase could be covered up to 2% of the relative heat release.

Although the turbulent fluctuation speed varies between the different pressure ratios, the impact on the early flame kernel is minimal, the duration from spark timing to an apparent flame area of 100 mm^2 differs from the percentage of hydrogen enrichment, but no significant difference can be found from the three pressure ratios.

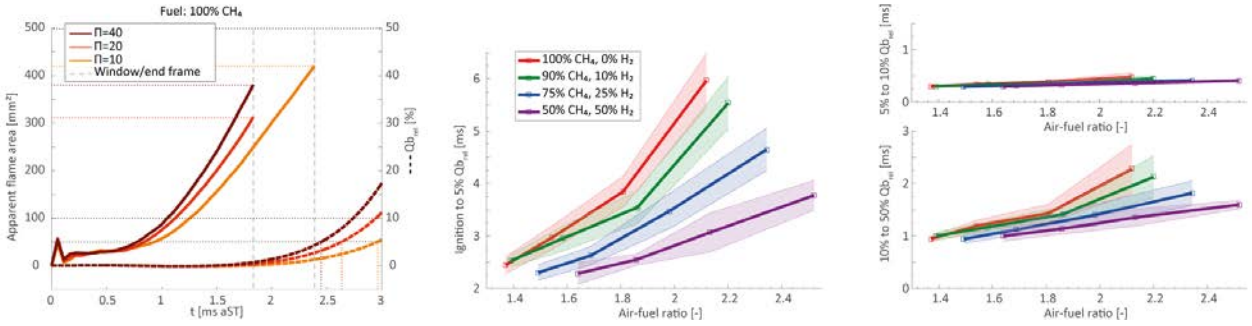

Fig. 4.9 Apparent flame area from OH* chemiluminescence compared to the mass fraction burnt (MFB) from the heat release rate calculations. Impact of different pressure ratios for methane (left) and impact of hydrogen enrichment for PR=40.

Comparing the hydrogen enrichment rates on the duration until a certain mass fraction is burnt (ignition to 5%,5%-10% and 10%- 50%) over the air-fuel ratio, points out the benefits of the higher reactivity of hydrogen on the faster combustion already at the very early stage of inflammation, especially for lean operating points. These benefits are much less pronounced in the later stages of combustion as indicated in the plots from 5 to 10% MFB and 10 to 50% MFB.

c) Modeling of the turbulent flame speed

Laminar flame speed

Many models in use for 3D-CFD of turbulent premixed flames in IC engines require the formulation of a turbulent flame speed to advance the flame front.As a sound basis for the turbulent flame speed closure, characteristics such as the laminar flame speed s_L^0 and laminar flame thickness d_L^0 of the corresponding laminar flame have to be known, which are functions of the evolving chemico-physical conditions in the chamber (pressure/temperature and composition). Measurements and correlations for the laminar flame speed of hydrogen enriched methane have been proposed in [5-7] and reviewed in [8]. However, no correlations for the laminar flame thickness can be found.

Simulations of 1-dimensional steady flames based on detailed chemistry allow extensive tabulation of flame properties. The chemical reaction mechanism GRI Mech 3.0 [9], consisting of 325 reactions and 53 species, has been vastly validated for methane as well as hydrogen combustion and is considered for of the methane-hydrogen admixtures of this project. The Cantera framework [10] is used to compute the structure of freely propagating laminar premixed flames. A comparison of literature data and the numeric prediction of the laminar flame speed at atmospheric conditions for pure methane-air combustion for a wide range in air-to-fuel ratio can be found in Figure 4.5. The predictions lie within the scattering of the measurements. Analogous, a comparison for a mixture consisting of 20%Vol hydrogen is shown in Figure 4.6. Again, the numerical prediction is within the scattering of the measurements and shows a particular good agreement with the data by Hermanns et al. [8].

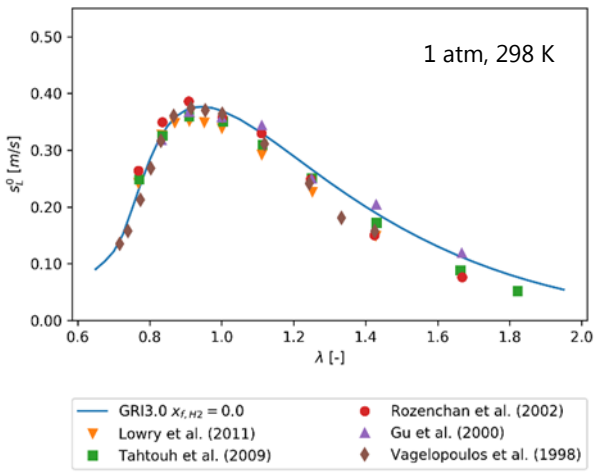

Fig. 4.10 Laminar flame speed for100% CH_4 at 1 atm and 298 K. Solid line: model prediction, markers: measurements

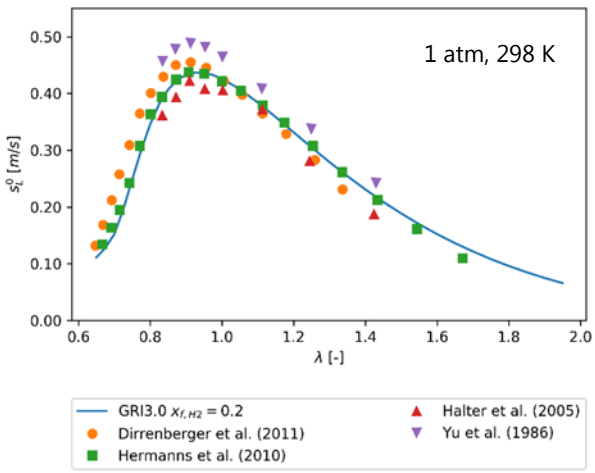

Fig. 4.11 Laminar flame speed for 80% CH_4 / 20% H_2 at 1 atm and 298 K. Solid line: model prediction, markers: measurements

An efficient numerical method was developed to facilitate the tabulation over a wide range in pressure, temperature, air-to-fuel ratio as well as hydrogen content present in this project. Table 4.1 shows the considered ranges and discretization, resulting in 32'340 and 19'404 calculations for the hydrogen and EGR sweep respectively.

Table 4.1 Discretisation of the tabulated laminar flame properties

	P [bar]	Tu [K]	□ [-]	$x_{f,H2}$ [%]	EGR [%]
Range	1-80	600-1'000	1.0-2.0	0-50	0-20
Points	28	21	11	5	3

An excerpt of the tabulation is shown in Figure 4.12 for ignition relevant conditions at 10 bar and 600 K. The characteristic evolution of the laminar flame speed and thickness for different hydrogen contents for changing air-to-fuel ratios can be seen. Increasing the hydrogen content leads to higher burning speeds and smaller thickness, as expected.

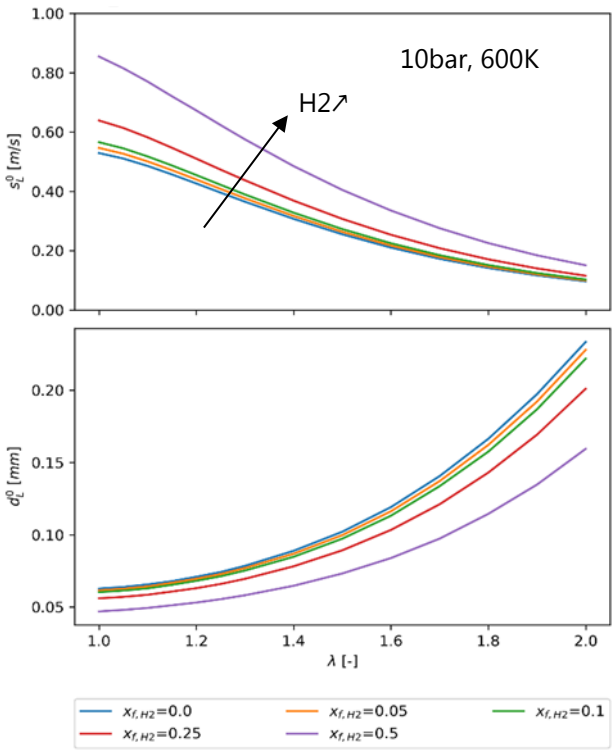

Fig. 4.12 Laminar flame speed (sL0) and thickness (dL0) as a function of air-to-fuel ratio λ for different hydrogen admixtures

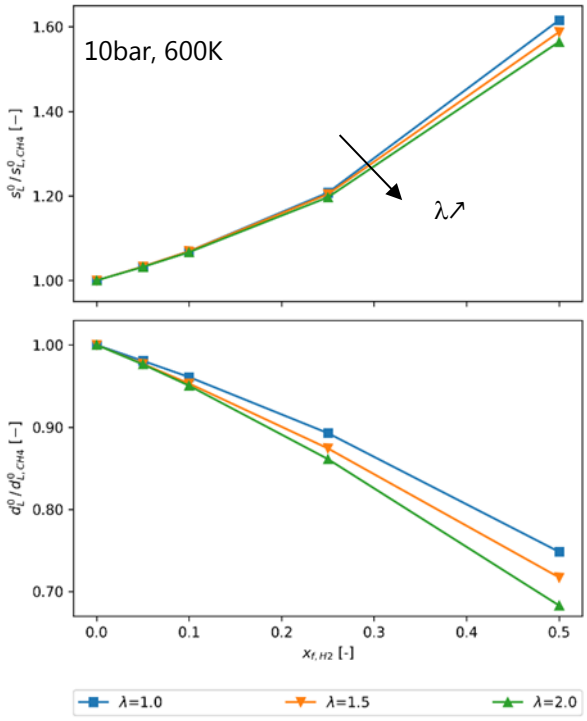

Fig. 4.13 Influence of hydrogen addition on the laminar flame speed (sL0) and thickness (dL0) normalized by pure methane for different air-to-fuel ratios λ

The relative influence of the hydrogen addition is investigated in more detail in Figure 4.13. The laminar flame speed and thickness is normalized with those of pure methane-air mixtures. A deviation from the initially linear influence towards higher hydrogen contents can be observed. This finding is emphasizing the fact that the flame properties of hydrogen admixtures cannot be modelled as a linear combination of its single component fuels, in particular for higher hydrogen contents.

Turbulent flame speed

Based on an algebraic closure for the scalar dissipation rate, a model for the turbulent flame speed was derived by Kolla et al. [11]. This novel closure has been assessed in the RANS context and validated against engine measurement data of the SA 250. In collaboration with Liebherr, a large bore engine operated with natural gas under lean conditions has been considered additionally. A sweep in turning speed was considered in order to assess the predictive capabilities w.r.t. changing turbulence quantities. It was found, that the novel tuning-parameter free model shows considerable advantage when changing the operating conditions compared to the commonly used Damköhler model, cf. Figure 4.14. The impact with respect to the choice of the turbulence model has also been assessed. The findings have been published in [12] and presented at the SAE Powertrains, Fuels and Lubes meeting, Oct. 2014 in Baltimore, USA.

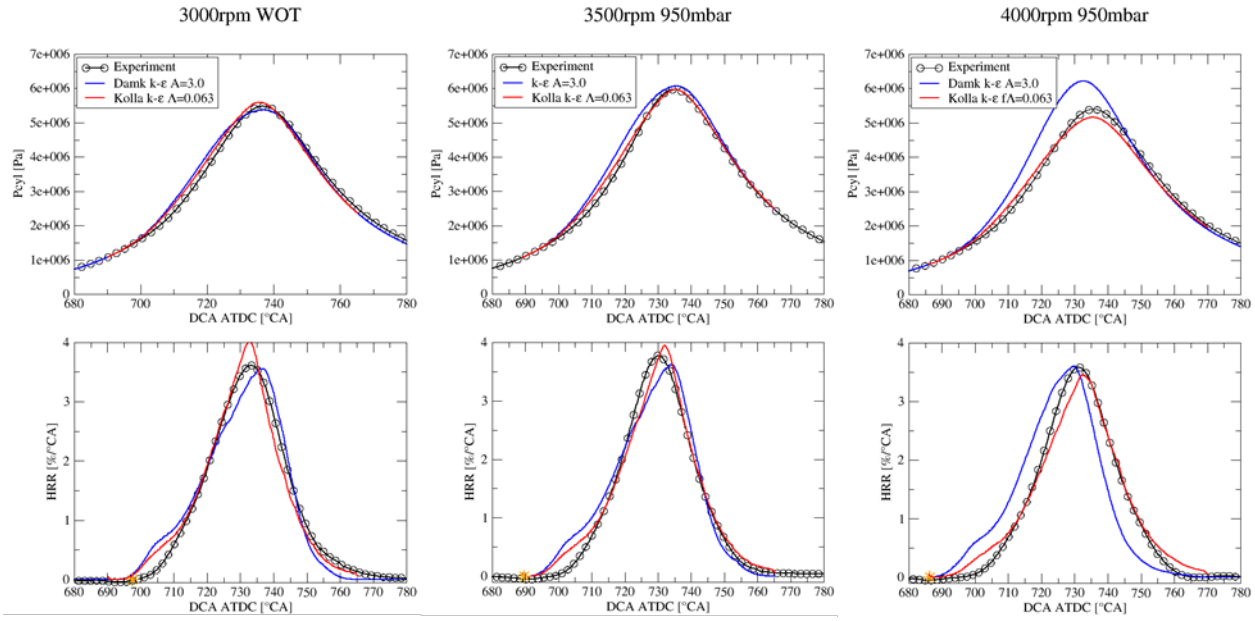

Fig. 4.14 Pressure trace (top) and heat release rate (bottom) for a sweep in turning speed at constant load. Model parameters adjusted for 3500 rpm and kept constant for the other speeds for the SA 250 engine.

Motivated by the good agreement in the RANS context, the flame speed closure valid in the LES context has been derived. This is based on a closure of the SDR in the LES context [13], and following the same KPP analysis as previously performed:

$$s_T = \left\{ \frac{8\nu_T}{(2c_m - 1)\beta_c} F\left[2K_c^* \frac{s_L^0}{d_L^0} + (C_3 - \tau Da_\Delta)\left(\frac{2u'_\Delta}{3\Delta} \right) \right] \right\}^{\frac{1}{2}}$$

Here, K_c^*, s_L^0 and d_L^0 are fuel specific constants, depending on the unburned state of the fresh mixture and are taken from the tabulated laminar flame database. In the RANS context β_c can be taken as a constant and represents the effects of flame curvature on the burning speed. A sensitivity study of this parameter has been presented in [14]. In the LES context, as shown in [13], β_c can either be determined dynamically or presumed constant, as it will be considered here.

The flame speed closure is currently assessed in a generic engine-like geometry, for which DNS data is available. There, a lean mixture of syngas is used with a Lewis number that correlates to a methane-hydrogen admixture of 10% hydrogen as can be seen in . The work is currently prepared for publication and presentation at the SAE World Conference 2018 in Detroit, USA.

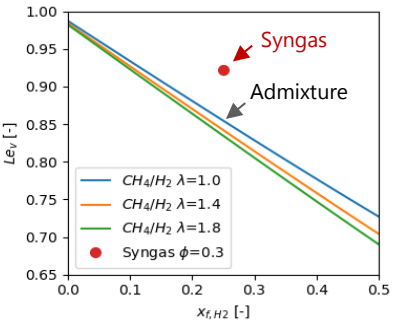

Fig. 4.15 Lewis number of methane-hydrogen admixtures as function of the hydrogen content and the considered

c) *Length and velocity scale ratios for RCEM and SA250*

The length scale ratio Λ/d_L^0 as well as the velocity scale ratio u'/s_L^0 relate the laminar flame properties (namely the flame speed and thickness, which depend solely on the physico-chemical state)to the surrounding turbulent flow field (characterized by the integral length scale and turbulence intensity). This allows the categorization of the resulting turbulent flame into distinct regions within the Borghi diagram (Figure 4.16).

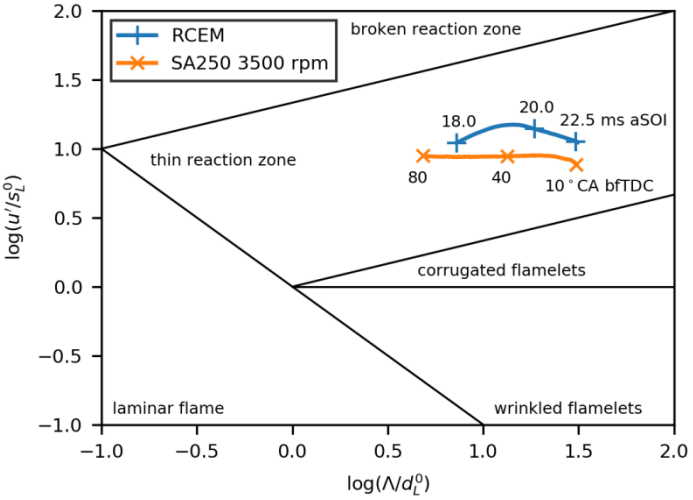

Fig. 4.16 Borghi Diagram for the two coordinated test rigs under consideration for different ignition timings

Here, it is sought after to coordinate the operating conditions at ignition timing between the RCEM and the SA 250 in order to realize turbulent flames within the same regions relevant to IC engines despite the different turbulent flow fields within these two test rigs. The available PIV data has been considered for the characterization of the turbulent flow field in the RCEM, CFD simulations estimated the turbulence quantities within the SA 250 full metal engine. Then, the laminar flame speed and thickness were taken from the generated database to compute the length and velocity scale ratio, allowing for characterization in the Borghi diagram. The operating conditions in the RCEM (wall temperature and start of compression pressure and air-to-fuel ratio) and SA 250 (air-to-fuel ratio) have then been adjusted to achieve a match in the Borghi diagram as can be seen in Figure 0 as a function of the ignition timing.

d) *Premixed hydrogen enriched methane combustion in the SA 250*

<u>Validation of the LES framework</u>

StarCD licensed by Siemens (formerly CD-Adapco) is used as the CFD platform. The LES framework including the proposed combustion modeling has been assessed in [15]. Here, previously existing engine test bench data for gasoline operation has been used focusing on the cycle-to-cycle variations of the pressure trace. The numerical predictions were in good agreement with the experimentally observed bandwidth. A grid sensitivity study identified the minimal grid requirements. Fluctuations in the local turbulence quantities around the spark plug at ignition timing have been found to be the main driver of the pressure fluctuations., Local variations in terms of composition (internal residuals) and temperature had a negligible impact.

<u>Engine Measurements at fixed spark timing</u>

The impact of hydrogen addition on engine efficiency and emissions has been experimentally investigated as part of WP 4.3 following a tuning for maximum break torque (MBT) by adjusting the spark timing. In order to isolate the effect of different fuel compositions from changing ignition conditions (pressure, temperature, flow field) for varying MBT spark timings, the spark timing has been kept constant for the variation in fuel composition and turning speed.

The only recently made available experimental data has been post-processed focusing on the influence of the hydrogen addition on flame propagation and the cycle-to-cycle variations of the in-cylinder pressure trace. This data constitutes the basis for ongoing LES simulations.

Influence of the H_2 addition on the phase averaged cycle

In the following, a reference operating point for a spark timing at 64°CA bFTDC at 3000 rpm is investigated for a sweep in fuel composition. Figure 4.17 shows the experimental phase averaged in-cylinder pressure traces as well as relative heat release rates (HRR) for a lean mixture of λ=1.4 and changing hydrogen content. For higher hydrogen fractions a considerably faster conversion of the fresh mixture can be observed, leading to higher in-cylinder peak pressure at earlier timings.

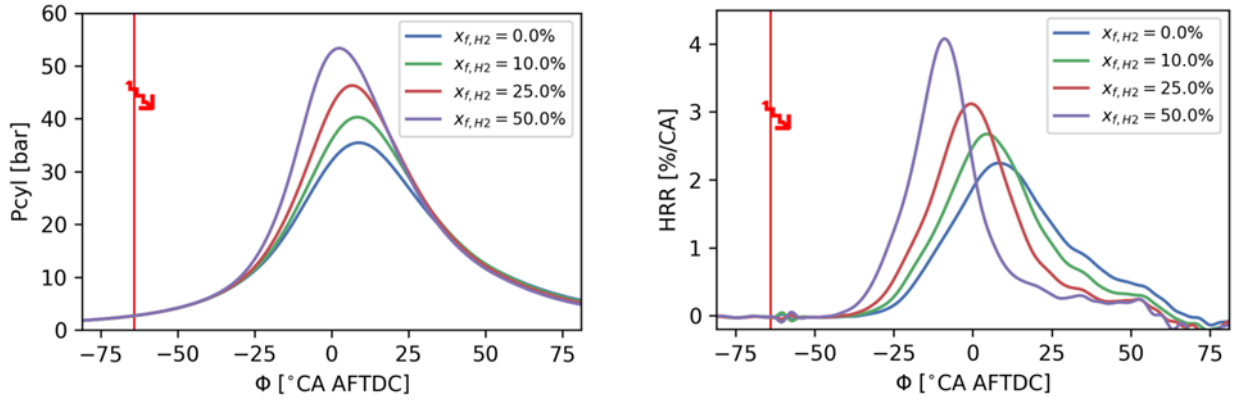

Fig. 4.17 Phase averaged in-cylinder pressure (left) and relative heat release rate (right) for lean operation (λ=1.4) and different hydrogen additions, sparking fixed at 64°CA bFTDC at 3000rpm

This speed up is illustrated more in-depth in *Figure 0*. Here, the change in combustion phasing for 50% as well as 2% fuel conversion is indicated when compared to pure methane operation (xfH2=0) for lean and stoichiometric operation. The speedup goes linearly with the hydrogen fraction, whereas it is more pronounced for the lean conditions. When comparing the speedup for 50% and 2% mass fraction burnt, it can be observed that a substantial amount of the flame acceleration happened already at this early stage of combustion. These findings are in agreement with former studies looking into hydrogen addition in a full metal engine by means of on-board reforming [16, 17].

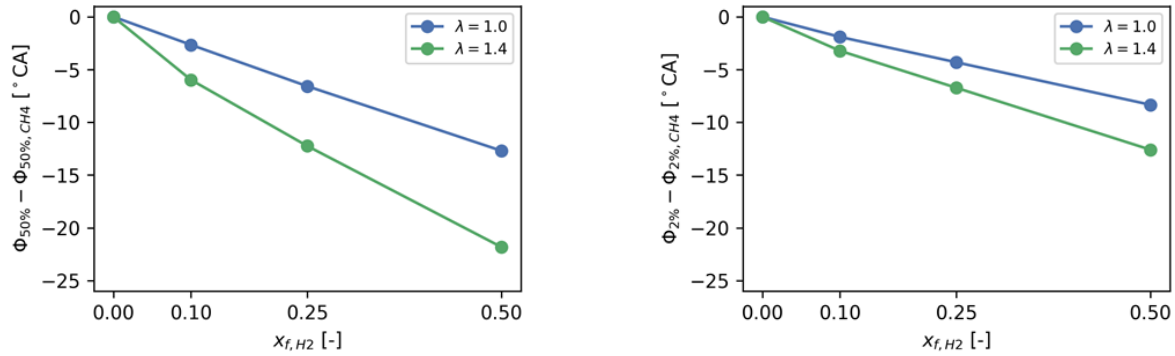

Fig. 4.18 Change in the average combustion phasing for 50% (left) and 2% mass conversion for different hydrogen fractions when compared to pure methane operation at lean (=1.4) and stoichiometric operation.

Cycle-to-cycle variations

The interaction of the flame front with the turbulent flow field leads to variations of the combustion process between consecutive cycles. These fluctuations lead to limitations of the operation range and optimal tuning of the engine as it is discussed more in-depth in WP 4.3. The standard deviation of the peak pressure is a measure to quantify the fluctuations as it is indicated in Figure 4.19 for the previously presented operating conditions at fixed spark timing. As expected, the lean operation leads to higher fluctuations, when compared to stoichiometric conditions. The hydrogen addition leads to a decrease in the peak pressure fluctuations for stoichiometry. At lean conditions, hydrogen addition seems to have a marginal impact up to 25% hydrogen, as only 50% hydrogen leads to a significant decrease in the observed fluctuations.

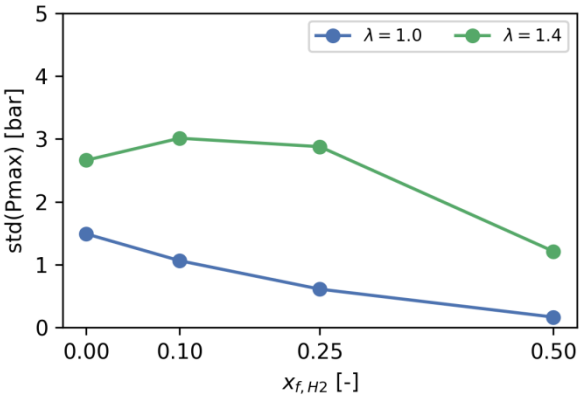

Fig. 4.19 Standard deviation of the peak pressure for different hydrogen fractions at stoichiometric and lean operating conditions

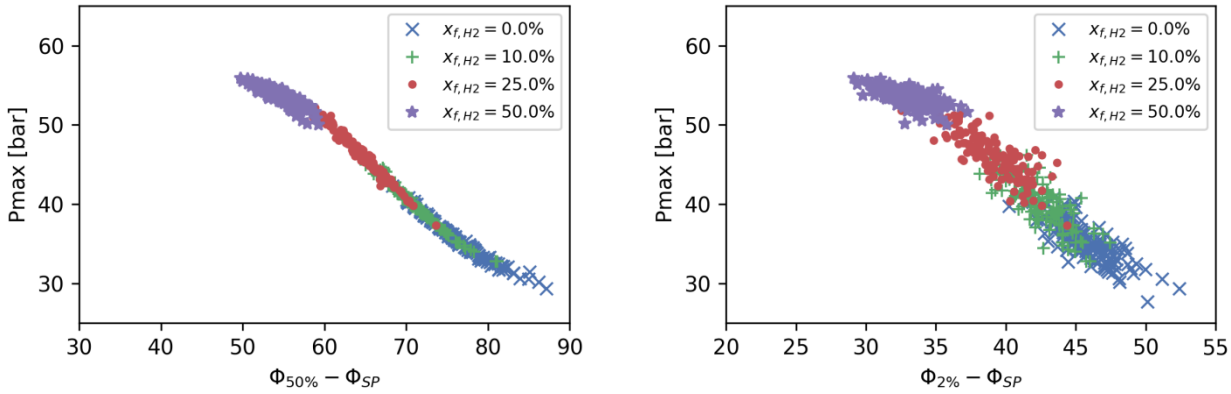

Fig. 4.20 Correlation for the peak pressure and phasing of 50% (left) and 2% (right) fuel conversion for individual cycles and lean operation (λ=1.4)

The phasing of 50% and 2% fuel conversion is correlated with the resulting peak pressure for each individual cycle for lean operation and different hydrogen fractions in Figure 4.20. There, as expected, a strong correlation can be found for the phasing of 50% fuel conversion and the peak pressure. Thus, a fast burning cycle leads to higher peak pressure. This correlation still holds, although slightly weakened, for the early flame stage, characterized by the 2% phasing. Similar observation can be drawn for the stoichiometric operation. Linearizing this correlation for each distinct hydrogen fraction, it can be shown that the sensitivity of the peak pressure towards the combustion phasing is decreased for higher hydrogen fractions.

Looking at the standard deviation of the characteristic combustion phasing in Figure *0*, a considerable reduction in the standard deviation, overall higher standard deviations for the lean operating point can be found as expected. When comparing between the standard deviation of the combustion center at 50% and the early flame at 2% for the stoichiometric operation, it can be seen that substantial deviations are already present at 2% which only slightly increase towards 50%. On the other hand, the deviations significantly increase between the 2% and 50% phasing for the lean operating point, making the combustion more affected by the later than the early phase. This effect is more pronounced for the lower hydrogen fractions.

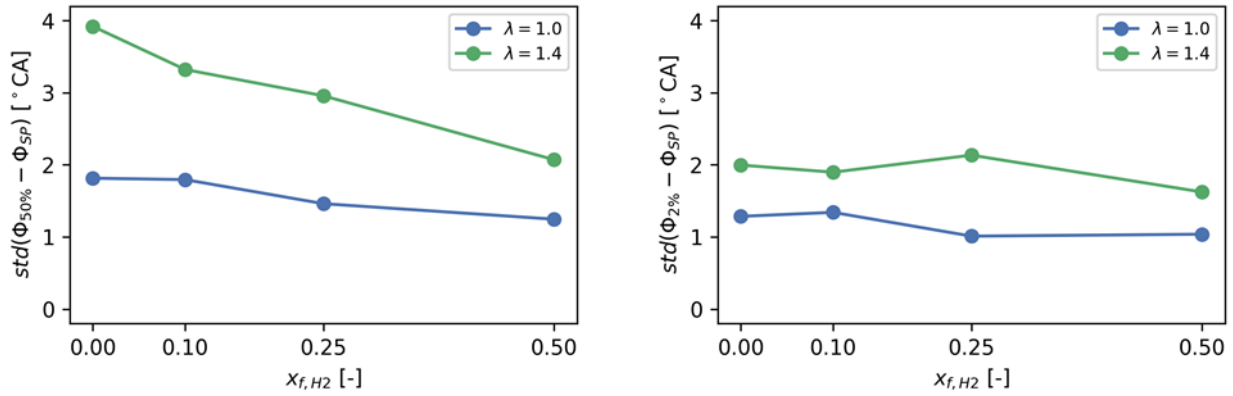

Fig. 4.21 Standard deviation of the 50% (left) and 2% (right) fuel conversion phasing for different hydrogen additions at lean and stoichiometric operation

It can be concluded that the effect of the hydrogen addition on the cyclic variability of the combustion process is threefold: (1) a small reduction in the variability of the early combustion phasing at 2% MFB for lean and stoichiometric operation and (2) a considerable reduction of the development of the variability between 2% and 50% MFB when operated lean. Additionally, the sensitivity of the peak pressure towards the combustion phasing seems to be decreased for higher hydrogen fractions.

Ongoing reactive multi-cycle CFD simulations using the validated combustion modeling will further help understanding the observed effects in terms of local quantities not accessible within the full-metal engine, such as local turbulence levels, composition and temperature as well as the directed flow velocity magnitude due to large scale bulk flow motion.

4.3 **Publications / patents**

- J. Koch, M. Schmitt, Y.M. Wright, K. Steurs, K. Boulouchos, LES Multi-Cycle Analysis of the Combustion Process in a Small SI Engine, SAE International. (2014) 17. doi:10.4271/2014-01-1138.
- Ahmed, I., Ghiasi, G., Sagaya Raj, A., Swaminathan, N., Koch, J., Steurs, K., Wright, Y.M.., Spark Ignition Engine Simulation Using a Flamelet Based Combustion Model, SAE Technical Paper 2015-24-2402, 2015. doi:10.4271/2015-24-2402.
- J. Koch, G. Xu, Y.M. Wright, K. Boulouchos, M. Schiliro, Comparison and Sensitivity Analysis of Turbulent Flame Speed Closures in the RANS G-Equation Context for Two Distinct Engines, SAE International Journal of Engines. 9 (2016). doi:10.4271/2016-01-2236.
- T. Kammermann, J. Koch, Y.M. Wright, P. Soltic, K. Boulouchos, Generation of Turbulence in a RCEM towards Engine Relevant Conditions for Premixed Combustion Based on CFD and PIV Investigations, SAE International Journal of Engines. 10 (2017). doi:10.4271/2017-24-0043.
- G. Ghiasi, I. Ahmed, Y.M. Wright, J. Koch, N. Swaminathan, Sensitivity of Flamelet Combustion Model to Flame Curvature for IC Engine Application, SAE Technical Paper 2018-24-0038, 2017. doi:10.4271/2017-24-0038.

4.5 **Industrial and institutional WP3 partner**

ETHZ-LAV & Empa-APTL

A very close cooperation was ongoing between the project members from LAV-ETHZ and APTL-Empa. Operating conditions for experiments and simulations on different test benches were constantly reviewed. In particular, the operating conditions of the RCEM in WP3.2 were closely coordinated with those of the engine measurements in WP4.3 and the interests of the simulations in WP3.1 to ensure a consistent database of validation data. Equipment was shared between labs according to specific needs.

ETHZ-LAV & Liebherr Machines Bulle

A cooperation with G. Xu (LAV / Liebherr) enabled the investigation and comparison of a novel flame speed closure for two inherently different IC-engines. Moreover, optical data from the RCEM experiments are under review for ignition model validation.

Empa-APTL & Volkswagen corporate research

Cooperation with Volkswagen corporate research was established from 2014 ongoing. An electrical characterization of the ignition system was conducted at the ignition cell at Empa to derive characteristic values for the pairing of the coil and spark plug under different cell conditions. Method development on SIBS was shared with the project partner. Within the EU project GasON, where ETHZ-LAV, Empa-APTL and Volkswagen collaborate in a work package on gas only engines, a similar hardware setup is in use and therefore, findings obtained can be directly reused. Moreover, optical data of the RCEM investigations was shared as a validation base for CFD simulations.

References

1. Kawahara, N., et al., *Fuel concentration measurement of premixed mixture using spark-induced breakdown spectroscopy*. Spectrochimica Acta Part B: Atomic Spectroscopy, 2009. **64**: p. 1085-1092.
2. Fischer, J., et al., *Measurement of the Equivalence Ratio in the Spark Gap Region of a Gasoline Direct Injection Engine With Spark Emission Spectroscopy and Tracer-LIF*. 2004, SAE International: Warrendale, PA.
3. Merer, R.M. and J.S. Wallace, *Spark spectroscopy for spark ignition engine diagnostics*. SAE Technical Papers, 1995.
4. Kammermann, T., et al., *Generation of Turbulence in a RCEM towards Engine Relevant Conditions for Premixed Combustion Based on CFD and PIV Investigations*. SAE International Journal of Engines, 2017. **10**(4).
5. Dirrenberger, P., et al., *Measurements of Laminar Flame Velocity for Components of Natural Gas*. Energy & Fuels, 2011. **25**(9): p. 3875-3884.
6. Halter, F., et al., *Characterization of the effects of pressure and hydrogen concentration on laminar burning velocities of methane–hydrogen–air mixtures*. Proceedings of the Combustion Institute, 2005. **30**(1): p. 201-208.
7. Yu, G., C.K. Law, and C.K. Wu, *Laminar flame speeds of hydrocarbon + air mixtures with hydrogen addition*. Combustion and Flame, 1986. **63**(3): p. 339-347.
8. Hermanns, R.T.E., et al., *Effects of temperature and composition on the laminar burning velocity of CH4 + H2 + O2 + N2 flames*. Fuel, 2010. **89**(1): p. 114-121.
9. Smith, G.P., et al. *GRI-Mech 3.0*. [cited 2017; Available from: http://www.me.berkeley.edu/gri_mech/.
10. Goodwin, D.G., H.K. Moffat, and R.L. Speth. *Cantera: An Object-oriented Software Toolkit for Chemical Kinetics, Thermodynamics, and Transport Processes*. 2017; Available from: http://www.cantera.org.
11. Kolla, H., J. Rogerson, and N. Swaminathan, *Validation of a turbulent flame speed model across combustion regimes*. Combustion Science and Technology, 2010. **182**(3): p. 284-308.
12. Koch, J., et al., *Comparison and Sensitivity Analysis of Turbulent Flame Speed Closures in the RANS G-Equation Context for Two Distinct Engines*. SAE Int. J. Engines, 2016. **9**(4): p. 2091-2106.
13. Langella, I., et al., *Assessment of dynamic closure for premixed combustion large eddy simulation*. Combustion Theory and Modelling, 2015. **19**(5): p. 628-656.
14. Ghiasi, G., et al., *Sensitivity of Flamelet Combustion Model to Flame Curvature for IC Engine Application*. 2017, SAE International.
15. Koch, J., et al., *LES Multi-Cycle Analysis of the Combustion Process in a Small SI Engine*. SAE Int. J. Engines, 2014. **7**(1): p. 269-285.
16. Conte, E., *Combustion of reformer gas/gasoline mixtures in spark ignition engins: A concept for near-zero emission transportation* 2006, PhD thesis, ETH Zurich, Diss. ETH No. 16539.
17. Conte, E. and K. Boulouchos, *Experimental investigation into the effect of reformer gas addition on flame speed and flame front propagation in premixed, homogeneous charge gasoline engines*. Combustion and Flame, 2006. **146**(1–2): p. 329-347.

5. HCNG field testing (WP4)

Empa, Internal Combustion Engines: ***Urs Cabalzar, Thomas Bütler, Mathias Huber***
ETH, Aerothermochemistry and Combustions Laboratory: ***Christian Schürch***

5.1 General targets and state of WP4 compared to the proposal aims/milestones

a) *HCNG blending station*

The overall target is the planning and realization of both an ad interims and a permanent HCNG refueling possibility on the basis of measurements and simulation works. Thereby the emphasis was put on HCNG-mixtures ranging from 0 to 30 vol-%. The following table shows exemplary HCNG-mixtures with corresponding volume, mass and energy fractions.

Table 5.1 Corresponding volume, mass and energy fractions of exemplary HCNG-mixtures

vol-%	mass-%	energy-%
2	0.23	0.55
10	1.25	2.95
25	3.65	8.33

The ad interims solution for HCNG refueling with low H_2 content was successfully taken into operation in the 3rd quarter of 2014 and decommissioned again roughly one year later. It allowed the refueling of three CNG vehicles tested as part of WP4.2 with a H_2 fraction of 2 vol-%.

Modelling and simulations of the CNG refueling process could be carried out as scheduled and were successfully validated with measurements taken on the CNG dispenser at Empa. Subsequently the model was extended to incorporate HCNG refueling which provided relevant support for the development of the permanent HCNG dispenser.

Commissioning of the permanent HCNG dispenser was planned for 2016 but had suffered a substantial delay. One of the project partners went into a lengthy reorganisation process in 2016 which resulted in the loss of project-relevant employees and know how. Also the procurement of the originally desired fuel system parts for the HCNG field test vehicle became uncertain and led to significant delays (see WP4). Therefore, the successful commissioning of the permanent HCNG dispenser took place in August 2017. Since then the dispenser is in operation and allows the refueling of 0 to 30 vol-% of H_2 which lies in accordance with the proposed targets.

b) *HCNG Field testing*

The overall target is to demonstrate that CNG/hydrogen mixtures can be used as fuel in current vehicle powertrains on the basis of field test with different hydrogen blending ratios. The field testing with three standard vehicles, fueled with 2 vol-% hydrogen in CNG, was carried out as planned from 2014 to 2015, including chassis dyno tests to analyze the pollutant emission behavior. A paper on the effects of low hydrogen blending ratios (2 vol-%) in CNG is currently in progress and is expected to be submitted in the beginning of 2018.

The field testing of the specially prepared vehicle was planned to start in 2016 but due to the limited availability of hydrogen-compatible parts experienced significant delays. By the end of January 2017, all parts had finally been delivered. The vehicle's fuel system was rebuilt from February to June 2017 and was certified and approved for road traffic in July 2017. Since August 2017, the vehicle is now undergoing a field test a parcel delivery vehicle in the area of Dübendorf, fueled with a mixture of CNG and 25 vol.-% of hydrogen. The first months showed that the vehicle and the refueling are working properly with no negative side effects for the driver or the driving behavior, even though the engine control unit has not been modified an is still running in its factory setting for CNG.

Empa will carry out further detailed investigations and emission tests in the laboratory following the field test.

5.2 **Main achievements of WP4**

a) *HCNG blending station*

The following listing summarizes the main achievements throughout the complete project duration.

- Working ad interims solution for HCNG-refueling (meanwhile decommissioned again)
- Validated model for CNG refueling
- Various extended models for different HCNG refueling possibilities
- Working HCNG dispenser (0 – 30 vol-% H_2) controlled by self-developed algorithm
- HCNG refueling target pressures determined (taking into account molar fraction of H_2, initial car tank pressure, ambient temperature and compression heat release)
- Various HCNG refueling data from measurements and simulations collected

<u>Ad interims HCNG-refueling solution</u>

To enable real-world measurements on CNG vehicles with low H_2 admixture an ad interims H_2-dispenser was designed and built in collaboration with the company Apex AG and the project partner Endress+Hauser. Thereby a refueling concept was chosen which was not very user friendly but realizable in a short time. The pictures below show the main components of the self-developed H_2 dispenser (left) and the refueling equipment in general (right).

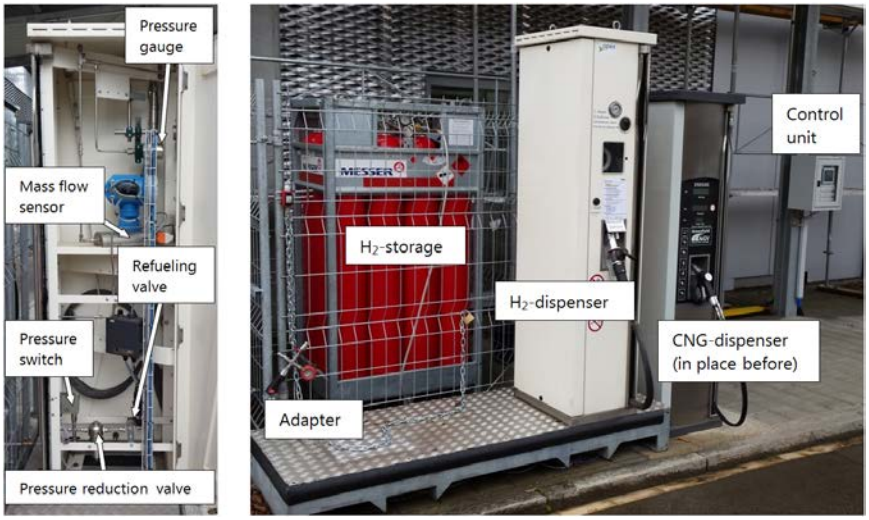

Fig. 5.1 Main components of self-developed H_2 dispenser (left) and the refueling equipment in general (right).

For the user the process of refueling consisted mainly of five steps:

1. Fill fueling hose of the H_2-dispenser by pressing the black button above the nozzle
   ⇨ Enables the determination of initial tank pressure in step 3
2. Connect adapter and fueling nozzle of the H_2-dispenser
3. Read pressure from manometer at the dispenser and ambient temperature from gauge at the control unit to determine the amount of H_2 to be refueled from a table available on site
4. Enter determined amount in control unit and start H_2 refueling
5. After control unit stops H_2 refueling perform a conventional CNG-refueling at the CNG-dispenser

Next to designing a safe and reliably working H_2-dispensing unit and refueling process the main challenge lied in working out the table determining the amount of H_2 to refuel. This amount depends on the mass of CNG refueled subsequently at the conventional CNG-dispenser in step 5 which is not mass but pressure controlled. The CNG target pressure in turn is depended on the pressure after H_2-refueling, the ambient temperature and the temperature increase caused by compression heat release during H_2 and CNG refueling which is not readily determined. However, thanks to existing knowledge and measurements from tasks preceding this project the amount of H_2 to refuel could be estimated successfully using various rough calculations and the required degree of accuracy regarding mixing ratio was met.

The ad interims H_2-dispenser was decommissioned again in 2015.

Computer model for CNG-refueling

In parallel to the realization of the ad interims dispenser a 1D computer model for the conventional CNG refueling process was developed using the multi-physics software *AMESim*. The model particularly consists of the CNG station storage tanks, the dispenser, the car tanks and the system control as depicted in figure 5.2.

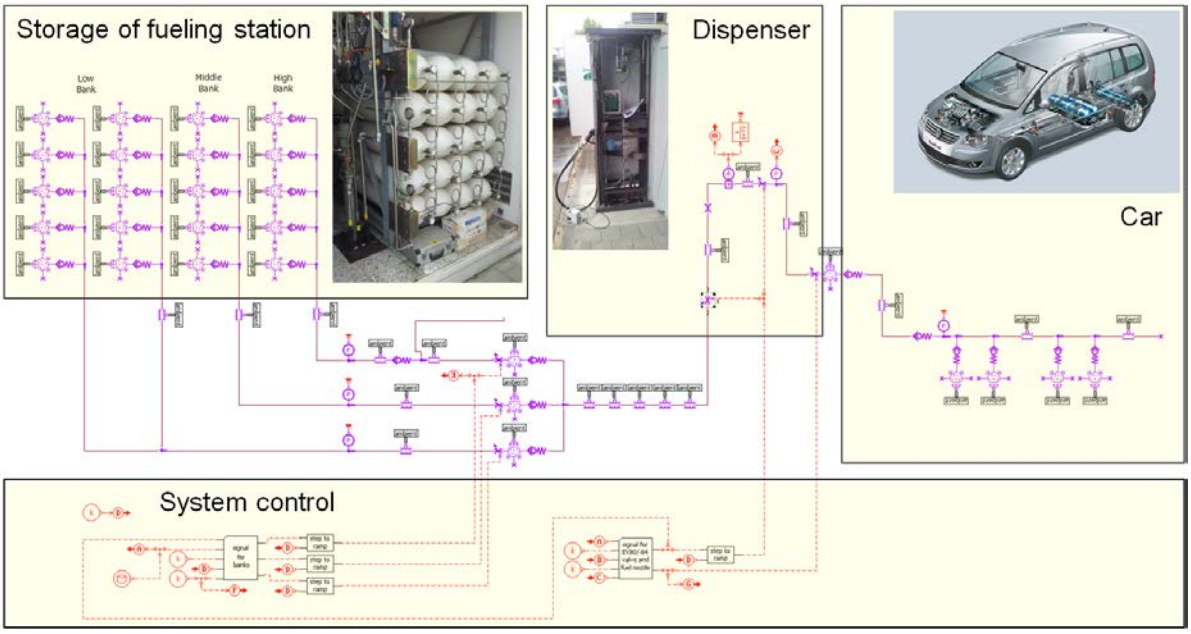

Fig. 5.2 AMESim simulation interface showing the main components of the CNG refueling model

The model allows the observation of pressure and temperature evolution in both storage and car tanks during a CNG refueling process. Whereas pressure losses in pipes and fittings as well as heat transfer through pipe and tank walls are accounted for, the one dimensional approach simplifies pressure and temperature in fixed volumes to be homogeneous at all times. Furthermore, CNG is approximated by CH_4 for which properties are available in the databank of *AMESim*. To incorporate real gas behavior the Peng Robinson equation of state was employed.

The system control was implemented in consultation with the project partner Atlas Copco. Various characteristics of a state-of-the-art CNG refueling controller such as determination of initial tank pressure, switching between storage tanks during refueling (cascade refueling) and the termination of the refueling process were implemented.

The simulation results were validated with measurements taken at the CNG-dispenser of Empa. As test vehicle a VW Touran EcoFuel CNG was used. After fine tuning the control parameters as well as all estimated coefficients determining pressure drop and heat transfer a good correlation between simulation and experiments was achieved. The subsequent figures show data from three experiments and a simulation run of the pressure in the fueling hose as well as the mass flow of a CNG refueling at an ambient temperature of 8°C. The three experiments at almost completely equal conditions show, that the refueling process always incorporates some differences with respect to time, so that simulation results should have the same tendencies but not necessarily need to show precise temporal correlation compared to one experiment (Fig. 5.3).

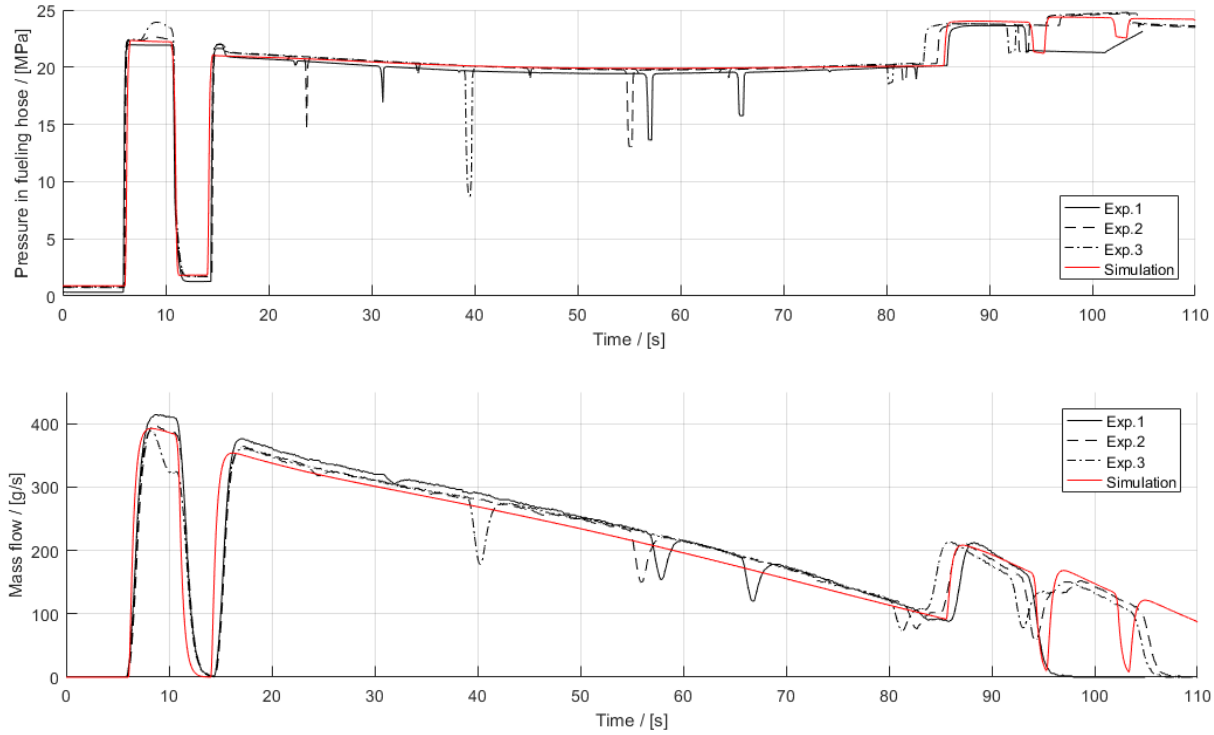

Fig. 5.3 Comparison of measurements and simulation regarding the pressure in the fueling hose (top) and mass flow (bottom) during CNG refueling

The figures display the pressure pulse in the beginning of the CNG refueling (6 s – 11 s) which allows the determination of the initial tank pressure. After around 14 s the actual refueling is started.

Subsequently the pressure in the fueling hose remains almost constant and the mass flow decreases continuously due to the decreasing pressure difference between storage tank and car tank. At around 85 s and 95 s refueling control switches to storage tanks with higher pressure (cascade refueling) leading to an increase in both fuel hose pressure and mass flow.

The dips in the curves are caused by pressure checks triggered by the system control. As these have no significant influence on pressure and temperature evolution during refueling they were omitted in the model.

While developing and validating the model the determination of the heat transfer within the car tank was identified as a task which needs very detailed attention going beyond the scope of this project. In particular regarding the heat transfer coefficient from the gas to the car tank wall no useful literature data could be found. Not least due to this reason a new project proposal was submitted to the SFOE for a more in-depth investigation of the temperature and heat transfer behavior within the car tank during refueling of gaseous fuels. The project is called 'eHF – efficient Hydrogen Fueling' and is scheduled to start in the 3rd quarter of 2017.

Model extension for HCNG-refueling

The validated model for the CNG refueling process forms the basis for the investigations of different HCNG refueling processes. To support the evaluation of refueling strategies for the permanent HCNG-dispenser (0 - 30 vol-% H_2) the CNG model was extended by various set-ups for H_2 addition. Particularly, online mixing of CNG and H_2 as well as intermittent and subsequent addition of H_2 was investigated. Furthermore, the set-ups were rated according to criteria such as functionality, system simplicity, cost of components etc.

For the HCNG-dispenser at Empa, however, the subsequent type refueling remained as the only option. Due to the decrease of volumetric energy density when adding H_2 to CNG it was decided to increase the nominal car tank pressure of the HCNG test vehicle from 20 MPa to 35 MPa. As a result, the HCNG mixture in the car tank can only be achieved by refueling CNG first and adding H_2 subsequently since the pressure in the CNG storage tanks cannot exceed 27 MPa.

In any case, subsequent-type refueling performs very well regarding system simplicity and cost aspects. However, as CNG is only available at 27 MPa in case of the Empa station, a complete HCNG-refueling with high initial tank pressure will not be possible as can be observed in the diagram showing the CNG target pressures later in this chapter. Also, manual cancellation during a refueling process will lead to undesired mixing ratios.

Among other things the extended model for the subsequent-type HCNG-refueling was used to analyze the gas temperature inside the car tank. The figure below shows the mass flow of CNG and H_2 as well as the resulting average temperatures within a specific car tank (in this figure it's tank no. 3) during subsequent refueling. As heat transfer through the car tank is not readily determinable, two different insulation scenarios where analyzed in this example. The blue curve depicts the result for a simulation run with low and the green with high heat transfer to the ambient.

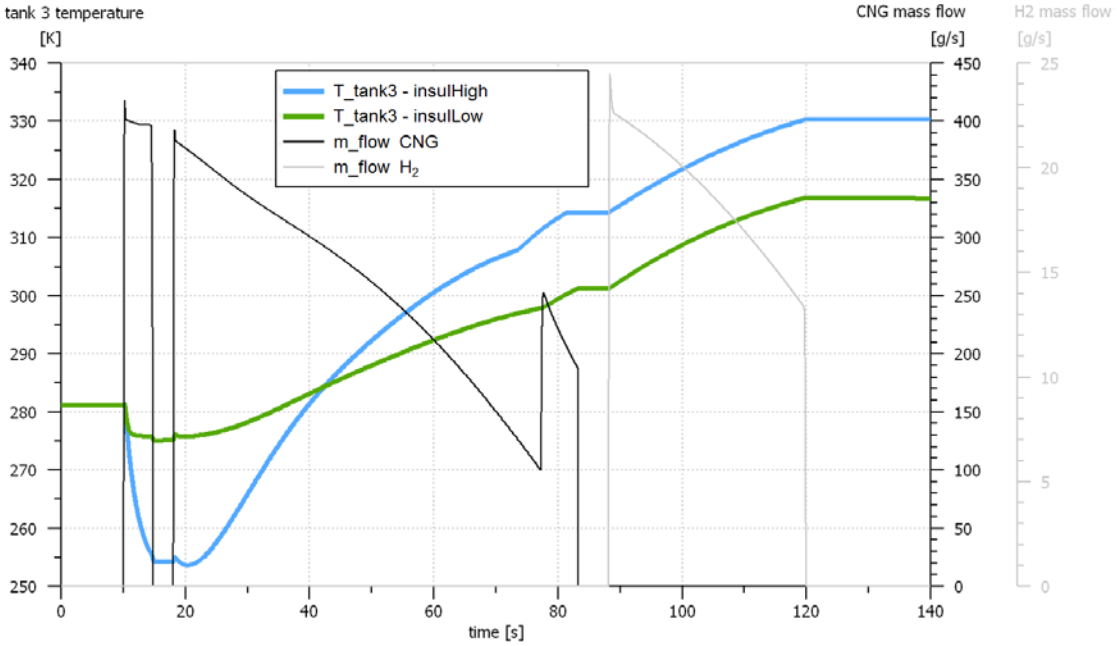

Fig. 5.4 Mass flow and temperature evolution for different heat transfer scenarios of a subsequent-type HCNG-refueling

On one hand knowing the gas temperature within the car tank is important to ensure that the normative temperature limit of 85°C for type IV tanks (as installed in the test vehicle) is not exceeded. With low heat transfer and higher ambient temperatures HCNG-refueling could lead to gas temperatures in the region of this limit. In such case the refueling time needs to be extended to allow more time for heat dissipation so that damage to the car tanks is prevented.

On the other hand the gas temperature needs to be known to determine the necessary storage tank pressures at the station. If gas temperature in the tank rises to high values the car needs to be filled to a pressure significantly higher than the nominal pressure of 35 MPa. If the station storage does not allow sufficiently high pressure levels – as is the case for the Empa station – the CNG refueling needs to be stopped early so that it is possible to refuel enough H_2. By doing so, the car tank will not be filled to full extent but the desired H_2 fraction can be achieved.

While looking into different HCNG refueling processes the question arose, if subsequent or intermittent refueling would cause the HCNG mixture to be inhomogeneous inside the car tank. For that reason very basic measurements using a gas analyzer were conducted to investigate the respective issue. The measurements showed that CNG and H_2 seem to mix well even when refueling subsequently, however, more in-depth analyses are necessary for conclusive statements. Also the fact that refueling lines of the car will be filled with mainly H_2 at the end of a subsequent HCNG-refueling was examined with basic investigations which showed that it doesn't seem to be an issue. Hereby detailed research would need to be conducted as well.

HCNG refueling dispenser

Based on the experiences gained from simulations and experiments in the first two years of the project the permanent HCNG-dispenser was designed at Empa and built by the project partner Atlas Copco. The main components of the HCNG dispenser are shown below.

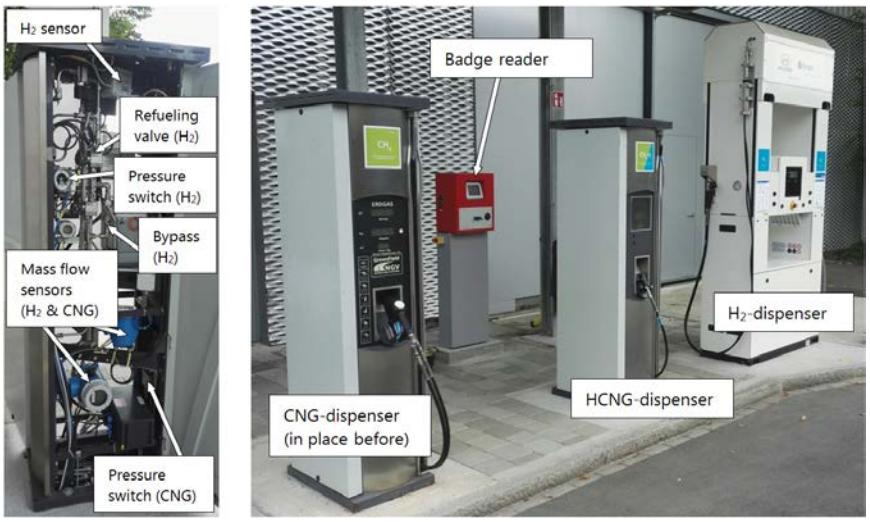

Fig. 5.5 Main components of the self-developed HCNG dispenser (left) and the refueling station at the move demonstration plant (right)

In contrast to the ad interims solution the permanent HCNG refueling dispenser allows HCNG mixtures from 0 to 30 vol-% and refueling is possible without compromising on convenience in comparison with a conventional CNG dispenser. The refueling process is governed by three controllers:

- SEKA (Atlas Copco) Controls first part of CNG refueling including cascade refueling
- Beckhoff SPS Controls second part of CNG refueling and has overall control
- Batch Controller Controls H_2-refueling

The complete refueling strategy and with that also the main logic for the HCNG refueling process was developed at Empa and is implemented in the Beckhoff SPS which has overall control of the refueling. It was programmed using the automation software TwinCAT from Beckhoff that is embedded in Microsoft Visual Studio. Following screenshots are intended to give an idea of the software interface (left) and the visualization tool (right) of the software.

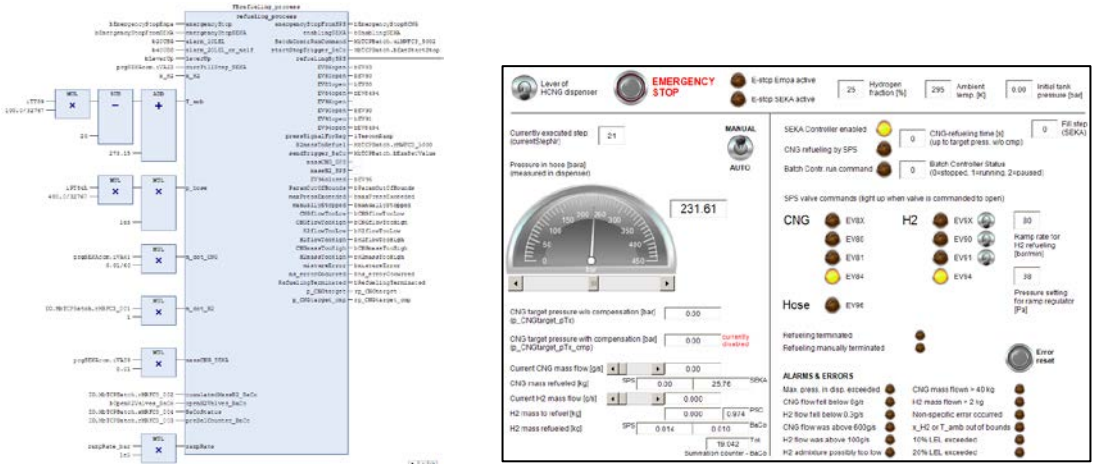

Fig. 5.6 TwinCAT programming interface (left) and visualization (right)

Target pressure determination

Since many relevant parameter are unknown to the HCNG dispenser control (car tank volume & insulation, number of car tanks, car tank pressure & temperature, etc), the data measured at the station site in combination with calculations and assumptions is used for governing the refueling process. As the CNG refueling part is pressure controlled, the determination of the CNG target pressure is of key importance for process control. The target pressure is influenced by the following parameters:

Tab. 5.2 Determination of parameter influencing CNG target pressure calculation

Influencing parameter	Determination of parameter
Initial car tank temperature	Ambient temperature measurement at station site
Initial car tank pressure	Pressure measurement in dispenser after 1st pressure pulse
H_2 fraction	Predefined through Beckhoff SPS
Final car tank temperature	Estimated by simulations and empirical formulas

The target pressure is set so that the energy content of the HCNG-mixture in the car tanks remains equal independent of the parameters listed above. This means that if the car tanks are completely filled, the energy content is always intended to be equal to the energy content of CNG at 20 MPa and 15°C. The H_2 fraction in the car tanks at the beginning of the refueling is not determined. Instead it is assumed that the mixture within the car tank corresponds to the mixture to be refueled. As it is planned to operate the test vehicle with the same mixture for several months this assumption is valid.

The figure below shows the CNG target pressure in dependence of the H_2 fraction. The dependency on initial car tank pressure is depicted exemplary for a value of 2 MPa (green) and 15 MPa (blue). Similarly the solid lines (15°C) and the dashed lines (30°C) show exemplary the target pressure at different ambient temperatures. The black lines illustrate the refueling end pressure which is reached after the subsequent H_2 admixture. Note that all points on the black lines (solid and dashed) represent end pressures for HCNG-mixtures with the same energy content.

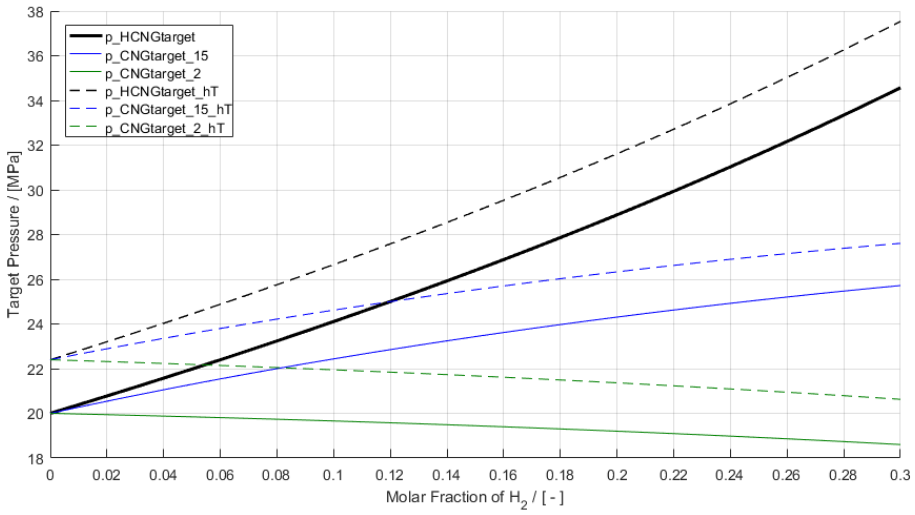

Fig. 5.7 CNG target pressures (colored) and refueling end pressures (black) in dependence of H2 fraction, initial car tank pressure and ambient temperature

The calculated target pressures shown above do not account for compression heat release. Separate correction values based on empirical formulas from Atlas Copco and own measurements and simulations are added to include the temperature increase caused by compression. In addition to abovementioned parameters this correction value also depends on refueling time.

As an example the gas temperature inside the car tank can increase in the order of 50°C when refueling a HCNG-mixture with 25 vol-% of H_2 due to compression heat release. This requires the target pressure to be increased very significantly by around 10 MPa. By adding this value to the target pressures shown in the diagram above one can recognize that complete refueling will not be possible at high ambient temperatures and high H_2 fractions at the Empa dispenser. The pressure in the Empa dispenser is limited to 40 MPa due to some of the installed components. This means that in such cases CNG refueling needs to be stopped early by the control unit to ensure that enough H_2 can still be added subsequently. Otherwise the predefined mixture cannot be met.

It is important to note that temperature increase due to compression heat release is not only critical regarding material limits of the car tank but also regarding the available storage pressure or the pressure limits of the components installed in the dispenser. If the energy content within the car tank is to remain equal for all plausible ambient temperatures and H_2 fractions up to 30 vol-%, the dispenser would need to be able to operate up to pressures of 45 – 50 MPa. Whereas a further increase of the H_2 fraction may make sense with respect to emissions and efficiency of an HCNG vehicle the dispensing of such mixtures becomes significantly more complex. To avoid damaging car tanks and high storage tank pressures precooling of the mixture may become necessary when refueling with higher H_2 contents.

HCNG refueling data

The functionality of the HCNG dispenser was tested on a single cylinder first. It was equipped with piping and fittings that allowed the connection to the fueling nozzle and the emptying of the cylinder between tests.

During the subsequent first refueling of the actual test vehicle with HCNG, data from both the vehicle and the dispenser were recorded. For this refueling the H_2 fraction was set to 25 vol-%. The initial tank pressure was 2 MPa and ambient temperature amounted to 23°C. The diagram below shows the measured car tank pressures for each of the five tanks of the test vehicle during refueling. Thereby, the pressure sensor is placed in the tank valve rather than inside the tank which explains why the pressure curves decrease to equal value in between the pressure pulses in the beginning. The green dots represent pressure measurements within the dispenser hose (recorded with only 1 Hz).

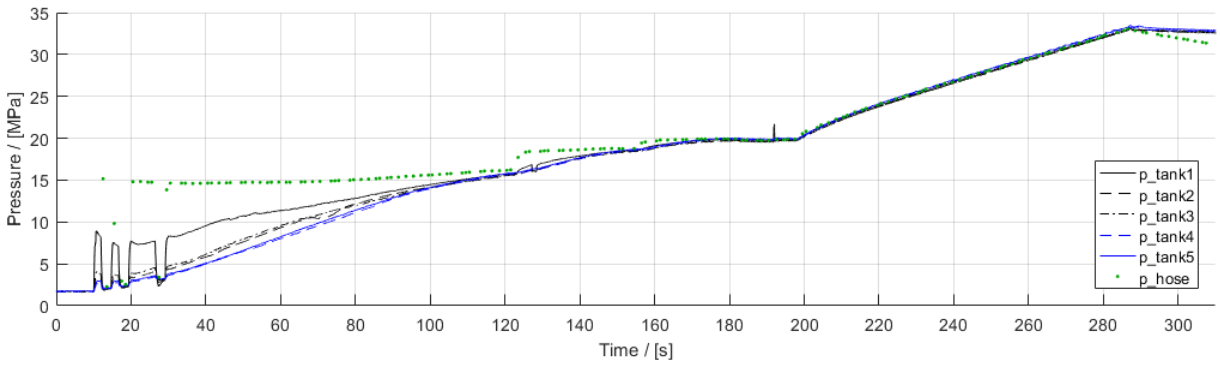

Fig. 5.8 Measured pressures for each of the five tanks of the test vehicle (black and blue) and the fueling hose (green) during refueling

CNG is refueled from around 10 s to 180 s whereas H_2 refueling starts at about 192 s and ends at 287 s. The complete refueling process took approximately 4.5 minutes. Note the pressure drops between hose and the individual car tanks in the beginning of the refueling. As refueling proceeds and CNG mass flow decreases also the pressure differences between the tanks diminish.

Furthermore the gas temperature within the vehicle tanks was measured as depicted in the subsequent diagram. The temperature drop below ambient temperature caused by the Joule-Thomson effect in the beginning which is typical for CNG refueling is not evident in this case. A possible explanation could be related to the location of the temperature sensor and the gas entrance within the vehicle tank. Presumably the cooling effect due to the quasi isenthalpic expansion is mostly limited to the region of the gas entrance and only reaches the temperature sensor in a weakened form.

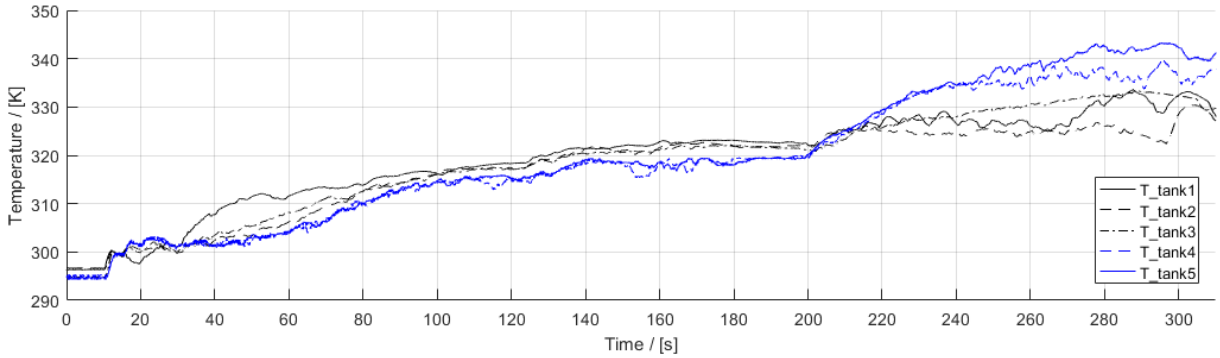

Fig. 5.9 Measured temperatures for each of the five tanks of the test vehicle

Figure 5.9 shows an increase in gas temperature of almost 50°C for vehicle tank 5. It is noticeable that temperatures in tank 4 and 5 which are furthest away from the receptacle rise to the highest temperature values while H_2 is refueled. Also the increase in temperature at around 200 s starts a few seconds earlier. This is an indication that the tanks 1-3 received a greater amount of gas during the CNG refueling part and therefore take up less in the H_2 refueling part which results in different individual H_2 fractions for each tank. For instance, tank 5 should therefore contain a higher H_2 fraction than tank 1. According to very basic investigations conducted during this project, this will not pose a problem for the operation of the vehicle. Due to low gas mass flow in the fuel lines while driving each tank will supply a similar amount of its contents to the engine, so that differences in H_2 fractions are equalized in the common fuel line.

With the realization of the HCNG dispenser according to the predefined specifications the objectives of WP4.1 are successfully met. As stated above, further works allowing more in-depth investigations regarding the temperature and heat transfer development within the vehicle tanks are already in planning. This topic was identified as crucial to develop control algorithms for the refueling process of gaseous fuels. Furthermore, potential for further work lies in the optimization of the HCNG dispenser regarding the noises emitted while refueling. Particularly during H_2 refueling and when the hose is depressurized unpleasant noises are present which have no relevance regarding safety or functionality but could lead to concerned users.

b) *HCNG vehicle field testing (WP 4.2)*

Field test with standard CNG vehicles

Three vehicles of the company Mobility Solution AG, now called Post Company Cars AG, were equipped with data loggers which were configured to record various engine parameters during a field test phase. With each vehicle, baseline measurements were carried out on the chassis dynamometer at Empa focusing on emissions and fuel consumption.

Thereafter, the vehicles were in use about 3 months in normal operation with CNG and where used as parcel delivery vehicles. After this phase, the vehicles were successively switched to HCNG operation (2 Vol-% H_2), fuelled at the ad interims HCNG-refuelling station. The vehicles have been measured again on the chassis dynamometer after some run in time. The vehicles completed their field testing phase at the end of August 2015.

Fig. 5.10 Fiat Ducato from the Mobility Solution AG on the chassis dyno at Empa

These vehicles are mainly used in the parcel distribution service and therefore have a high number of motor starts per day. The data from the field test shows an average of over 30 starts a day, with a maximum of 87 engine starts on one day. 7'600 engine starts with CNG and 10'500 engine starts with HCNG (2 Vol-% H2) have been evaluated. On average, 95% of the engine starts are carried out at an engine coolant temperature higher than 80°C.

The evaluation also included an analysis of engine start times. One of the results of this analysis was the time delay from the first turn of the engine starter (crank) and the first firing of the first cylinder (CTFF) derived from engine speed measurements during start-up. Four different delays were distinguished:

- Very short; CTFF smaller than 100ms
- Short, CTFF between 100ms and 200ms
- Normal, CTFF between 200ms and 400ms
- Long, CTFF bigger than 400ms

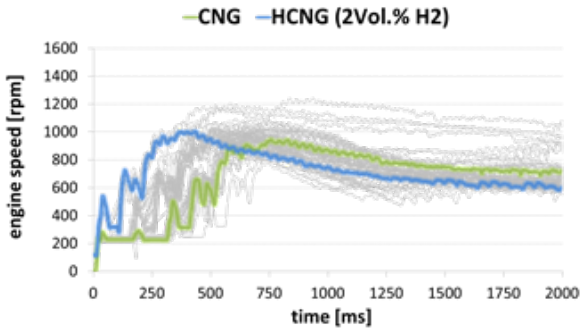

Fig. 5.11 Various engine start speed traces with examples for CNG and HCNG

HCNG compared to CNG operation shows a shift to shorter crank to first fire times (see figure below). This can be explained with the higher ignition quality caused by the hydrogen in the HCNG blend. Even small amounts of hydrogen seem to have an impact on start quality.

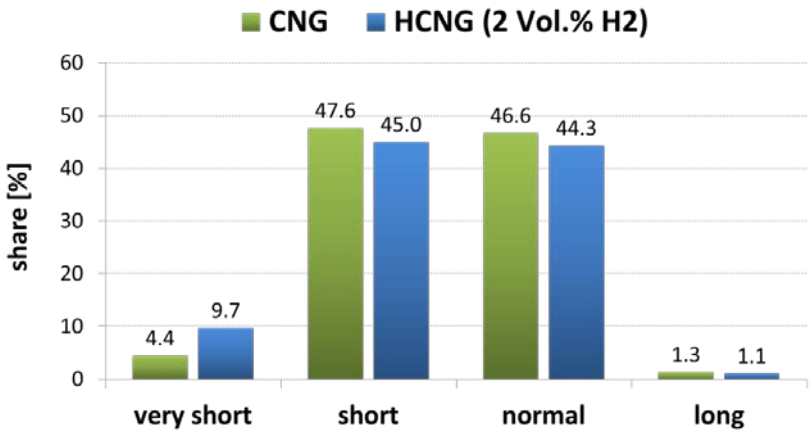

Fig. 5.12 Start time distribution for CNG and HCNG (average of three vehicles and a total of 18'100 engine starts)

Chassis dyno measurements with standard CNG vehicles

With each vehicle base measurements were carried out on the chassis dynamometer with CNG and also with HCNG (2 Vol-% H_2) as fuel. As driving cycle for these measurements, the CADC cycle from the Artemis program has been used. This cycle corresponds to a real world driving cycles with three phases (urban, rural, highway).

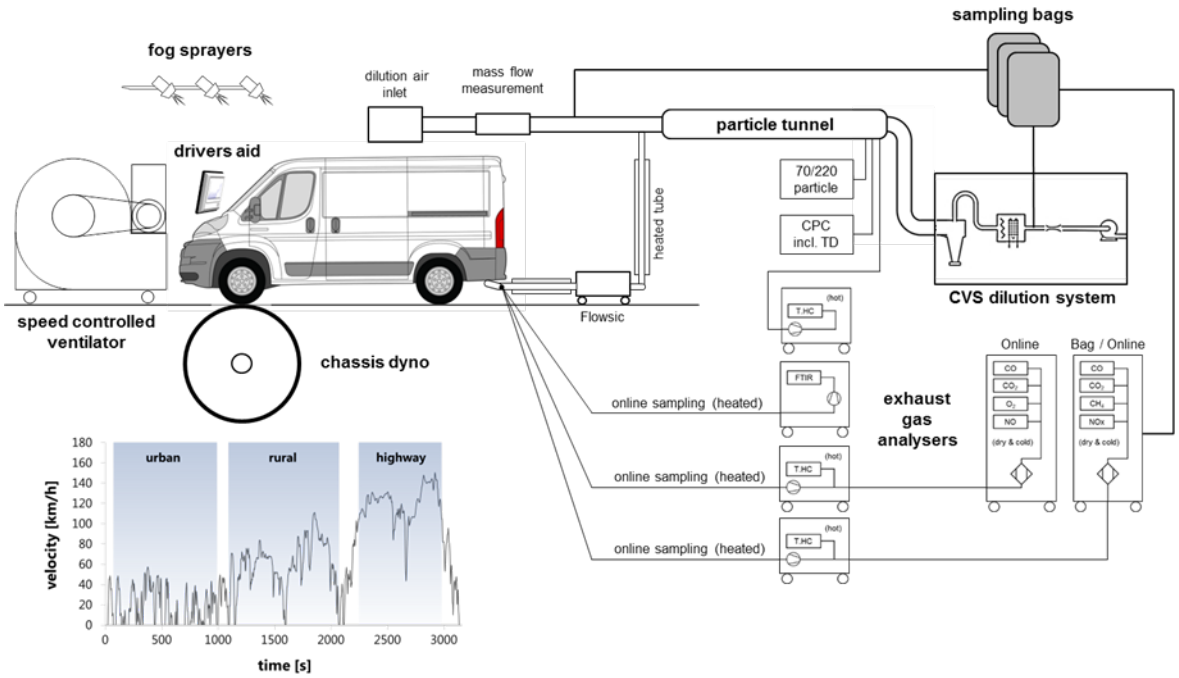

Fig. 5.13 Measurement setup and Artemis CADC speed profile

The emission values for carbon monoxide (CO), nitrogen oxides (NOx) and unburned hydrocarbons (T.HC) show no significant differences between the two types of fuel. However, the 2 Vol.-% H_2 blending shows a slight reduction of CO_2 emissions of 1 - 1.5%, which can be explained by the reduced carbon content of the fuel as well as a slight improvement of the engine efficiency.

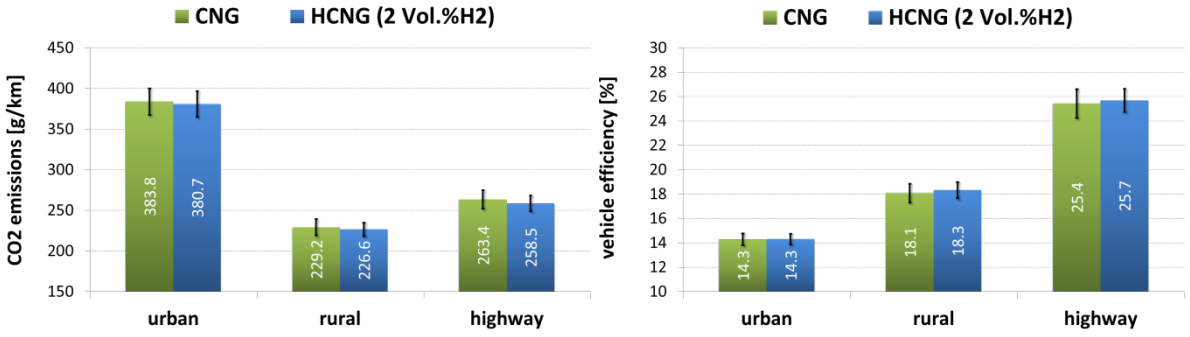

Fig. 5.14 Average CO_2 emissions (CADC sub cycles, error bars represent the standard deviation) and vehicle efficiency (tank to wheel, error bars represent the standard deviation)

The slight efficiency increase can be explained by the improved ignition phase. Such effects have already been observed at Empa in other HCNG projects. In the current case, however, they are very faint due to the low blending of hydrogen. In the overall evaluation, it can be stated that all three vehicles did not show any negative characteristics during the field test as well as during the chassis dyno tests. Therefore raising the hydrogen content of the natural gas in the grid to the maximum of the allowed value for motor fuel application (2 vol-%) represents a favorable option for the storage of excess electricity and making it available for mass mobility.

Field test with standard CNG vehicles

Besides the field test with low blending ratios also higher amounts of hydrogen in methane were tested. For this purpose a special demonstration vehicle was built up during the project. The complete fuel system needed to be designed to withstand the hydrogen-induced embrittlement, caused by the diffusion of atomic hydrogen in the steel.

It was intended to finish the rebuild until the beginning of 2016, but as mentioned earlier, the sub project experienced severe delays in the supply chain of the hydrogen compatible fuel system parts.

At first it was planned to equip the vehicle with 200 bar type 4 CNG bottles to reduce the vehicles empty weight and offer the desired resistance to hydrogen. But refueling simulations showed that the driving range is reduced when hydrogen is added to natural gas due to the lower volumetric energy density of the mixture. To maintain or even extend the driving range also with higher hydrogen blending ratios a concept to set the maximum pressure for HCNG refueling to 350bar was worked out. Hydrogen resistant 350bar bottles are used in different industrial applications, but were not available in the specific dimensions for this vehicle application. Therefore it was decided to switch to 700bar bottles normally used for fuel cell vehicles. The 700 bar type 4 hydrogen cylinders where delivered in April 2016.

In parallel to the procurement of the hydrogen cylinders, enquiries for the rest of the fuel line parts were made. Since the cylinder valves must fit on the cylinders, it was necessary to procure 700bar hydrogen valves. New pressure regulators were needed to reduce the tank pressure from 350bar to the fuel rail pressure of 7bar, and they also needed to be hydrogen and CNG proof.

Clarifications, the quotation and ordering process was time consuming since all the parts where ordered from US and Canadian Manufacturers. These kinds of parts are no stock items and were specially fabricated on order. The last parts where delivered in the beginning of February 2017 and the rebuild was completed by the end of July 2017.

The final fuel system consists of 5 70MPa 36L hydrogen cylinders, each with hydrogen cylinder valve with pressure and temperature sensors. The new stainless steel fuel lines bring the gaseous fuel to the first pressure regulator at the back of the vehicle where the cylinder pressure is lowered to a medium pressure of 70bar. In the front of the vehicle sits another pressure regulator which reduces the medium pressure to the low pressure of 7bar in the fuel rail. To compensate the temperature drop due to the pressure reduction over the regulators and in order to prevent their seals from being damaged due to low temperature, several countermeasures were implemented. Both pressure regulators and a part of the fuel line are electrically heated and a helical 35 meter fuel line was added as a heat exchanger in the rear of the vehicle. The last part is the new stainless steel fuel rail holds the original fuel injectors which are actuated by the unaltered ECU. In this configuration the fuel system has been certified by the SVGW and the vehicle was approved for on-road operation by the STVA of Zürich.

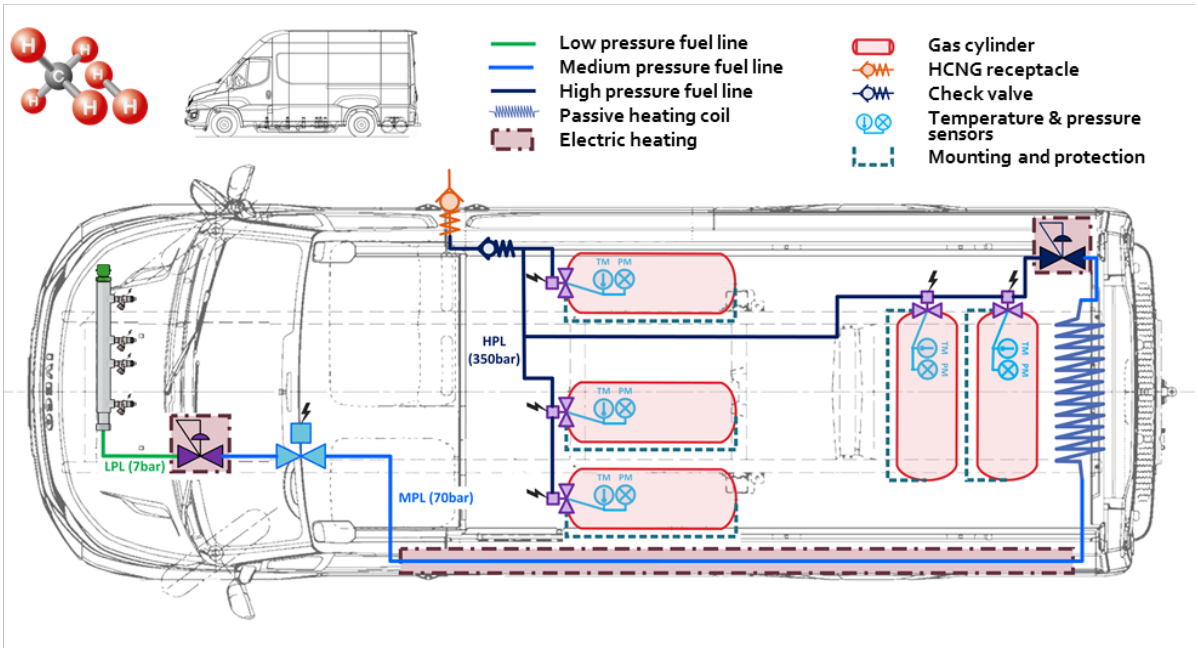

Fig. 5.15 Overview of the system components of the HCNG fuel system

The vehicle started its field test in August 2017 and is running until the current day without problems and the interaction between petrol station and vehicle works properly. Since the fuel lines are designed with a wider diameter then the original system, the re-fueling times of the new fuel system are similar to the durations of the conventional, non-modified vehicle. The field test will continue until spring 2018 and will be completed with additional chassis dyno tests to analyze the fuel consumption and emission behavior of the vehicle concept.

This demonstrator vehicle shows that with minor changes in the fuel system, of which some are already part of the latest state of technology for CNG vehicles, current natural gas vehicles are capable of running with renewable fuel produced with fluctuating excess electricity with lower CO_2 emissions and higher energy efficiency.

c) *HCNG decentralized power (co-)generation*

An engine test bench for emulating conditions relevant for a hydrogen enriched natural gas powered micro combined heat and power (mCHP) plant is shown in Fig. 5.17. The single cylinder 4-stroke naturally aspirated SI engine is equipped with a lambda controller for lean burn operation as well as with a gas mixing device to apply hydrogen addition to the methane fuel and synthetic EGR (only applied for stoichiometric operating points) using CO_2 and N_2 (see Fig. 5.16). The engine torque is measured using an eddy current brake. In addition the engine is fully indicated which allows for heat release calculations of multiple consecutive single cycles. The coefficient of variation of peak pressure or indicated mean effective pressure (IMEP) is used to judge combustion stability. Other characteristic parameters such as crank angles after spark timing at certain heat release are relevant for WP 3 and are extracted also from the data recorded on this test bench.

The influence of hydrogen addition on the emissions is quantified using an exhaust gas analysis system which measures volume concentrations of NO_x, HC, CO, O_2 and CO_2.

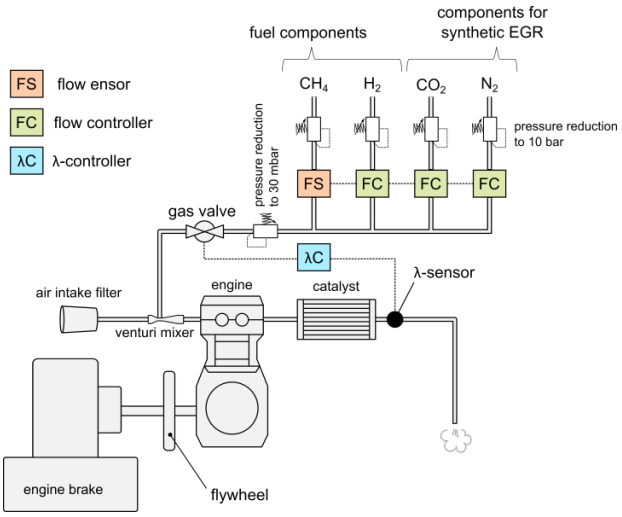

Fig. 5.16 Test bench schematic

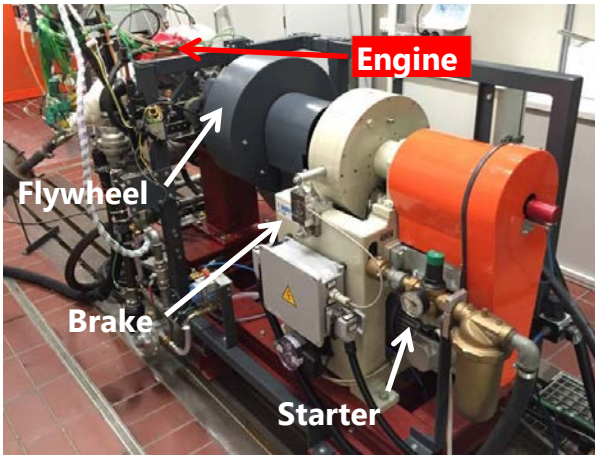

Fig. 5.17 Test bench with eddy current brake, flywheel and the 250ccm naturally aspirated mCHP engine.

H_2 introduction

Micro CHP plants are operated from the gas grid where the fuel pressure is as low as 20-40 mbar. Therefore as a relevant introduction method of H_2 the premixing of NG, H_2 and air in a venturi mixer is implemented in this case. In a similar manner the low pressure synthetic EGR is introduced, see Fig. 5.16. Like this a homogeneous pre-mixed condition is reached at spark timing.

Spark plug concepts

The smallest pre-chamber spark plugs available on the market are of size M14. The spark plug thread size in the investigated engine is M10 and due to close by cooling channels it is not possible to cut an M14 thread into the same Cylinder head. The remaining wall thickness at the weakest point would only be roughly 0.75mm (see Figure 5.18). The tolerances of the cast cylinder head are not exactly known and therefore the risk of damaging the cooling channel with an M14 thread is too big. Open-chamber spark plugs are investigated using hydrogen addition to promote stable combustion and short inflammation phases.

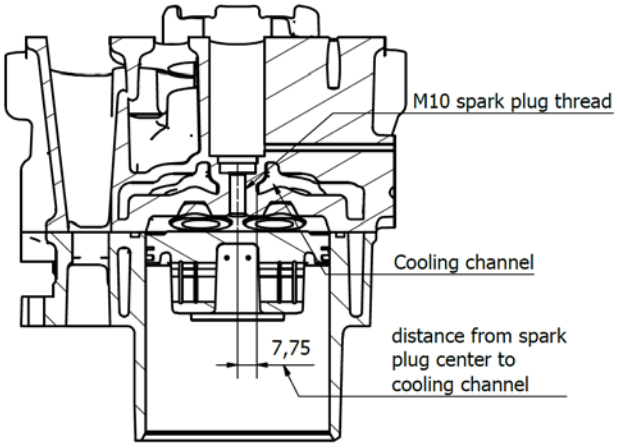

Fig. 5.18 Sectional drawing of the cylinder head.

Operation limits

For both the lean burn - and the EGR engine operation the according limits are investigated by steadily increasing the lambda or the EGR content respectively for a certain CH_4/H_2 mixture until misfiring happens or the torque collapses. The fuel mixtures investigated are 0, 10, 25 and 50% volume share of hydrogen in methane (see first column in Table 5.3). The coefficient of variation of the indicated mean effective pressure (COV_{IMEP}) serves as a criterion for stable engine operation. An operating point with a COV_{IMEP} < 5% is considered stable.

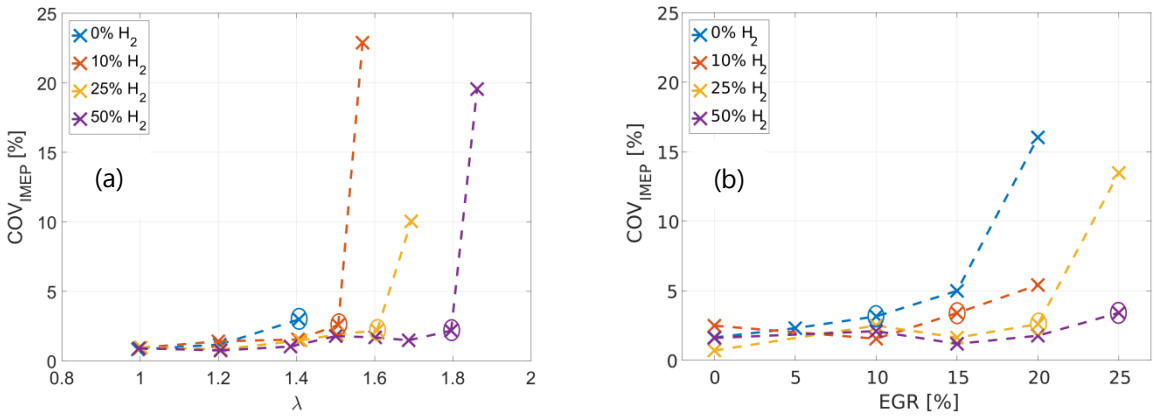

Fig. 5.19 COVIMEP for lean burn (a) – and EGR (b) operation. The points marked with a circle represent the operating limit for the according fuel mixture.

Figures 5.19 show the COV_{IMEP} for all operating points in the lean burn - and EGR operation campaign respectively. For the lambda variation as well as for the EGR variation a drastic increase of COV_{IMEP} is observed beyond a limiting value λ_{lim} or EGR_{lim} respectively, where COV_{IMEP} is still below 5%. This behavior is observed for each fuel mixture investigated. By increasing the hydrogen content of the fuel however, the operating limits are pushed towards higher lambdas or EGR contents respectively. Table 5.3 shows the operating limits of each fuel mixture.

Table 5.3 Operating limits (COVIMEP < 5%) for lean burn – and EGR operation displayed for each of the fuel mixtures used. The eight operating points shown here correspond to the ones marked with a circle in Fig. 5.18.

Fuel mixture [H_2 $\%_{vol.}$]	λ_{lim} [-]	EGR_{lim} [%]
0	1.4	10
10	1.5	15
25	1.6	20
50	1.8	≥25[1]

[1] The fuel mixture with 50% hydrogen could not be tested with higher EGR rates due to flow limitations in the gas valve (see Fig. 5.16).

Efficiency:

Figure 5.19 (a) and (b) illustrate the engine efficiency of the set-up shown in Figure 5.16 for lean burn – and EGR operating conditions respectively. For all fuel mixtures and lean burn operation the efficiency decreases progressively with increasing lambda until the operation limit (marked with a circle) is reached. A steep drop in efficiency can be observed beyond the operation limit. For $\lambda \geq 1.2$ an increasingly positive influence of hydrogen addition is observable for increasing lambdas.

In contrast to the lean burn operation, a clear benefit of hydrogen addition for the EGR operation is not apparent for EGR rates below the operating limit. Compared to the lean burn operation a rather mellow decrease in engine efficiency for increasing EGR rates below the operating limit is observed (see Figure 5.19 (b)). Therefore in general the limits of EGR operation indicate a higher efficiency than the corresponding limits of the lean burn operation.

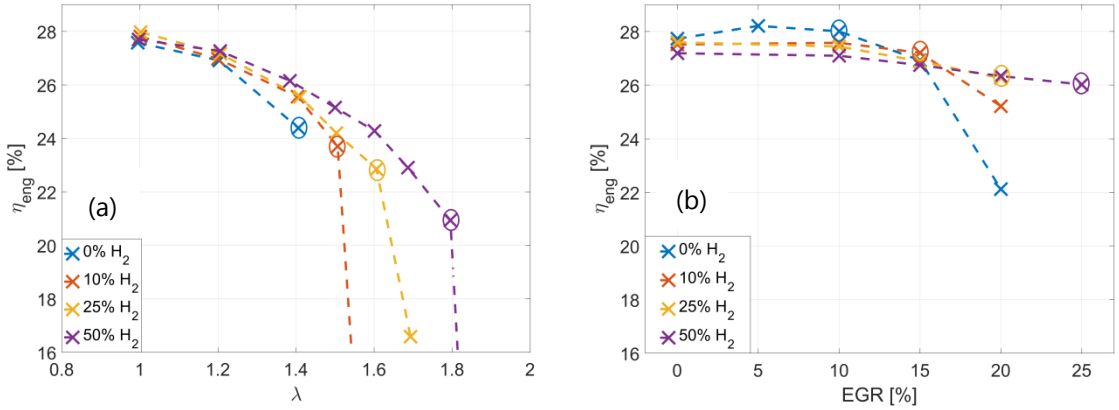

Fig. 5.19 Engine efficiency for lean burn (a) – and EGR (b) operation. The operating limits for each fuel mixture (see table 1) is marked with a circle.

Raw emissions:

Lean burn – as well as EGR operation is applied for raw NO_x emission reduction in cases where only an oxicat is installed for exhaust gas after treatment. For both concepts the NO_x emissions are more reduced the leaner the engine is operated or the more EGR is applied. In the next section only the operating limits shown in Table 5.3 are discussed in further detail because they represent the operating point with the minimum emissions for each fuel mixture.

Figure 5.20 shows the raw emissions for the lean burn operating limits. By adding up to 50% hydrogen to the fuel mixture it is possible to increase the operating lambda to 1.8 and therefore reduce the raw NO_x emissions by 92% down to 42 mg/Nm^3 at 5% oxygen dilution compared to 770 mg/Nm^3 for the best case with CH_4–only-operation. The NO_x emission limit for stationary gas IC engines of a fuel power ≤ 100kW is 250[2] mg/Nm^3. With 232 mg/Nm^3 the raw NO_x emissions of the operating point with $\lambda = 1.6$ and a hydrogen content in the fuel of 25% fall below this limit. The legal limit for carbon monoxide emissions are 650[2] mg/Nm^3 while HC emissions are not regulated. For a mCHP application the carbon monoxide emissions must in any case be reduced using appropriate exhaust gas after treatment. They moderately increase with increasing lambda due to incomplete combustion. The HC emissions almost stay constant due to the cancelling out of both the positive and the negative effect on the quenching distance of the hydrogen addition and the increasing lambda respectively.

[2] Luftreihalte-Verordnung (LRV) vom 16. Dezember 1985 (Stand am 1. April 2017)

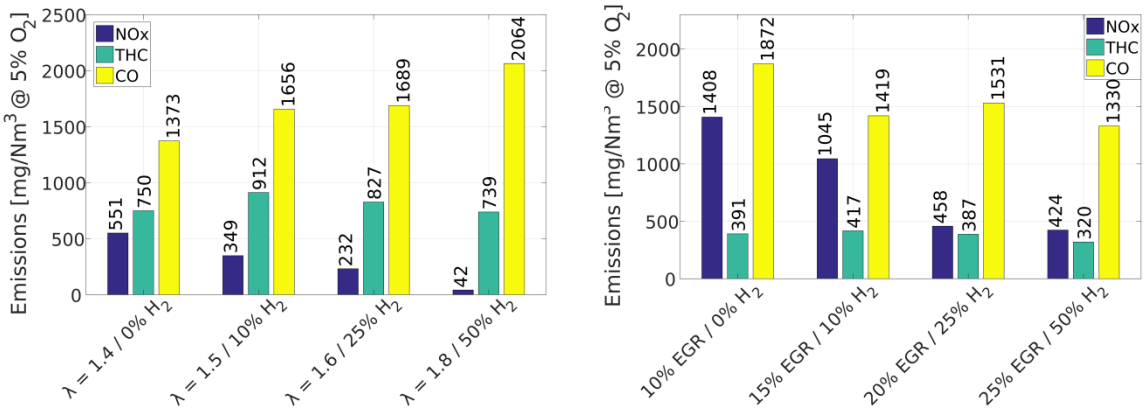

Fig. 5.20 Raw emissions for the operating limits of the lean burn (a) – and EGR (b) operation.

The raw emissions for the EGR operating limits are illustrated in Figure 5.20 (b). Here the hydrogen addition allows for extending the EGR rate from 10 to at least 25%[1] while the NO_x emissions only reduce by 70% down to 424 mg/Nm^3 which is not enough to satisfy the LRV[2].

<u>H_2 addition applied to a stoichiometric mCHP plant with TWC – field testing:</u>

The same fuel mixtures as in the above described engine experiments are applied to the mCHP plant Aladin II. This is a system where a three way catalyst (TWC) and stoichiometric operation are implemented to minimize the NO_x, CO and HC emissions. Regardless on the hydrogen share in the fuel, all emissions are below 30 mg/Nm^3 at 5% oxygen dilution. Also in terms of electrical (32%) and thermal (57%) efficiency no dependencies on the hydrogen share can be observed.

5.3 **Publications / patens**

- Urs Cabalzar; Brigitte Buchmann; Christian Bach, move: the Future Mobility Demonstrator - synthetische Treibstoffe aus erneuerbarem Strom, AQUA & GAS No 10, 2015
- Urs Cabalzar; Marco Brügger; Christian Bach; Brigitte Buchmann, Future Mobility Demonstrator: Utilizing renewable excess electricity in the mobility sector, Proceedings EFCF Luzern, 2015
- Urs Cabalzar; Thomas Bütler; Christian Bach, move Project | Hydrogen Enriched Methane Fuel (HCNG) | Switzerland, Newsletter DBI Gas und Umwelttechnik_Eysser, 2016
- Urs Cabalzar; Christian Bach, move: the Future Mobility Demonstrator at Empa, Hydrogen Report Switzerland 2016–2017 - Hydropole, 2017

5.5 **Industrial and institutional WP4 partners**

▪ SFOE (BFE)	Swiss federal office of energy
▪ FOGA	Research, development and promotion fund of the Swiss gas industry
▪ Atlas Copco	Industrial (gas) company Support regarding the development of the HCNG dispenser. Extended collaboration within the project "Future Mobility Demonstrator" which is linked to RENERG^2 WP4
▪ Endress+Hauser	Instrumentation and process automation company Collaboration in the field of mass flow metering (Coriolis). A substantial part of gaseous fuel dispensing.
▪ Mobility Solutions AG	Corporate fleet manager (fleet of Post AG) Providing and operating of test vehicles for field testing
▪ Iveco / FPT Motorenforsch. AG	Powertrain technologies company Collaboration regarding the adaption of CNG-vehicles for HCNG use
▪ SwissAuto	Engine company Support on CHP test engine
▪ Motorex	Lubricant company Information exchange with respect to permissible engine lubricants for hydrogen enriched fuels

6. Markets & Grids (WP5)

ZHAW, Institute for Data Analysis and Process Design: ***Wolfgang Breymann***
ZHAW, Electric Power Systems and Smart Grid Lab: ***Chan Park, Petr Korba***

6.1 General targets and state of WP5 compared to the proposal aims/milestones

WP5 includes research activities in the field of electrochemical energy storage, its interaction with the electric grid and the efficient use of stored energy as well as simulation of the financial side of an integrated energy system.

The target of the project is to demonstrate the efficiency increase and CO_2 reduction potentials of the whole chain, from electrolytic hydrogen production and the use in energy converters – all being considered here from the point of view of a single power-to-gas plant in this project.

Intermediate targets were:

- Construction of a simulation framework that uses the results of the technical analysis and simulates the financial side of a P2G system.
- Single-mode and multi-mode simulation of PtG at different levels of the Swiss power grid.

The final target is an integrated assessment, including the technological and the economic assessment of whole technology, thus merging the results of WP 5.1 and 5.2. It consists of a PtG feasibility study based on previous study results related to the excess energy due to an increased Photovoltaics (PV) production in a low voltage (LV) with a detailed assessment of revenues and costs for different scenarios.

Due to a lack of resources (only about half of the originally planned budget was available), the integration of the price uncertainty using financial forecasting models could not be carried out.

6.2 Main achievements of WP5

a) *Financial Modeling*

<u>Financial simulation platform and R-interface</u>

The simulation modelling framework includes multiple layers as depicted in the schema below (Figure 6.1).

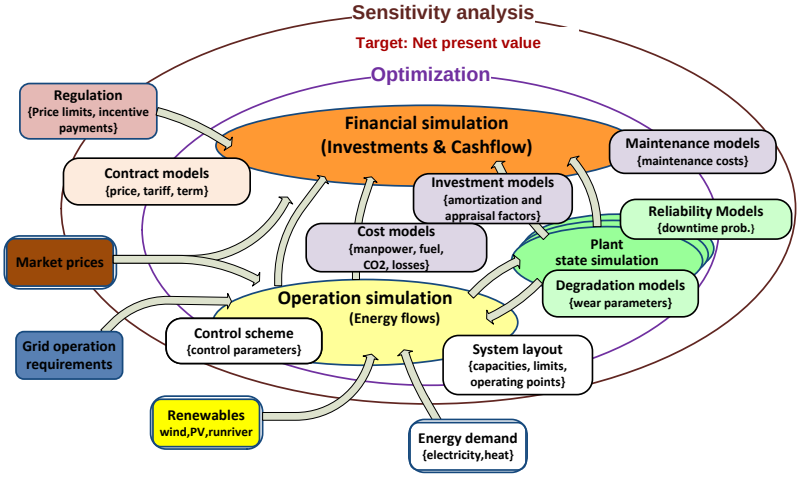

Fig. 6.1 Overall scheme of the modelling framework linking technical (plant models), operational (controller) and financial representation in terms of a corporate model.

The financial simulation framework has been developed in close cooperation with Ariadne Software AG. The platform makes it possible to simulate and analyze the financial side of an entire P2G project. In particular, the balance sheet and the P&L statements are simulated dynamically. The cash flows associated with energy-related services can be integrated directly into the P&L-part of the simulation. Scenarios describing how to operate the different devices can also be defined at this level or imported from the technical model constructed in technical modeling in WP 5.

We have set up a basic corporate / project balance sheet and P&L structures for the generation of analytical results and aggregation and we have implemented a commodity market model for electric power and methane markets and simulated a financial market model for interest rates in EUR/CHF.

In addition, we created an interface to the technical RENERG^2 model in order to simulate the P2G technology in an electric grid that provides a dynamic linking of RENERG^2 physical quantities with financial risk factors.

The platform is commercialized by Ariadne Business Analytics AG.

The financial simulation can be partially accessed through an R interface that has been developed at ZHAW. In addition, it is used by a new risk management platform under development by Ariadne Software AG.

Simplified, excel-based economic scenario modeler and simplified economic viability analysis

Since the originally planned Monte-Carlo simulation with a dynamic stochastic modeling of electricity and gas prices as well as interest rates could not be carried out due to a lack of resources, we have partially compensated this shortcoming by building a simplified, excel-based economic scenario modeler which can compute the present value of different scenarios. You have to indicate the most important input parameters, such as interest rate, the life-time of the machines and operating time per year in hours. It will compute the present value of the power-to-gas technology for different gas prices.

An optimistic scenario is given below and is based on the following assumptions:

A machine life-time of 30 years, an annual usage of 3000 hours as well as an interest rate of 5%.

On the x-axis, we plot the required investment costs in Mio CHF/ MW of capacity. On the y-axis we get the present value of the power-to-gas technology. Different lines in the chart indicate different assumption on the prevailing gas price. Assume the gas price per MWh is 50 CHF. This technology will be profitable if the investment costs are at most 2.3 Mio CHF per MW of capacity (with an assumption of 5% interest rate, 3000 hours of operating time per year). Assume that, in an optimistic case, the current costs are 3.8 Mio CHF per MW. From this you can conclude that the technology has to be another 1.5 Mio CHF per MW of capacity cheaper in order to reach break-even.

Furthermore, we simulate the present value for different gas prices and different interest rates. The same assumptions as before are used.

Below we show an optimistic scenario with a machine life-time of 30 years, an annual usage of 3000 hours as well as initial investment costs of 4.8 million CHF per 1 megawatt of output

Here we can see how much the gas price must increase for the technology to become profitable. Alternatively, it shows by how much the state has to subsidize the gas price so that power-to-gas is profitable. The second line from the top, e.g., assumes an interest rate of 1%. The present value would be zero for a gas price of 50 CHF per MWh, which means that in this case P2G would be marginally profitable. On the other hand, for a gas price of 80 CHF per MWh break-even will be reached even for an interest rate of 5%.

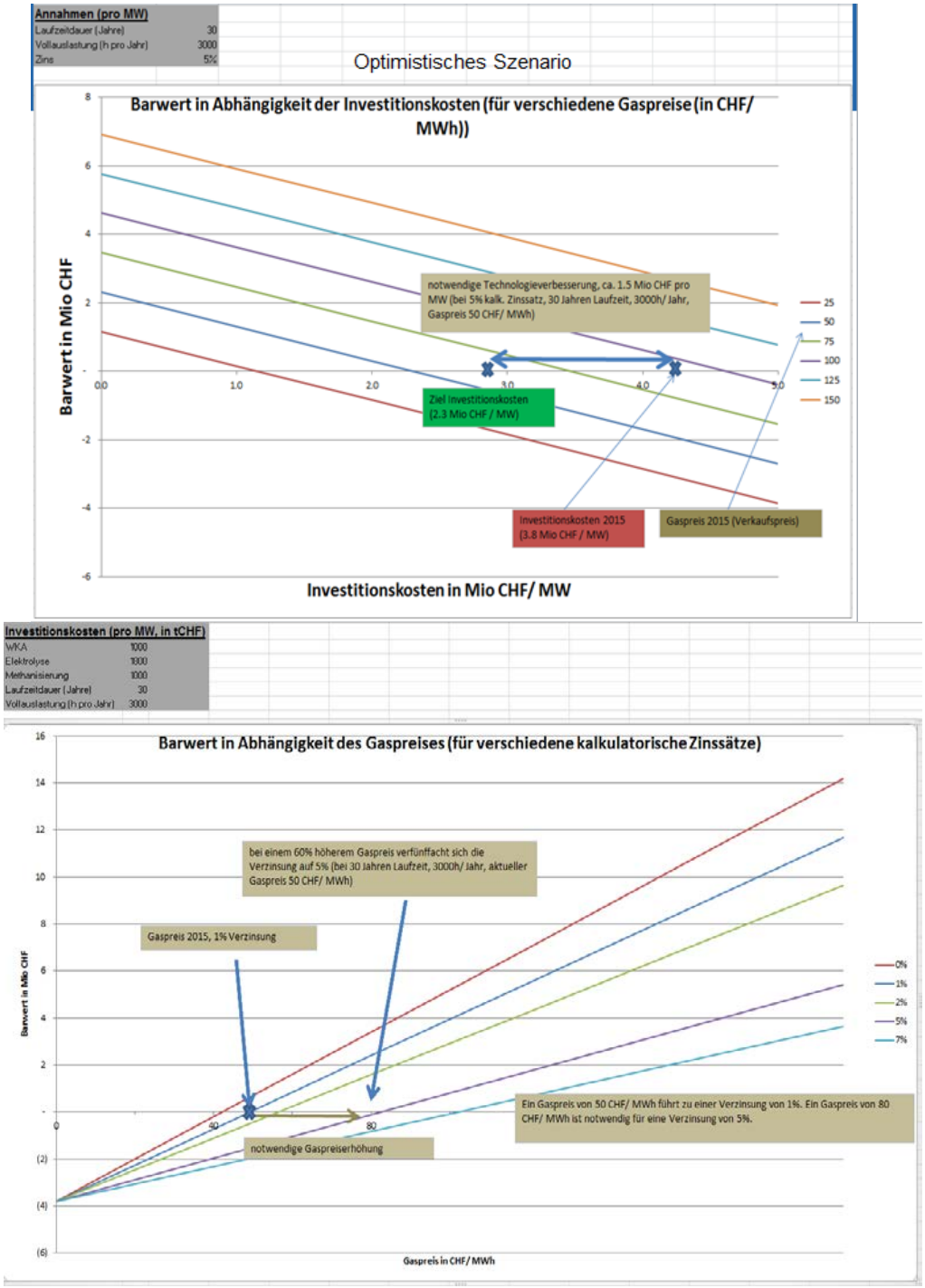

Fig. 6.2 Net present value as function of (a) investment costs (for different gas prices) and (b) gas prices (for different calculatory interest rates).

b) Technical Modelling

Development and analysis of a Swiss grid transmission model (validated in cooperation with Swissgrid) in Matlab/Simulink using MatPower toolbox and solvers.

In order to evaluate and discuss the results of dimensioning PtG plants, the power flows of the Swissgrid transmission model has been validated. The power flow along the most loaded lines are shown below. A map of the Swiss level 1 power grid is plotted there in Matlab, and potential congested lines marked with a red dashed lines. To obtain a representative figure, which shows the grid bottlenecks, the 45 most loaded 220 kV lines, the 5 most loaded 380 kV lines and the 2 most loaded 1000 kV lines, were displayed. This map was compared with the original Swissgrid AG model, which also shows the bottlenecks of the Swiss level 1 power grid.

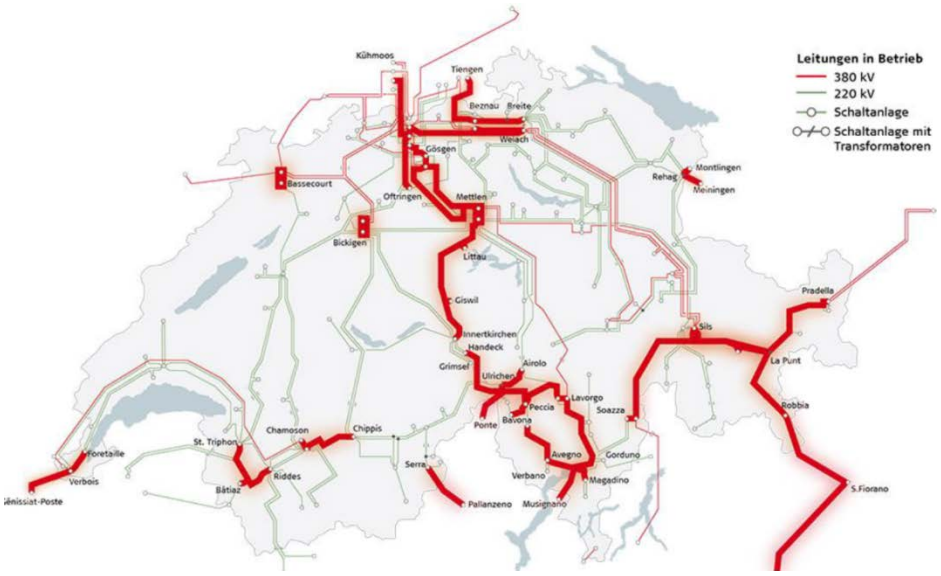

It can be seen in the Matlab and the Swissgrid model look alike in terms of the coincidence of bottlenecks.

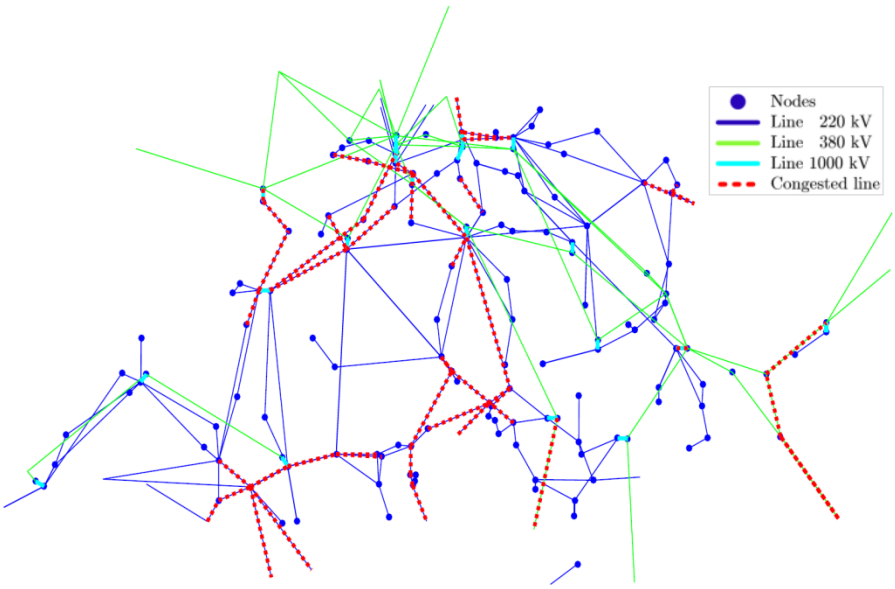

Fig. 6.3 Results of transmission grid simulations using the developed Matlab model vs. the official one used by Swissgrid AG.

Development, validation and analysis of several local low-voltage distribution grid models (in cooperation with EWZ).

The industrial partner Elektrizitätswerk der Stadt Zürich (ewz) provided all the data sets for this study. The dataset includes a prediction for the year 2035, were most of the roofs of the area "Hüslibachstrasse" would be covered with solar panels. All relevant values are predicted every 15 minute on each point of the net. The forecast is over a period of one year shown in a figure below. The PV production in the area compared to the daily consumption is very high. This leads to a big reverse power flow which on the other hand causes strong physical burden to the transformer and the branch, especially in summertime, when the PV production is at the highest level. The goal was avoid these large performance at the transformer and the buses. This can be achieved through long time energy storage systems such as a P2G plant.

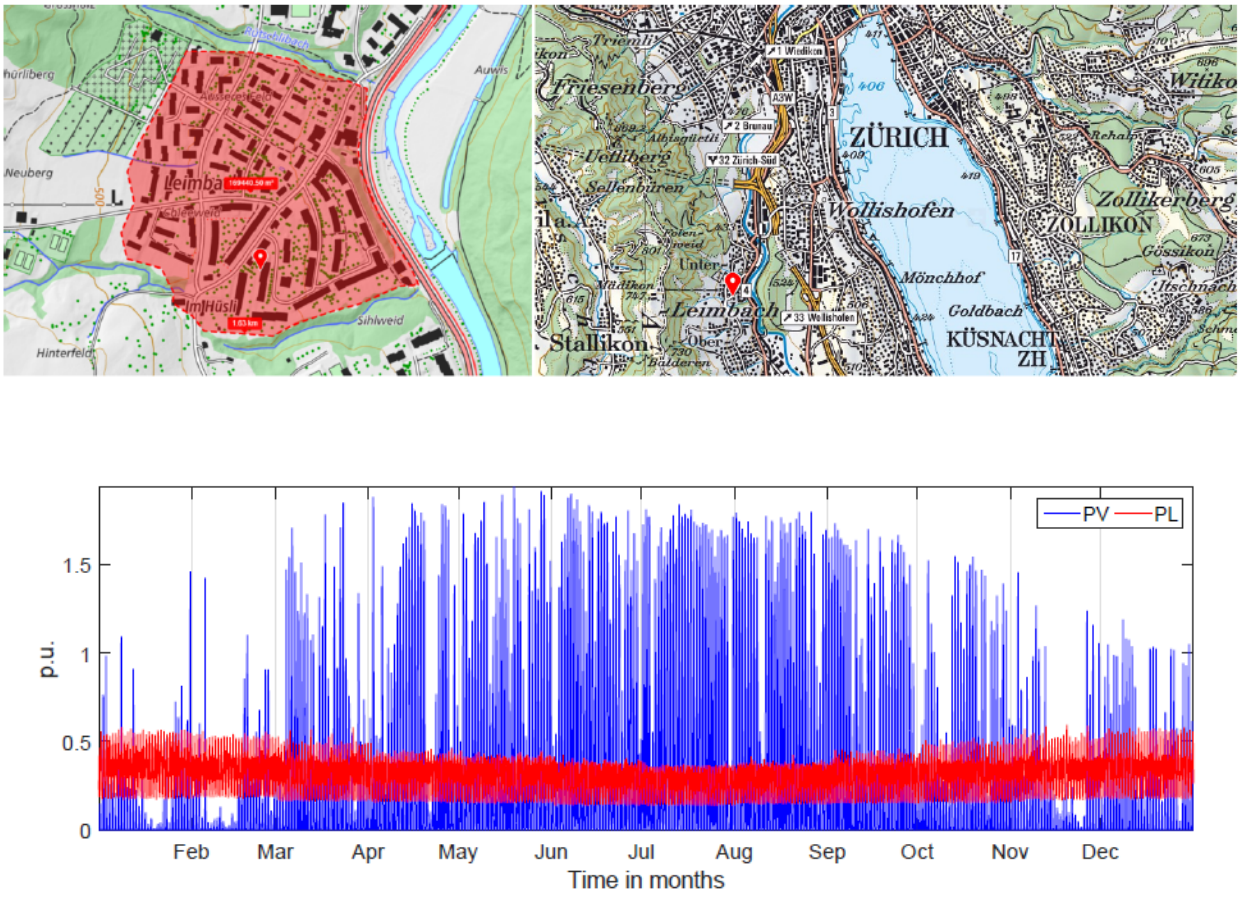

Fig. 6.4 Considered real distribution grid, incl. measured load profiles and expected PV generation.

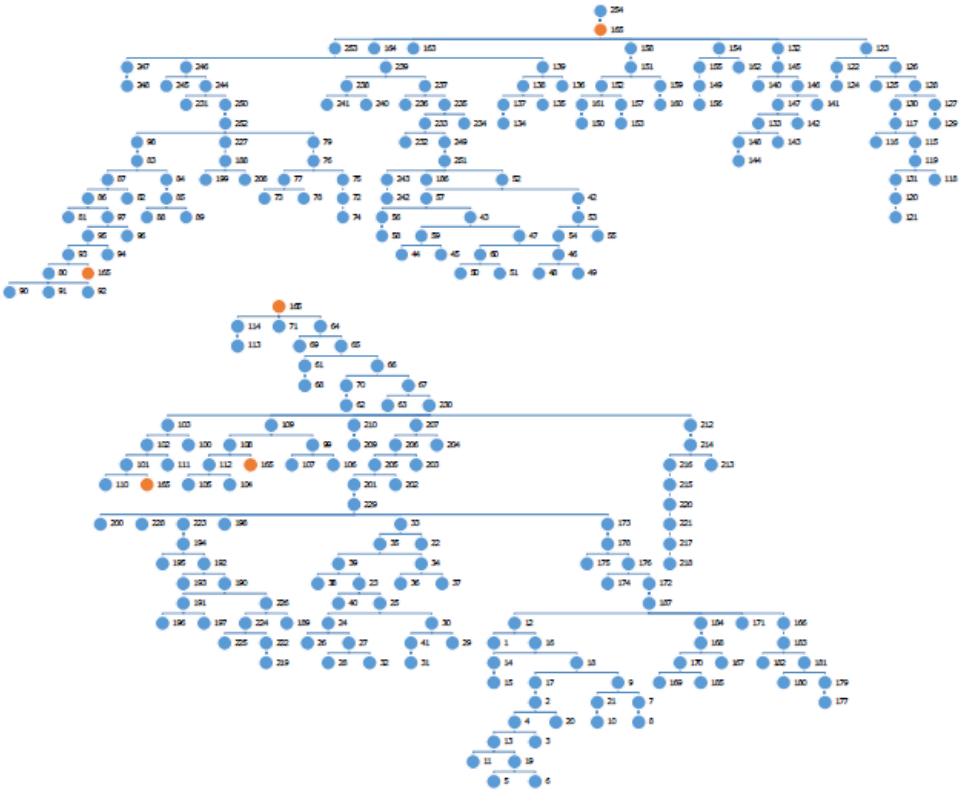

Fig. 6.5 Single line diagram of the considered local distribution grid.

Tools for optimal integration (sizing & siting) of storage systems into the grid (from the electrical grid point of view) and application of these tools to the above-mentioned grid models.

An algorithm has been developed for determining an optimum size of Energy Storage System (ESS) via the principles of exhaustive search for the purpose of local-level load shifting including peak shaving (PS) and load leveling (LL) operations in the electric power system. An exhaustive search method is employed to perform the ESS capacity (Q_{ESS}) and power (P_{ESS}) optimization. The sizing process involves two distinct steps. In the first step, the search for a feasible ESS parameter space in which the requirements of PS and LL are fulfilled (Figure 6.5) and in the second step the search for an optimum point in the feasible space with respect to the cost benefit (Figure 6.6).

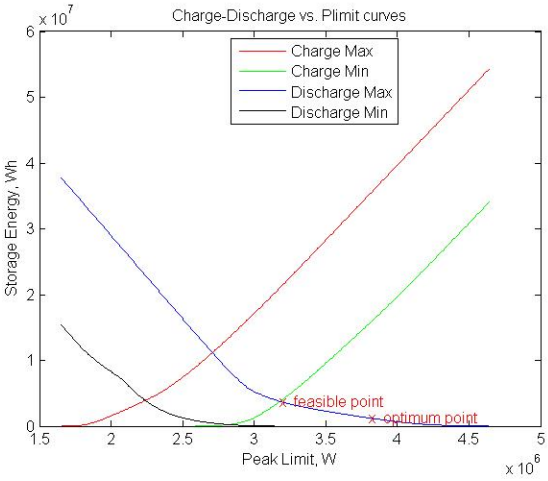

Fig. 6.6 Charge-Discharge vs. Plimit Curves

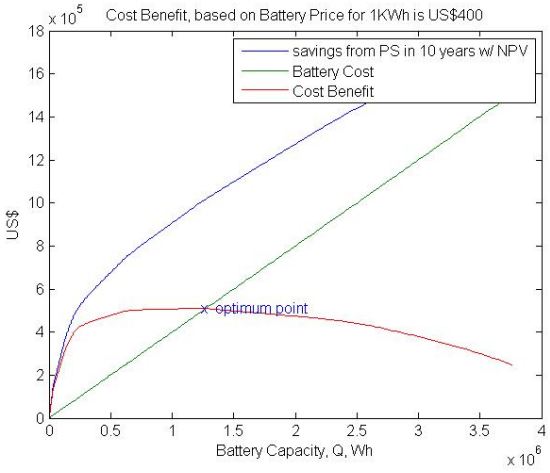

Fig. 6.7 Energy Savings Estimate incl. an example of one cost-benefit optimum point

Then search is expanded to find a set of Q and Plimit 's for each month in order to carry out the load shifting throughout a whole year, as follows: 1) Run the search mentioned about for each month to come up with 12 optimum Q's and 12 Plimit 's for one whole year; 2) Take a maximum Q of 12 optimum Q's as $Q_{optimum}$, which corresponds to the month of October in this case and will be large enough to handle the data for 12 months; and 3) Take each Plimit of 12 months to set Plimit for the month (Figure 6.6). The time-domain simulation with these values is shown in Figure 6.7. Especially Figure 6.8 (a) and (d) indicate that different Plimit levels are set for each month. As a result, the load level shifting was carried out throughout the whole year. A user friendly GUI was developed for a simple application of the developed algorithmas a tool by our industrial partners.

<u>Development of simplified models and controllers for the integration of P2G plants in the above considered grid models enabling to run all required grid simulations.</u>

An algorithm to control the power flow of an electric power system with integrated energy storage systems was investigated. The power system under consideration consists of a conventional distribution feeder that supplies the power to satisfy the customers' demand, a set of photovoltaic (PV) panels that also contribute to the power generation, one unit of Lithium-Ion battery storage for the intra-day use and a combined power-to-gas (PtG) and gas-to-power installation that converts the power excess in the summertime into hydrogen and injects power back to the system in the wintertime. The proposed control algorithm is based on model predictive control tailored for the energy system under investigation. To demonstrate the performance of the proposed control, a set of synthetic PV and demand profiles representing future conditions in Switzerland were created and used as input data to the system model. The synthesized generation and consumption data span a whole year of operation. A number of detailed simulations performed in the framework of the study reported in this paper demonstrate the effectiveness of the proposed control algorithm and provided invaluable insights into the optimum operation of the complex integrated power system as shown in the figure and equations below.

$$x(k+1) = Ax(k) + Bu(k)$$
$$y(k) = Cx(k),$$

$$\min J(k) = \sum_{k}^{k+N_p} \left[P_1^2(k) + (P_{pv}(k) - y_2(k))^2 + y_3^2(k) + y_4^2(k) \right],$$

$$0 = P_g(k) + P_{pv}(k) + P_{ess}(k) + P_2G(k) - P_L(k)$$

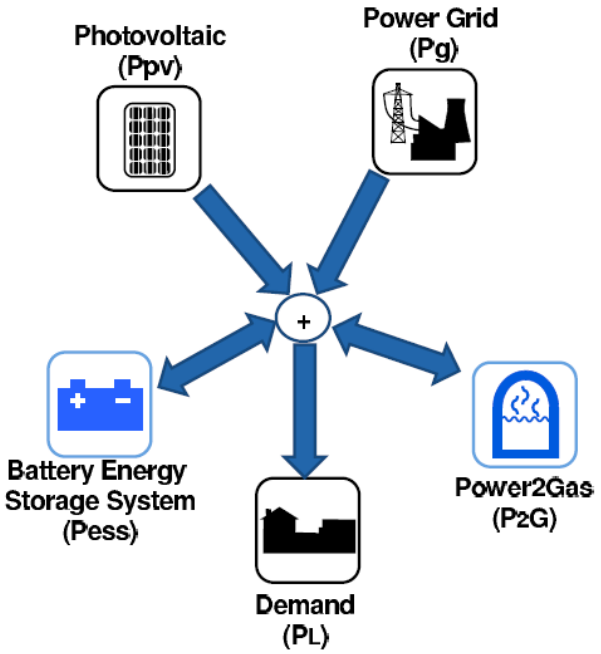

$$0 \leqslant P_1(k) \leqslant P_1^{max}, \quad 0 \leqslant P_g(k) \leqslant P_g^{max}$$
$$0 \leqslant P_c(k) \leqslant P_c^{max}, \quad 0 \leqslant P_d(k) \leqslant P_d^{max},$$
$$0 \leqslant P_{2g}(k) \leqslant P_{2g}^{max}, \quad 0 \leqslant G_{2p}(k) \leqslant G_{2p}^{max}$$

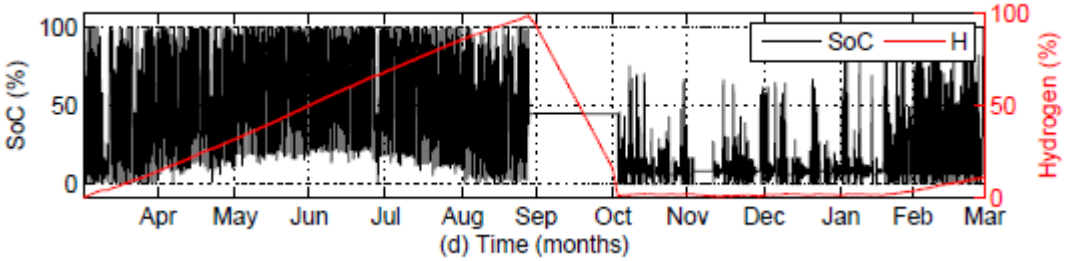

Fig. 6.8 Calculated state of charge and the amount generated hydrogen.

Detailed profitability analysis

An integrated analysis of costs an revenue of P2G technology has been performed for the area of Hüslibachstrasse located at 8041 Zürich Leimbach. The main results are the following.

a. Costs

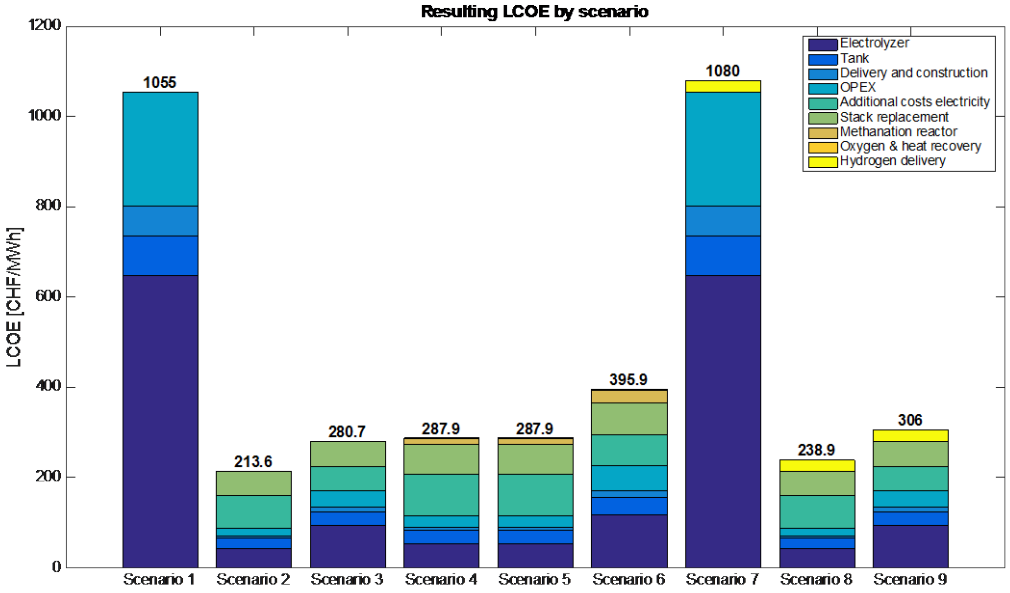

Fig. 6.9 Resulting LCOE by scenario

From **Fehler! Verweisquelle konnte nicht gefunden werden.** the following conclusions can be drawn regarding the resulting LCOE of each scenario:

Operating solely with PV excess energy

When the PtG system is operated solely with the PV excess energy, the LCOE seems drastically higher than when operated in baseload or partload with the grid energy. It can be stated that with the resulting operating hours of 499 hours at nominal capacity the PtG system can never be proven profitable.

Baseload vs. Partload

The baseload operating modes (scenarios 2,4,5, and 8) perform better than the partload operating modes (scenarios 3, 6, and 9). This is due to the fact that the CAPEX can be amortized with higher quantity of product gas over the lifetime, either hydrogen or methane. This shows the relevance of striving for high operating hours of the PtG system.

It has to be noted that this conclusion is only a snapshot based on the current price situation and the assumptions made for the analysis. It can be assumed that the CAPEX can potentially decrease in the coming years when improvement of the electrolyzer manufacturing process will occur. If this is the case, the difference between baseload and partload operating modes will be narrow since the CAPEX has less influence over the LCOE. Moreover, notice the uncertainty as to the electricity price.

Hydrogen vs. Methane

The hydrogen production leads to the lowest LCOE over the lifetime of the plant. This is due to the higher production rate of the gas because the methanation step is skipped and the lower CAPEX because no methanation reactor has to be used.

CO_2 form biogas vs. pure CO_2

In this analysis, no cost difference has been applied whether the hydrogen is produced with CO_2 from biogas or CO_2 from a pure source. As a consequence, the LCOEs for scenarios 4 and 5 are the same. However, this issue warrants further investigation for a more realistic result.

Main cost drivers

In the baseload operation, the main cost driver is the expenses for the additional electricity, followed by the stack replacement cost and the CAPEX of the electrolyzer. In the partload operation, the CAPEX of the electrolyzer takes the leading position of cost driver, followed by the stack replacement costs and the expenses for the additional electricity.

Moreover, it can be concluded that the methanation reactor only marginally contributes to the resulting LCOE. The electrolysis step is by far the most cost intensive part of the PtG system. For all the scenarios, the OPEX seems to play only a marginal role.

b. Revenues

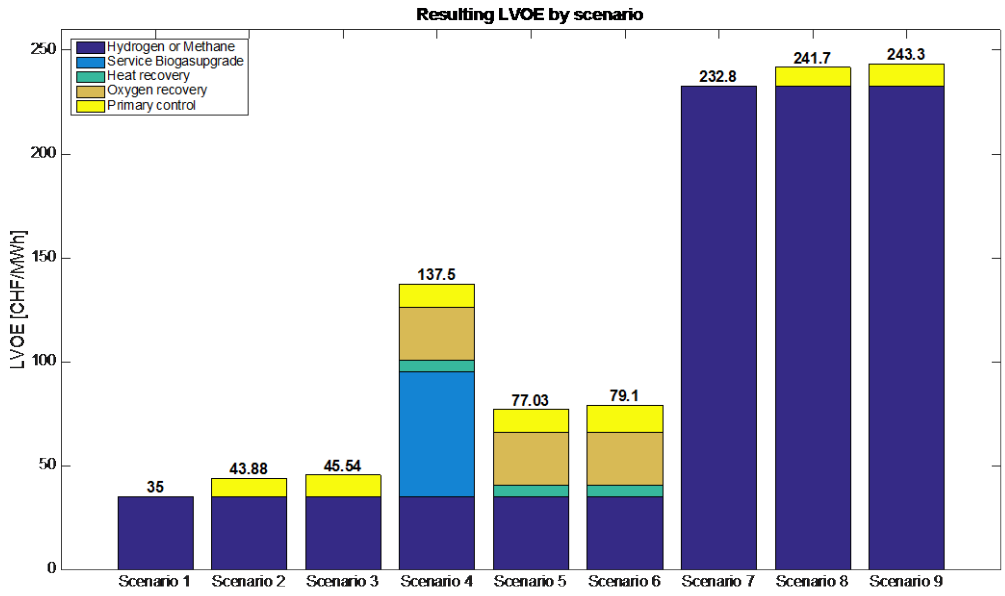

Fig. 6.10 Resulting LVOE by scenario

From Figure 6.7 the following conclusions can be drawn regarding the resulting LVOE of by scenario:

Direct fed-in to gas pipeline

When the product gas is fed into the gas pipeline (scenarios 1 to 6), scenario 4 generates by far the highest value. This is due to the fact that the biogas upgrading service adds a significant value to the LVOE. Moreover, the revenue from the production of oxygen and heat adds more value to scenarios 4 to 6 since they can be used in the process of the biogas plant. The value from the primary control contributes only marginally to the LVOE, and it has to be noted that no expenses for the process or equipment for the primary control qualification have been taken into account.

In conclusion it can be noted that if the gas produced is to be fed into the gas grid, it is more favorable to produce methane since more possible value sources are available.

CO_2 form biogas vs. pure CO_2

As mentioned above it is more favorable to use CO_2 from a biogas or wastewater treatment plant since more value is added with the biogas upgrading service.

Hydrogen in mobility

When the hydrogen in sold in the mobility sector (scenarios 7 to 9), the LVOE can be increased significantly in comparison to scenarios 1 to 6. This is because the hydrogen selling price is based on the diesel market price. However, this conclusion relies on the assumption that the infrastructure of the hydrogen based mobility sector already exists.

H_2 vs. CH_4

It is difficult to compare these two cases. However, it can be said that for hydrogen production it seems more favorable to look for a business case in the mobility sector since the value of the hydrogen can be set much higher as discussed above. Otherwise, the production of methane seems more favorable because this concept can use synergies with already existing biogas plants generating more value. Moreover, the quantity of hydrogen t be fed into the gas grid is limited while no such limit applies to methane.

c. Profitability

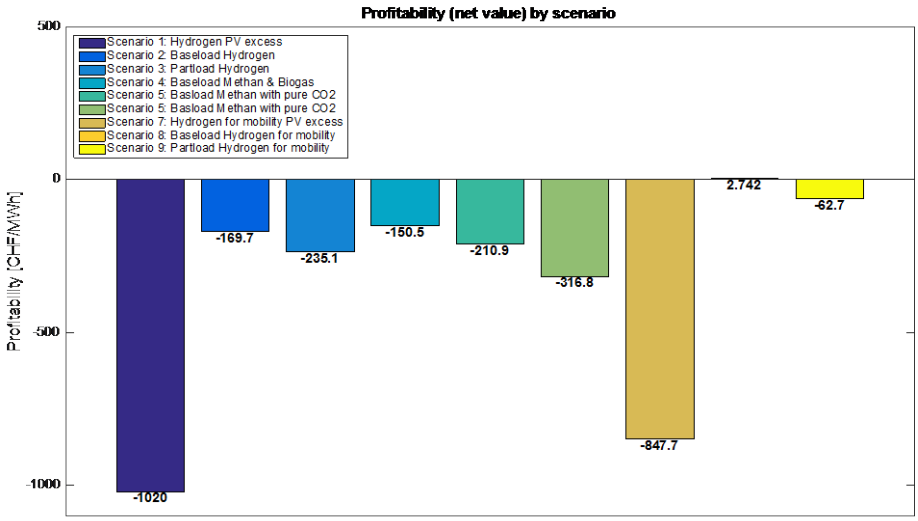

Fig. 6.7 Resulting profitability by scenario

From Figure 6.7 the following conclusions can be drawn regarding the resulting profitability of by scenario:

Operating solely with PV excess energy

In can be concluded that when operated with PV excess only (scenarios 1 and 7) the PtG system seems far from any chance of profitability. This indicates the importance to strive for high operating hours.

Direct fed-in to gas pipeline

As already mentioned in the previous chapter, if the product gas is intended to be fed into the gas grid it is most favorable to produce methane since more value sources are available. Even though all the scenarios produced the negative profitability, scenario 4 displays the least negativity because the biogas upgrading service adds a significant contribution to the value. However, positive profitability has not been reached in all the scenarios, where the product gas is fed into the gas grid.

Direct fed-in vs. mobility

It can be concluded that more promising option is to find a business case in the mobility sector because the hydrogen can be sold for a much higher value. The important finding is that already now this scenario would be marginally profitable if we have not to account for the hydrogen infrastructure for the mobility sector.

d. Discussion

How economically profitable will be the PtG system under different operating scenarios?

The PtG system is yet far from being economically viable if the gas produced is to be fed into the gas grid. However, if the gas is used in the mobility sector, PtG is marginally profitable in the baseload scenario (scenario 8) when we neglect the costs for the hydrogen infrastructure.

It should be noted that the results are based on the assumption regarding the hydrogen selling price. Since market prices are volatile, a more thorough analysis with an appropriate stochastic price model is in order. This also applies to interest rates which at present are particularly low and may rise and vary in the future.

What are the most influential cost drivers?

The most influential cost drivers are the CAPEX of the electrolyzer and the additional purchased energy from the grid. When operated in baseload, the additional energy is the main cost driver whereas the CAPEX of the electrolyzer takes the lead when operated in partload or solely with the use of the PV excess energy.

What measures have to be taken to make the PtG most profitable?

Since PtG is marginally profitable when sold as fuel the policy advice should be to subsidize the infrastructure for the use of hydrogen in mobility. This would ensure profitability of PtG already now and therefore provide a sound basis for the increase use of PtG and thus the further development of this technology.

In conclusion, the author would like to state that the research objectives have essentially been reached. The produced results are based on relatively large number of parameters, which were obtained through exhaustive research effort. However, a certain degree of uncertainty over the parameters still remain. The largest uncertainty, however, concerns the economic environment, namely interest rates and the prices of gas and electricity. Due to a shortage of resources, no such model could be build.

Outlook

The results of this study show that PtG technology would be economically viable in the mobility sector if the costs of the hydrogen infrastructure do not need to be accounted for.

In addition, if a cost reduction of over 50% takes place by 2035, as predicted by the industry experts, the system could reach a state of profitability even if the gas is fed into the gas grid. In order to reach this state as soon as possible (which would provide a significant contribution to reaching the CO_2 limitation goals) it would be helpful if policy could subsidize the creation of a hydrogen infrastructure in the mobility sector.

6.3 **Publications/patents**

Publications

- "On the Estimation of an Optimum Size of Energy Storage System for Local Load Shifting" (Submission to the 2015 IEEE Power & Energy Society General Meeting Denver, Colorado, USA in July)
- "Advanced Control of Energy Storage Systems for Photovoltaic Installation Maximizing Self-Consumption" (Submission to the PowerTech 2015 Conference, Eindhoven, Netherlands, in June 2015)
- L. von Thiessen and S. Weibel: "Modellierung der verbrauchten und produzierten elektrischen Energie in der Schweiz unter Zunahme von Photovoltaik-Anlagen". Winterthur, Juni 2014, unpublished.
- F. Öztürk, "Modellierung von Risikofaktoren wie Zinsen, Equity, Commodities und FX". Winterthur, Juni 2014, unpublished.
- S. Schaffhauser, L. Schneider, "Herleitung sinnvoller Analyse-Metriken auf Basis von Kontrakt-Events und Cashflows." Winterthur, Juni 2014, unpublished.
- C. Park, V. Knazkins, F.R. Segundo Sevilla, P. Korba, On the Estimation of an Optimum Size of Energy Storage System for Local Load Shifting, (Presented to the 2015 IEEE Power & Energy Society General Meeting, held in Denver, Colorado, USA in July, 2015)
- C. Park, V. Knazkins, F.R. Segundo Sevilla, and P. Korba, Advanced Control of Energy Storage Systems for PV Installation Maximizing Self-Consumption, (To be presented to the IFAC symposium on Control of Power and Energy Systems, to be held in Dehli, India in December 2015)
- F.R. Segundo Sevilla, C. Park, V. Knazkins, and P. Korba, Model Predictive Control of Energy Systems with Hybrid Storage, (Submitted to the 2016 IEEE Power & Energy Society General Meeting, to be held in Boston, Massachusetts, USA in July, 2016)
- C. Park, F.R. Segundo Sevilla, V. Knazkins, P. Korba, Feasibility Analysis of the Power-to-Gas Concept in the Future Swiss Power System, (Abstract submitted to CIRED 2016 Workshop, to be held in Helsinki, Finland, in June 2016)
- Park, Chan; Bigler, Felix; Korba, Petr, *Power-to-Gas concept for integration of increased photovoltaic generation into the distribution grid,* 10th International Renewable Energy Storage Conference (IRES) Peer reviewed.
- Park, Chan; Segundo Sevilla, Felix Rafael; Knazkins, Valerijs; Korba, Petr, *Feasibility Analysis of the Power-to-Gas Concept in the Future Swiss Power System*, CIRED WORKSHOP 2016, June 14-15, Helsinki, Finland 14-15 June. Peer reviewed.
- Segundo Sevilla, Felix Rafael; Park, Chan; Knazkins, Valerijs; Korba, Petr, *Model Predictive Control of Energy Systems with Hybrid Storage,* IEEE PES General Meeting 2016, July 17-21, Boston, MA, USA Peer reviewed.
- Park, Chan; Bigler, Felix; Korba, Petr, *The Utility of Power-to-Gas Concept for Integration of Increased Photovoltaic Generation into the Distribution Grid*, 32nd European Photovoltaic Solar Energy Conference and Exhibition 20-24 June. Peer reviewed.

Patents

Title:	State of Charge Management in Battery Systems
Patent application	CH-14116-EP-EPA
Date:	13.10.2014

6.5 **Industrial and institutional WP5 partners**

Ariadne Software AG and Ariadne Business Analytics AG

Ariadne Software AG is a start-up that offers a software platform for the financial simulation and analysis of financial and non-financial projects, firms or groups of firms, based on the concept of Algorithmic Contract Type Unified Standard. There is an ongoing close cooperation between ZHAW and Ariadne. The software is commercialized by Ariadne Business Analytics AG.

EWZ

The project goal is to develop a tool for optimal integration of energy storage systems (P2G) into electric power grids, implementing the tool, and evaluating the impact on existing (realistic) power systems. Originally, we planned collaboration with industrial partners including Swissgrid and EKZ or just an exchange of the relevant data with these partners. During this project period, however, the EWZ has emerged as reliable and a sole industrial partner, which is to provide a model of realistic distribution grid (grid topology). There is in general rather a lack of data to obtain enough realistic load-flow data. For this reason, we plan to develop tools which will generate automatically load flows based on the type of load in a particular region (e.g. industrial and residential area etc.) used as an input information.

In addition there have been discussion of an extension of the collaboration to the financial modeling part but they are in a pretty preliminary state.

SCCER Grids (FURIES)

The technical modeling activities in WP5 is committed to WP2 of the Swiss Competence Center for Energy Research (SCCER) project. The contribution of WP5.2 is focused on the following areas: Utilization of the Power-to-Gas concept in the Swiss power grid; Development of relevant renewable energy generation and storage models; and Integration in simulations and estimation of its impact on the grid in different scenarios. We are also engaged in technical discussions with other SCCER members of EPFL, Lausanne and Neuchâtel (SCCER-FURIES) and University of Geneva, PSI, EMPA, BFH (SCCER-HAE). The main goal of the discussions was to identify opportunities of collaboration on the issues of energy storage including batteries and Power-to-Gas during both the current and the next phase of the SCCER.

Elektrizitätswerke des Kantons Zürich (EKZ)

EKZ provided a grid model of a low voltage distribution grid, which was used in WP5 to evaluate the developed tools for sizing and siting of long time energy storage systems. Because of the general lack of realistic grid data and models the project partners are thankful to EKZ for this support. The results achieved in this project give us the opportunity to collaborate with EKZ bilaterally when the RENERG2 projects is finished.